University of Trento

Alessia Ussia (Ph.D. Student)

INPUT IDENTIFICATION, FOOTBRIDGE CONTROL AND NON-LINEAR IDENTIFICATION OF A MR DAMPER

Prof. Oreste S. Bursi (Tutor)

April, 2014

University of Trento

Doctorate in Engineering of Civil and Mechanical Structural Systems - Cycle XXVI

Board of examiners:

Prof. Dionisio P. Bernal

Prof. Michel Destrade

Prof. Oreste S. Bursi

Prof. Andrea G. Calogero

Prof. Paola Falugi

ABSTRACT

The thesis aims to investigate the dynamical criticality of a pedestrian footbridge and the use of a semi-active tuned mass damper. In this respect, the work appears threefold since the first and third part regard identification of a realistic model for the damping device and semi-active control of the magneto-rheological damper. In this respect, input identification techniques are a useful tool and an aid for the control law design. As a consequence, the second part involves both input identification strategies for a dynamic system and analysis of issues related to the inherent delay. In this respect, the so called “collocation” of measurement devices with respect to the application points of the input is critical, together with the concept of kernel.

ACKNOLEDGEMENTS

Vorrei ringraziare in primis i miei genitori per il sostegno sempre presente,
poi il Prof. Bursi per la grande opportunita', Alessio per l'estrema disponibilita'
dimostrata
e tutti quelli con con cui ho lavorato e collaborato in questi anni.
Infine un caro pensiero a tutte le persone meravigliose che ho conosciuto in questi
anni a Trento e senza le quali non sarebbe stata la stessa bellissima esperienza.

CONTENTS

LIST OF FIGURES

LIST OF TABLES

CHAPTER 1

INTRODUCTION

1.1 Motivation

The work of the thesis starts from the project founded by the Autonomous Province of Trento and regarding to the Nomi-Calliano footbridge. The design of the Nomi-Calliano footbridge was executed by the T&D Associated Engineers of Trento with the aim of connecting the two banks of the Adige River giving continuity to the existing cycling road. Because of the recent events related to some famous footbridges such as the Solferino and the Millennium bridge, the aim of the research project was to investigate the dynamical criticality of this structure in reference to both the cycle and pedestrian action. In addition also the aeroelastic behavior of the footbridge was investigated since the structure is characterized by high slenderness and high sensitivity to dynamic loads. This increased flexibility may compromise the serviceability state since the excessive amplitude of vibrations induced by external loads (wind, pedestrian and so on) unsettles the users comfort while just some modes are subject to resonance induced by loads acting in phase. In this respect, a damping system and a one-year monitoring system became necessary. An experimental campaign was carried out on the Nomi-Calliano footbridge on the 12^{th} of July 2012 with the aims to identify the modal dynamic characteristics of the structure and consequently to design a damping system. However, uncertainties on soil stiffness depending of changes in temperature, suggested that frequencies of the modes to be damped can vary substantially within a range. For this purpose, a semi-active Magneto-Reological Tuned Mass Damper (MR TMD) was chosen to be installed on the footbridge. The semi-active control

system lets change on-line the mechanical characteristic of the device which, after the induced modification, acts like a passive TMD. In this respect, two issues arise; the first is the identification of the hysteretic behavior of the damper; the second is the control law to be adopted for the device control. In this respect, in order to identify both the main properties and the detailed model able to reproduce the experimental behavior, tests on the MR damper were conducted at the Materials and Structural Testing Laboratory of the University of Trento. The main hysteresis models are described and a study on the Unscented Kalman filter (UKF) as tool to identify hysteretic parameters is performed. An accurate parametric model of the damper was finally obtained with the support of trial tests, optimization techniques and the UKF. Eventually, the semi-active control law was preliminary numerically simulated and then the control validation took place by using real data. A clipped control strategy in conjunction with the well known Linear Quadratic Regulator algorithm was chosen as control algorithm. The resulting clipped optimal control law was used in order to find the optimal force able to reduce accelerations of the main structure in absence of a properly tuned tuned mass damper. The thesis has also a second path regarding to the input identification topic. Input identification comprises a range of techniques aimed to the solution of inverse problems. The classical aspect of the input identification is related to the knowledge of the input acting on a structure since we are interested in inferring something about loads starting from output sampled data. In this respect, the input identification comprises three different parts: the identification of number, position and eventually time histories of loads. The thesis considers linear time invariant systems subject to excitations fixed in space and with long duration when compared to the fundamental period of the structure. For this conditions it shows that the number of independent inputs can be extracted from the output measurements and that their position can be established with the aid of a model without the need to perform a combinatorial inspection of all the possible scenarios. The problem of the inherent delay between inputs and outputs is addressed and a sequential deconvolution approach called Segmented Deconvolution Algorithm (SDR) is proposed. The sequential process is conditionally stable and the condition for stability is derived together with hints about the possible presence of ill conditioning. Input identification techniques are

used within the framework of a real application with the aim of validating the investigated semi-active strategy. The reconstructed input is in fact applied on the simplified 2DoF model outlined by the Den Hartog theory and used in the design of the controller. The final result is that the validation of the control strategy took advantage of both the recorded data from the monitoring system of the real structure and the input identification technique.

1.2 Organization of the thesis

This thesis presents the research proposed by the author on system identification and control of a MR damper together with a study on the input identification strategies. This research is sponsored by the Autonomous Province of Trento and includes the following chapters.

- **Chapter 1** presents the thesis objectives and motivation.

- **Chapter 2** is an introductory Chapter summarizing the linear time invariant systems theory. Both continuous and discrete time state space representation of dynamical systems are introduced together with the concept of observability and dynamic response in terms of Markov parameters. A brief portion of the control theory is reported with the description of the LQR algorithm. Eventually, both the modal domain representation and the order reduction of the system are presented.

- **Chapter 3** treats the Kalman Filter theory. The chapter is focused mainly on the linear filter and on its non linear version called Unscented Kalman Filter since they have been used within the input identification field. The in-depth analysis of references with respect to the Kalman filter application has highlighted some significant issues.

- **Chapter 4** summarizes the state of the art in both vibration mitigation problem and control in civil structures, analyzing passive, active, and semi-active solutions; in addition, some actual examples are shown. Then the Nomi-Calliano footbridge is introduced together with its vibrational criticality in order to design the damping system including three passive and one semi-active

devices. At his purpose, dynamic identification and model updating are performed.

- **Chapter 5** is dedicated to the input identification theory and to issues related to the input reconstruction. The Segmented Deconvolution Algorithm is presented and validated by means of both numerical and experimental tests.
- **Chapter 6** is about testing, identification and semi-active control of the tuned mass damper with the aid of numerical and experimental tools such as the input reconstruction and real data.
- **Chapter 7** contains summary, conclusions and future perspectives.

1.3 Objectives

The objective of the thesis is the investigation of dynamical criticality of a pedestrian footbridge and the use of a semi-active tuned mass damper. In this respect, the work appears threefold since first and third parts regard identification of a realistic model for the damping device and semi-active control of the magneto-rheological damper. In this respect, input identification techniques are a useful tool and an aid for the control law design. As a consequence, the second part involves both input identification strategies for a dynamic system and analysis of issues related to the inherent delay. In this respect, the so called “collocation” of measurement devices with respect to the application points of the input is critical, together with the concept of kernel.

CHAPTER 2

STATE SPACE REPRESENTATION, OBSERVERS AND CONTROLLERS

2.1 Introduction

In this chapter there are some basic concepts regarding the theory of the Linear Time Invariant systems (LTI). These systems are described in term of state space representation which is a mathematical model of a physic system composed by a set of inputs, outputs and state variables connected by first order differential equations. First, the continuous and the discrete space representation and their relation is reported and the hypothesis at the base of both the Zero Order Hold (ZOH) and the First Order Hold (FOH) discretization is described in detail. Then, the concepts of observability, reconstructability and detectability are introduced and more attention about the asymptotic state estimator in open and closed loop is payed. In addition, the dynamic properties of the LTI system are described in terms of Markov parameters. A brief description of Linear Quadratic Regulator (LQR) and Linear Quadratic Gaussian regulator (LQG) are reported and eventually, the system dynamic behavior is described in term of modal coordinates in state space and the concept of modal truncation is introduced.

2.2 Continuous time state space representation

The equation of motion for a finite dimensional linear dynamic system viscous damped in second order form is in Juang and Phan (2001) and can be described as,

$$M\ddot{u}(t) + C\dot{u}(t) + Ku(t) = Sd(t) \tag{2.1}$$

where M, C and $K \in \mathbb{R}^{nxn}$ are the mass, damping and stiffness matrix, respectively. $\ddot{u}(t)$, $\dot{u}(t)$ and $u(t) \in \mathbb{R}^n$ are the acceleration, velocity and displacement vector, respectively. $S \in \mathbb{R}^{nxr}$ gives the spatial distribution of the r excitations $d(t) \in \mathbb{R}^r$. Assuming that M is invertible, one can write,

$$\ddot{u}(t) = -M^{-1}C\dot{u}(t) - M^{-1}Ku(t) + M^{-1}Sd(t) \tag{2.2}$$

Adding the equation $\dot{u}(t) = \dot{u}(t)$, one has

$$\frac{d}{dt}\begin{bmatrix} u(t) \\ \dot{u}(t) \end{bmatrix} = \begin{bmatrix} 0 & I \\ -M^{-1}K & -M^{-1}C \end{bmatrix}\begin{bmatrix} u(t) \\ \dot{u}(t) \end{bmatrix} + \begin{bmatrix} 0 \\ M^{-1}S \end{bmatrix} d(t) \tag{2.3}$$

where $x(t) = \begin{bmatrix} x_1(t) \\ x_2(t) \end{bmatrix} = \begin{bmatrix} u(t) \\ \dot{u}(t) \end{bmatrix}$ is the state vector and $x(t) \in \mathbb{R}^{2n}$. Substituting the state vector into Eq. 2.1 one gets,

$$\dot{x}(t) = A_c x(t) + B_c d(t) \tag{2.4}$$

with the system matrix $A_c \in \mathbb{R}^{2nx2n}$, where $A_c = \begin{bmatrix} 0 & I \\ -M^{-1}K & -M^{-1}C \end{bmatrix}$, the input to the state matrix $B_c \in \mathbb{R}^{2nxr}$ where $B_c = \begin{bmatrix} 0 \\ M^{-1}S \end{bmatrix}$ and the input vector $d(t) \in \mathbb{R}^r$. Assuming that measurements are linear with respect to the state, the set of equations describing the outputs in terms of state variables and with zero initial conditions, reads

$$y(t) = Hx(t) \tag{2.5}$$

where $H \in \mathbb{R}^{mx2n}$ is the output influence matrix and depends by the number and location of sensors used to measure the system output. If the output is acceleration, then,

$$y(t) = R_a\ddot{u}(t) \tag{2.6}$$

Substituting the equation of motion solved for $\ddot{u}(t)$ as shown in Eq. 2.2 into Eq. 2.6, yields

$$y(t) = R_a M^{-1}\left[Sd(t) - C\dot{u}(t) - Ku(t)\right] \tag{2.7}$$

thus the general form writes

$$y(t) = Hx(t) + Dd(t) \tag{2.8}$$

where $H = [-R_a M^{-1} K, -R_a M^{-1} C]$ and $D = \left[R_a M^{-1} S\right]$ and the matrix D is the direct transmission matrix with dimension *mxr* - *m* and *r* number of outputs and inputs respectively. Eqs. 2.4 and 2.8 form the continuous-time state-space description of a linear time-invariant system.

2.2.1 Response to a general input

In order to obtain the state $x(t)$ at any time, we simply need to integrate the state equation 2.4, which can be conveniently solved with the method of matrix exponential. First, we rearrange the differential equation

$$\dot{x}(t) - A_c x(t) = B_c d(t) \tag{2.9}$$

and multiply both sides by $e^{-A_c t}$

$$e^{-A_c t}\left(\frac{dx}{dt} - A_c x(t)\right) = e^{-A_c t} B_c d(t) \tag{2.10}$$

that is the perfect differential of

$$frac dx dt \left[e^{-A_c t} x(t)\right] = e^{-A_c t} B_c d(t) \tag{2.11}$$

Integrating both sides from t_0 to t and using τ as dummy variable, yields

$$\int_{t_0}^{t} \frac{dx}{d\tau}\left[e^{-A_c t} x(\xi)\right] \xi = \int_{t_0}^{t} e^{-A_c \xi} B d(\xi) d\xi = e^{-A_c \xi} x(t) - e^{-A_c t_0} x(t_0) \tag{2.12}$$

and solving for $x(t)$, one obtains the solution of Eq. 2.9 at any time t given by the well known convolution integral,

$$x(t) = e^{A_c (t-t_0)} x(t_0) + \int_{t_0}^{t} e^{A_c (t-\xi)} B d(\xi) d\xi \tag{2.13}$$

where $x(t_0)$ is the initial state at time $t = t_0$. Since the output term is expressed as linear combination of the state,

$$y(t) = Hx(t) + Dd(t) \tag{2.14}$$

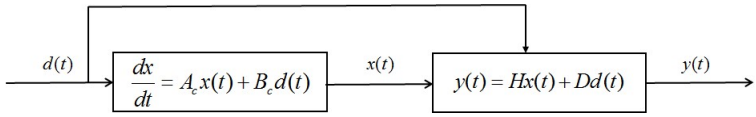

Figure 2.1: system representation by means of block diagrams.

then following that,

$$y(t) = He^{A_c(t-t_0)}x(t_0) + \int_{t_0}^{t} He^{A_c(t-\xi)}B_c d(\xi)d\xi + Dd(t) \tag{2.15}$$

The general system representation in state space form and based on block diagrams is shown in figure 2.1.

2.3 Discrete time state-space representation

Physical quantities change continuously with time since systems in real word are characterized by a continuous-time dynamics. So what happens is that sensors generate analog acquisition continuously, but computers handle with the digital sampled signal and as a consequence state estimation and control algorithms are usually implemented by means of digital electronic (Simon, 1990). In general, a continuous time invariant system can be represented by a sampled one, as follows

$$x(t) = e^{A_c(t-t_0)}x(t_0) + \int_{t_0}^{t} e^{A_c(t-\xi)}B_c d(\xi)d\xi \tag{2.16}$$

Consider the discrete sampling interval Δt and substitute $t_0 = k\Delta t$ and $t = (k+1)\Delta t$ into the above continuous solution,

$$x\left[(k+1)\,\Delta t\right] = e^{A_c\Delta t}x(k\Delta t) + \int_{k\Delta t}^{(k+1)\Delta t} e^{A_c[(k+1)\Delta t-\xi]}B_c d(\xi)d\xi \tag{2.17}$$

Then with the final change of variables $-\tau = (k+1)\Delta t - \xi$ and with some simplifications one gets,

$$x\,(k+1) = e^{A_c\Delta t}x(k\Delta t) + \int_{0}^{\Delta t} e^{-A_c\tau}B_c d(\tau)d\tau \tag{2.18}$$

and finally, posed $A_d = e^{A_c(\Delta t)}$, the solution in discrete time writes

$$x(k+1) = A_d x(k) + \int_0^{\Delta t} e^{-A_c \tau} B_c d(\tau) d\tau \tag{2.19}$$

and the general form

$$x(k+1) = A_d x(k) + B_d d(k) \tag{2.20}$$

It is evident that the integration in Eq. 2.19 depends on the inter-sample behavior of the input $d(k)$. Some assumption must be done about $d(k)$ and the parametrization for the inter sample behavior of the input can be expressed as (Bernal, 2007),

$$d(\tau) = f_0(\tau) d(k) + f_1(\tau) d(k+1) \tag{2.21}$$

where $f_0(\tau)$ and $f_1(\tau)$ are arbitrary basis function defined over the time step and with origin at the beginning of each time step. In general a finite dimensional input can be expressed in the inter-sample as follows,

$$d(\tau) = \sum_{alljs} f_j(\tau) d_{k+j} \tag{2.22}$$

Since the true analog input does not generally belong to the class that fits the discrete time state space model, for any duplet $\{f_0, f_1\}$, a residual exists between the true analog input and the sampled-based reconstruction. Substituting Eq. 2.21 into the integral in Eq. 2.19, the generic form of the discrete state space equation is expressed as (Hanselman, 1987)

$$x(k+1) = A_d x(k) + \sum_{all\ js} B_j d(k+j) \tag{2.23}$$

where

$$B_j = A_d \int_0^{\Delta t} e^{-A_c \tau} B_c f_j(\tau)\, d\tau, \textit{ for } \quad j = 0, 1 \tag{2.24}$$

The state matrices depend on the inter-sample behavior of the input; they are summarized in Table 2.1 and studied in detail in the following two subsections. More in general it is possible to parametrize the continuous-discrete relationships

Table 2.1: Closed form of the state matrices as function of the discrete assumptions on the input.

Inter sample assumption	B_0	B_1
Zero Order Hold	$(A - I)A_c^{-1}B_c$	0
First Order Hold	$(A - I)A_c^{-1}B_c - B_1$	$(A - A_c\Delta t - I)A_c^{-2}B_c/\Delta t$

as,

$$A_c = \frac{log(A_d)}{\Delta t} \tag{2.25}$$

$$B_c = (T_0 + A_d T_1)^{-1} B_d \tag{2.26}$$

$$C_c = C_d \tag{2.27}$$

$$D_c = D_d - C_c T_1 B_c \tag{2.28}$$

where

$$T_j = A_d \int_0^{\Delta t} e^{-A_c \tau} f_j(\tau) d\tau \tag{2.29}$$

2.3.1 Zero order hold

For the Zero Order Hold (ZOH) the assumption is $\{f_0, f_1\} = \{1, 0\}$, so $j = 0$. The continuous signal is sampled and holds at a certain value for all the intervals, becoming a stepwise as shown in figure 2.2. Let's assume,

$$d(\tau) = f_0(\tau) d(k) \tag{2.30}$$

Let' s define B_d, assuming that $t_0 = 0$, then,

$$\int_0^t e^{A_c(t-\tau)} B_c d(\tau) d\tau = \tag{2.31}$$

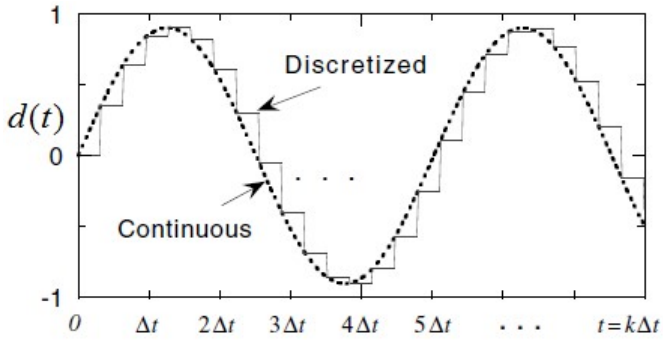

Figure 2.2: discrete and continuous signal.

$$= \int_0^t e^{A_c(t-\tau)} B_c f_0(\tau) d(k) d\tau = \tag{2.32}$$

$$= \int_0^t e^{A_c(t-\tau)} B_c 1 d(k) d\tau = \tag{2.33}$$

$$= -A_d A_c^{-1} \, e^{-A_c\tau} B_c \Big|_0^{\Delta t} d(k) = \tag{2.34}$$

$$= -A_d A_c^{-1} \left(A_d^{-1} - I \right) B_c d(k) = \tag{2.35}$$

$$= A_c^{-1} \left(A_d - I \right) B_c d(k) \tag{2.36}$$

Comparing Eqs. 2.19 and 2.20, it is evident that the ZOH solution is valid for for $B_d = A_c^{-1} \left(A_d - I \right) B_c$. In addition remembering Eq. 2.24 we define that $B_d = B_0$ and $B_1 = 0$.

2.3.2 First order hold

For the First Order Hold (FOH) the assumption is $\{f_0, f_1\} = \{1 - \tau/\Delta t, \tau/\Delta t\}$. Let's assume,

$$d(\tau) = f_0(\tau) d(k) + f_1(\tau) d(k+1) \tag{2.37}$$

This parameterization is not widely used in identification theory but is likely to be more accurate than the ZOH assuming that in this case causality is not an issue, (Bernal, 2007). The state space system becomes

$$x(k+1) = A_d x(k) + B_0 d(k) + B_1 d(k+1) \tag{2.38}$$

$$y(k) = H_d x(k) + D_d d(k) \tag{2.39}$$

The above-formulation is not in a standard discrete time state-space form due to the presence of the term $d(k+1)$. However, it is possible to convert it in standard form using the following transformation introduced by Hanselman (1987):

$$x(k) = z(k) + \sum_{all\ js} \sum_{i=1}^{j} A_d^{j-i} B_j d_{k+i-1} \tag{2.40}$$

and

$$z(k+1) = A_d z(k) + \left(\sum_{all\ js} A_d^j B_j \right) d(k) \tag{2.41}$$

$$y(k) = C_c z(k) + C_c \sum_{all\ js} \sum_{i=1}^{j} A_d^{j-1} B_j d(k+i-j) + D_c d(k) \tag{2.42}$$

In detail, for the FOH discretization,

$$x(k) = z(k) + B_1 d(k) \tag{2.43}$$

and as a consequence,

$$x(k+1) = z(k+1) + B_1 d(k+1) \tag{2.44}$$

That yields,

$$z(k+1) + B_1 d(k+1) =$$

$$= A_d x(k) + B_0 d(k) + B_1 d(k+1) = A_d[z(k) + B_1 d(k)] + B_0 d(k) + B_1 d(k+1) \tag{2.45}$$

$$z(k+1) = A_d z(k) + A_d B_1 d(k) + B_0 d(k) = A_d z(k) + \left[A_d B_1 + B_0\right] d(k) \tag{2.46}$$

and

$$y(k+1) = H_d \left[z(k) + B_1 d(k)\right] + D_d d(k) = H_d z(k) + \left[H_d B_1 + D_d\right] d(k) \tag{2.47}$$

Finally,

$$z(k+1) = A_d z(k) + \left[A_d B_1 + B_0\right] d(k) = A_2 z(k) + B_2 d(k) \tag{2.48}$$

and

$$y(k+1) = H_d z(k) + \left[H_d B_1 + D_d\right] d(k) = H_2 z(k) + D_2 d(k) \tag{2.49}$$

since

$$A_2 = A_d \tag{2.50}$$

$$B_2 = A_d B_1 + B_0 \tag{2.51}$$

$$H_2 = H_d \tag{2.52}$$

$$D_2 = H_2 B_1 + D_c \tag{2.53}$$

Let's now define B_2, assuming that $t_0 = 0$ and knowing the solution in continuous time,

$$x(t) = e^{A_c t} x(0) + \int_0^t e^{A_c (t-\tau)} B_c d(\tau) d\tau \tag{2.54}$$

The input is sampled with a FOH:

$$d(\tau) = d(k) + \frac{\tau}{\Delta t}(d(k+1) - d(k)) \tag{2.55}$$

Substituting the input above into the forced part of the solution

$$\int_0^t e^{A_c(t-\tau)} B_c d(\tau) d\tau = \int_0^t e^{A_c(t-\tau)} B_c \left(f_0(\tau) d(k) + f_1(\tau) d(k+1) \right) d\tau \tag{2.56}$$

Then we need to solve the following three integrals:

$$\int_0^{\Delta t} e^{A_c(t-\tau)} B_c d(\tau) d\tau = \tag{2.57}$$

$$= \int_0^{\Delta t} e^{A_c(t-\tau)} B_c d(k) d\tau - \int_0^{\Delta t} e^{A_c(t-\tau)} B_c \frac{\tau}{\Delta t} d(k) d\tau + \int_0^{\Delta t} e^{A_c(t-\tau)} B_c \frac{\tau}{\Delta t} d(k+1) d\tau \tag{2.58}$$

Remembering that $B_j = A_d \int_0^{\Delta t} e^{-A_c \tau} B_c f_j(\tau)\, d\tau, \quad j = 0, 1$ and that B_0 and B_1 are the two terms needed to find B_2:

$$B_0 = \int_0^{\Delta t} e^{A_c(\Delta t-\tau)} B_c f_0(\tau) d\tau =$$

$$= \int_0^{\Delta t} e^{A_c(\Delta t-\tau)} B_c d(k) d\tau - \int_0^{\Delta t} e^{A_c(\Delta t-\tau)} B_c \frac{\tau}{\Delta t} d(k) d\tau \tag{2.59}$$

$$B_1 = \int_0^{\Delta t} e^{A_c(\Delta t-\tau)} B_c f_1(\tau) d\tau = \int_0^{\Delta t} e^{A_c(\Delta t-\tau)} B_c \frac{\tau}{\Delta t} d(k+1) d\tau \tag{2.60}$$

It is possible to show that the solution for this integral results,

$$A_d (I_1 - \frac{I_2}{\Delta t}) d(k) + \frac{A_d}{\Delta t} I_2 d(k+1) \tag{2.61}$$

where

$$I_1 = A_c^{-1} \left[A_d^{-1} - I \right] B_c \tag{2.62}$$

$$I_2 = \left[-A_c^{-1} A_d^{-1} B_c \Delta t - A_c^{-2} (A_d^{-1} - I) B_c \right] \tag{2.63}$$

2.4 Observability, reconstructability and detectability

The observability (and also the recontructability and detectability) of a system is a basic concept in the estimation and control theory (Simon, 1990). A system is observable if the current state can be determined in a finite amount of time steps using both the information contained in outputs $y(t)$ and inputs $d(t)$. Since we use also the outputs in order to find the current state, we must be sure that the current state can be distinguishable from another one. The pair of states $x_1 \neq x_2 \in \mathbb{R}^{2n}$ is called indistinguishable from the output $y(\cdot)$ if for any input sequence $d(\cdot)$ the following applies,

$$y(k; x_1, d(\cdot)) = y(k; x_2, d(\cdot)), \forall k \geq 0 \tag{2.64}$$

So the system is called completely observable if no pair of states are indistinguishable from the output. The issue related to the observability process consists in determining the initial state $x(k_0)$through observations of both the inputs $d(k)$ and the outputs $y(k)$ of the actual system, for $k \geq k_0$. Let' s consider the following LTI system in discrete time,

$$\begin{cases} x(k+1) = A_d x(k) + B_d d(k) \\ y(k) = H_d x(k) + D_d d(k) \end{cases}, \; x(0) = 0 \qquad (x \in \mathbb{R}^{2n},\, d \in \mathbb{R}^r,\, y \in \mathbb{R}^m) \tag{2.65}$$

with output:

$$y(k; x_0, d(\cdot)) = H_d A_d^k x_0 + \sum_{j=0}^{k-1} H_d A_d^j B_d d(k-1-j) + D_d d(k) \tag{2.66}$$

The problem of reconstructing the initial condition from m output measurements is outlined in the following. The output recurrence is

$$\begin{cases} y(0) = H_d x_0 + D_d d(0) \\ y(1) = H_d A_d x_0 + H_d B_d d(0) + D_d d(1) \\ \vdots \\ y(N-1) = H_d A_d^{N-1} x_0 + \sum_{j=1}^{N-2} H_d A_d^j B_d d(N-2-j) + D_d d(N-1) \end{cases} \tag{2.67}$$

and we define

$$YY = \begin{bmatrix} y(0) - D_d d(0) \\ y(1) - H_d B_d d(0) - D_d d(1) \\ \vdots \\ y(N-1) - \sum_{j=1}^{N-2} H_d A_d^j B_d d(N-2-j) + D_d d(N-1) \end{bmatrix} \tag{2.68}$$

and

$$\Theta = \begin{bmatrix} H_d \\ H_d A_d \\ \vdots \\ H_d A^{N-1} \end{bmatrix} \tag{2.69}$$

So, the initial state x_0 is determined by solving the linear system

$$YY = \Theta x_0 \tag{2.70}$$

where the matrix $\Theta \in \mathbb{R}^{Nm \times 2n}$ is the observability matrix of the system. With regard eq. 2.70,

- the solution is unique if $\mathrm{rank}(\Theta) = 2n$;
- there exist infinite solutions if $\mathrm{rank}(\Theta) < 2n$; in this case, all solutions are given by $x_0 + \ker(\Theta)$, where x_0 is any particular solution of the system.

Then, assuming that the solution is unique and knowing the initial condition x_0 and the inputs, the current state for any time instant k can be easily determined,

$$x(k) = A_d^k x_0 + \sum_{i=0}^{k-1} A_d^i B_d d(k-1-i) \tag{2.71}$$

In order to find the initial state, we use the Rouch-Capelli theorem and as a consequence the system in 2.70 has a solution if

$$\mathrm{rank}(\Theta) = \mathrm{rank}([\Theta\, YY]) \tag{2.72}$$

It is possible to show that a linear system is observable if and only if $\mathrm{rank}(\Theta) = 2n$. The observability property does not depend on the input signal but only on the

matrix Θ, that means on the couple $\{A_d, H_d\}$. So the couple $\{A_d, H_d\}$ is observable if

$$\operatorname{rank}\left(\begin{bmatrix} H_d \\ H_d A_d \\ \vdots \\ H_d A_d^{2n-1} \end{bmatrix}\right) = 2n \tag{2.73}$$

We are interested in the kernel since in general $\ker(\Theta)$ is the set of states $x \in \mathbb{R}^{2n}$ that are indistinguishable from the origin for any input sequence $d(\cdot)$, which means that

$$y(k; x, d(\cdot)) = y(k; 0, d(\cdot)), \forall k \geq 0 \tag{2.74}$$

A system is observable if and only if there are no states that are indistinguishable from the origin $x = 0$ and this happens when $\ker(\Theta) = \{0\}$ or, in other words, when $\operatorname{rank}(\Theta) = 2n$. A linear system $x(k+1) = A_d x(k) + B_d d(k)$ is called reconstructable in k steps if, for each initial condition x_0, $x(k)$ is uniquely determined by $\{d(j), y(j)\}_{j=0}^{k-1}$. A system reconstructable in N steps in completely reconstructable. Finally, the linear system is detectable if it is reconstructable asymptotically for $t \to \infty$. It is useful to investigate the observability property since a system is in general endowed with sensors that allow to measure only a part of some state variables or their linear combination. The set of the measured variable form the set of the system outputs $y(\cdot)$ but there is a lack of knowledge about the dynamic field induced by a general load since the number of sensors is limited. Using the observability property of the LTI system, it is however possible to estimate the state of the system $\hat{x}(k)$ with the so called asymptotic state estimator, starting from the measurement of both the input $d(\cdot)$ and the output $y(\cdot)$, with a estimate error the asymptotically goes to zero,

$$\lim_{t \to \infty} \|x(t) - \hat{x}(t)\| = 0 \tag{2.75}$$

The asymptotic state estimator, also called the state observer, has an initial estimate error which is initially not zero and which became void after a certain amount of time since the state estimate drifts to its real state value.

2.4.1 The initial condition issue

The structure of the open loop estimator is nothing else than a “copy” of the dynamic equations of real system which uses both the input $d(t)$ and the model of the system, as shown in figure 2.3. Of course initial conditions are not known, so the output of the simulated system is biased by the error due to the lack of knowledge on initial conditions. The equations for this open loop estimator write,

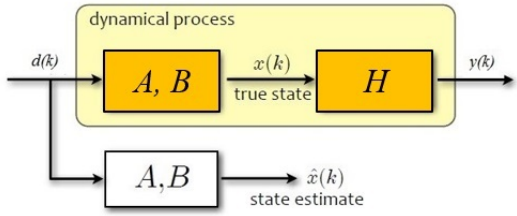

Figure 2.3: Open loop state estimator.

$$\hat{x}(k+1) = A_d\hat{x}(k) + B_d d(k) \tag{2.76}$$

The estimate error result to be

$$e(k) = x(k) - \hat{x}(k) \tag{2.77}$$

and the dynamics of the estimate error

$$e(k+1) = x(k+1) - \hat{x}(k+1) = A_d x(k) + B_d d(k) - A_d\hat{x}(k) - B_d d(k) = A_d(x(k) - \hat{x}(k)) = A_d e(k) \tag{2.78}$$

The evolution with an initial condition $e(0) = x(0) - \hat{x}(0)$ results

$$e(k) = e(0)A_d \tag{2.79}$$

It appears clear that the evolution of the error is function of the eigenvalues of the system matrix A or in other words the estimate error depends from the dynamic of the system itself. However, assuming the system stability (the system is stable since outputs are not diverging), it is not possible to arbitrarily choose with which velocity the error goes to zero. The only advantage of such a type of open loop mirrored system is that the estimator is extremely easy since it is sufficient to replicate the dynamic equations of the system.

2.4.2 Closed loop asymptotic estimator

The idea behind the closed loop asymptotic estimator is to feed back the estimation error using the available measurements, i.e. the outputs $y(t)$, through an appropriate gain used to change the asymptotic behavior of the estimator (Juang and Phan, 2001; Kailath, 1990). This is shown schematically in figure 2.4. The

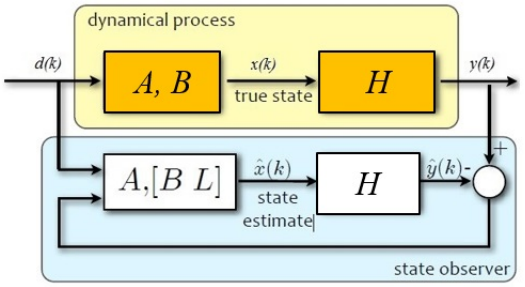

Figure 2.4: closed loop asymptotic estimator.

closed loop asymptotic estimator uses all available information. Indeed, through an appropriate choice of the feedback gain matrix L, it is possible to control the convergence rate of the estimate error. The equation of the estimator in closed loop reads,

$$\hat{x}(k+1) = A_d\hat{x}(k)+B_d d(k)+L[y(k)-H_d\hat{x}(k)] = (A_d-LH_d)\hat{x}(k)+Ly(k)+B_d d(k) \quad (2.80)$$

The initial state $x(0)$ is unknown, so one uses an initial random value on the initial state estimate $\hat{x}(0)$. The dynamic of the error estimate writes,

$$\begin{aligned} e(k+1) &= x(k+1) - \hat{x}(k+1) = \qquad (2.81)\\ &= A_d x(k) + B_d d(k) - A_d\hat{x}(k) - B_d d(k) - L[y(k) - H_d\hat{x}(k)] = \\ &= A_d x(k) - A_d\hat{x}(k) - LH_d x(k) + LH_d\hat{x}(k) = \\ &= (A_d - LH_d)(x(k) - \hat{x}(k)) = (A_d - LH_d)e(k) \end{aligned}$$

The dynamic of the error is function of the matrix $(A_d - LH_d)$ and the estimator performance is governed by the eigenvalues of this matrix. The convergence to zero is ensured by the fact that the eigenvalues have a negative real part, while the

convergence rate can be modulated by choosing the magnitude of the real part of the eigenvalues through the matrix L.

2.5 Dynamic response and Markov parameters

For discrete time model, the dynamic response to a general input is already built into the model. We simply need to compute the state at each time step,

$$x(1) = A_d x(0) + B_d d(0) \tag{2.82}$$

$$x(2) = A_d x(1) + B_d d(1) = A_d^2 x(0) + A_d B_d u(0) + B_d u(1) \tag{2.83}$$

$$x(3) = A_d x(2) + B_d d(2) = A_d^3 x(0) + A_d^2 B_d u(0) + A_d B_d u(1) + B_d u(2) \tag{2.84}$$

and so on. Eventually,

$$x(k) = A_d^k x_0 + \sum_{i=0}^{k-1} A_d^i B_d d(k-1-i) \tag{2.85}$$

and the corresponding output is

$$y(k) = H_d A_d^k x_0 + \sum_{i=0}^{k-1} H_d A_d^i B_d d(k-1-i) + D_d d(k) \tag{2.86}$$

The output equation can be rearranged in order to highlight the Markov parameters Y_k; in fact, the outputs are the result of the convolution between the Markov parameters and the input load.

$$y(k) = H_d A_d^k x_0 + \begin{bmatrix} D_d & H_d B_d & H_d A_d B_d & H_d A_d^2 B_d & \dots & H_d A_d^{k-1} B_d \end{bmatrix} \begin{bmatrix} d(k) \\ d(k-1) \\ \dots \\ \dots \\ d(1) \\ d(0) \end{bmatrix} \tag{2.87}$$

or

$$\begin{bmatrix} y(k) \\ y(k-1) \\ ... \\ ... \\ y(1) \\ y(0) \end{bmatrix} = \begin{bmatrix} H_d A_d^k \\ H_d A_d^{k-1} \\ ... \\ ... \\ H_d A_d \\ H_d \end{bmatrix} x_0 + \begin{bmatrix} Y_0 & Y_1 & Y_2 & Y_3 & ... & Y_k \\ 0 & Y_0 & Y_1 & Y_2 & ... & ... \\ 0 & 0 & Y_0 & Y_1 & Y_2 & Y_3 \\ 0 & 0 & 0 & Y_0 & Y_1 & Y_2 \\ 0 & 0 & 0 & 0 & Y_0 & Y_1 \\ 0 & 0 & 0 & 0 & 0 & Y_0 \end{bmatrix} \begin{bmatrix} d(k) \\ d(k-1) \\ ... \\ ... \\ d(1) \\ d(0) \end{bmatrix} \tag{2.88}$$

For zero initial condition, the well know formulation of the impulse response holds,

$$y(t) = Md(t) \tag{2.89}$$

We note that the solution to the same input $d(k)$ is not the same if we are integrating the differential equation in continuous time or if we are solving the difference equation in discrete time. In discrete time, the response is due to the discretized version of $d(k)$.

2.6 LQR and LQG controller

In this chapter we introduce the basic equations of the Optimal Linear Quadratic Regulator (LQR) in continuous and discrete time and finite/infinite horizon.

2.6.1 LQR in continuous time and finite/infinite horizon

Assuming the linear system in continuous time

$$\dot{x}(t) = A_c x(t) + B_c u(t) \tag{2.90}$$

Let's start using a finite time horizon; the objective is to minimize the following quadratic cost function within the time interval $[t_0, ..., t_1]$,

$$J = x(t_1)^T M x(t_1) + \int_{t_0}^{t_1} (x(t)^T Q x(t) + u(t)^T R u(t)) dt \tag{2.91}$$

The control law results to be,

$$u(t) = -K_{LQR}(t) x(t) \tag{2.92}$$

where $K_{LQR}(t) = R^{-1} B_c^T P(t)$ and $P(t)$ is the solution of the Riccati differential equation in continuous time

$$-\dot{P}(t) = A_c^T P(t) + P(t) A_c - P(t) B_c R^{-1} B_c^T P(t) + Q \tag{2.93}$$

Let's now take the infinite time horizon; the objective now is to minimize the following quadratic cost function within the time interval $[t_0, ..., \infty]$,

$$J = \int_{t_0}^{t_\infty} (x(t)^T Q x(t) + u(t)^T R u(t)) dt \tag{2.94}$$

The control law results to be,

$$u(t) = -K_{LQR}(t) x(t) \tag{2.95}$$

where $K_{LQR}(t) = R^{-1} B_c^T P_\infty$ and P_∞ is the solution of the Riccati differential equation in continuous time

$$0 = A_c^T P_\infty + P_\infty A_c - P_\infty B_c R^{-1} B_c^T P_\infty + Q \tag{2.96}$$

2.6.2 LQR in discrete time and finite/infinite horizon

Assuming the linear system in discrete time

$$x(k+1) = A_d x(k) + B_d u(k) \tag{2.97}$$

Let's start using a finite time horizon; the objective is to minimize the following quadratic cost function within the time interval $[k_0, ..., k_1]$,

$$J = \sum_{i=k_0}^{k_1} (x(k)^T Q x(k) + u(k)^T R u(k)) \tag{2.98}$$

The control law results to be,

$$u(k) = -K_{LQR}(k) x(k) \tag{2.99}$$

where $K_{LQR}(k) = (R^T + B_d^T P(k) B_d)^{-1} B_d^T P(k) A_d$ and $P(k-1)$ is the solution of the Riccati algebraic equation in discrete time

$$P(k-1) = A_d^T (P(k) - P(K) B_d (R + B_d^T P(k) B_d)^{-1} B_d^T P(k)) A_d + Q \tag{2.100}$$

Let's now take the infinite time horizon; the objective now is to minimize the following quadratic cost function within the time interval $[k_0, ..., \infty]$,

$$J = \sum_{i=k_0}^{\infty} (x(k)^T Q x(k) + u(k)^T R u(k)) \tag{2.101}$$

The control law results to be,

$$u(k) = -K_{LQR}(k)x(k) \tag{2.102}$$

where $K_{LQR}(k) = (R^T + B_d^T P_\infty B)^{-1} B_d^T P_\infty A_d$ and P_∞ is the solution of the Riccati algebraic equation in discrete time

$$P_\infty = A_d^T (P_\infty - P_\infty B_d (R + B_d^T B_d)^{-1} B_d^T) A_d + Q \tag{2.103}$$

2.7 Modal domain

The dynamic behavior of structures can be settled by only few vibrational modes (Ewins, 2000). It can be useful to project the problem into the modal domain. Starting from the equation of motion in continuous time,

$$M\ddot{u}(t) + C\dot{u}(t) + Ku(t) = Sd(t) \tag{2.104}$$

The change of coordinates writes,

$$u(t) = \Phi q(t) \tag{2.105}$$

The introduction of modal coordinates and the pre-multiplication by Φ^T, yields

$$\Phi^T M \Phi \ddot{u}(t) + \Phi^T C \Phi \dot{u}(t) + \Phi^T K \Phi u(t) = \Phi^T S d(t) \tag{2.106}$$

and assuming proportional damping, the decoupled system becomes

$$I\ddot{q}(t) + \Gamma\dot{q}(t) + \Omega^2 q(t) = \Phi^T S d(t) \tag{2.107}$$

where the diagonal matrix $\Omega \in \mathbb{R}^{nxn}$ collects the n eigenfrequencies. The state space system in modal domain given $\zeta = \dfrac{q(t)}{\dot{q}(t)}$, results

$$\dot{\zeta}(t) = \begin{bmatrix} 0 & I \\ -\Omega^2 & -\Gamma \end{bmatrix} \zeta(t) + \begin{bmatrix} 0 \\ \Phi^T S \end{bmatrix} d(t) \tag{2.108}$$

or

$$\dot{\zeta}(t) = A_m \zeta(t) + B_m d(t) \tag{2.109}$$

with $A_m \in \mathbb{R}^{2nx2n}$, $B_m \in \mathbb{R}^{2nxr}$, $\zeta \in \mathbb{R}^{2n}$ and$d(t) \in \mathbb{R}^r$. With regard to the measurement equation, displacement, velocity and acceleration measurement can easily be projected in the modal domain

$$y(t) = R_d u(t) = R_d \Phi q(t) \tag{2.110}$$

$$y(t) = R_v \dot{u}(t) = R_{v\Phi} \dot{q}(t) \tag{2.111}$$

$$y(t) = R_a \ddot{u}(t) = R_a \Phi \ddot{q}(t) \tag{2.112}$$

with R_d, R_v and $R_a \in \mathbb{R}^{nxn}$ allowable to selecting for the real position of displacement, velocity and acceleration measurements, respectively. In turn, acceleration can be written as,

$$I\ddot{q}(t) = -\Gamma \dot{q}(t) - \Omega^2 q(t) + \Phi^T S d(t) \tag{2.113}$$

and substituting (in the case of acceleration data),

$$y(t) = -R_a \Phi \Gamma \dot{q}(t) - R_a \Phi \Omega^2 q(t) + R_a \Phi \Phi^T S d(t) \tag{2.114}$$

or

$$y(t) = \begin{bmatrix} -R_a \Phi \Omega^2 & -R_a \Phi \Gamma \end{bmatrix} \begin{pmatrix} q(t) \\ \dot{q}(t) \end{pmatrix} + \left[R_a \Phi \Phi^T S \right] d(t) \tag{2.115}$$

Collecting different types of measurements, the output equation write

$$y(t) = \begin{bmatrix} u(t) \\ \dot{u}(t) \\ \ddot{u}(t) \end{bmatrix} = \begin{bmatrix} R_d \Phi & 0 \\ 0 & R_v \Phi \\ -R_a \Phi \Omega^2 & -R_a \Phi \Gamma \end{bmatrix} \zeta(t) + \begin{bmatrix} 0 \\ 0 \\ R_a \Phi \Phi^T S \end{bmatrix} d(t) \tag{2.116}$$

or easily

$$y(t) = H_m \zeta(t) + D_m d(t) \tag{2.117}$$

with $H_m \in \mathbb{R}^{mx2n}$, $D_m \in \mathbb{R}^{mxr}$, $\zeta \in \mathbb{R}^{2n}$ and $d(t) \in \mathbb{R}^r$.

2.8 Model reduction

It is often necessary to cut off the problem dimension because of computational issues by means of a model reduction. When the reduction is performed, the dynamics of the system is represented by a reduced number N of modal coordinates. $\zeta_r(t) \in \mathbb{R}^{2N}$ is the modal state vector and the state vector is just a linear combination of N modes where

$$u(t) \simeq \Phi_r q(t) \tag{2.118}$$

$$\Phi_r^T M \Phi_r \ddot{u}(t) + \Phi_r^T C \Phi_r \dot{u}(t) + \Phi_r^T K \Phi_r u(t) = \Phi \Phi^T S d(t) \tag{2.119}$$

The expression for modal acceleration becomes

$$I\ddot{q}_r(t) + \Gamma_r \dot{q}_r(t) + \Omega_r^2 q_r(t) = \Phi_r^T S d(t) \tag{2.120}$$

and the modal reduced model in state space yields,

$$\dot{\zeta}_r(t) = A_{m,r}\zeta_r(t) + B_{m,r} d(t) \tag{2.121}$$

with $A_m \in \mathbb{R}^{2Nx2N}$, $B_m \in \mathbb{R}^{2Nxr}$, $\zeta \in \mathbb{R}^{2N}$ and $d(t) \in \mathbb{R}^r$. With regard to the output equation,

$$y(t) = \begin{bmatrix} u(t) \\ \dot{u}(t) \\ \ddot{u}(t) \end{bmatrix} = \begin{bmatrix} R_d \Phi_r & 0 \\ 0 & R_v \Phi_r \\ -R_a \Phi_r \Omega_r^2 & -R_a \Phi_r \Gamma_r \end{bmatrix} \zeta_r(t) + \begin{bmatrix} 0 \\ 0 \\ R_a \Phi_r \Phi_r^T S \end{bmatrix} d(t) \tag{2.122}$$

or easily

$$y(t) = H_{m,r}\zeta(t)_r + D_{m,r} d(t) \tag{2.123}$$

with $H_{m,r} \in \mathbb{R}^{mx2N}$, $D_m \in \mathbb{R}^{mxr}$, $\zeta \in \mathbb{R}^{2N}$ and $d(t) \in \mathbb{R}^r$.

CHAPTER 3

THE KALMAN FILTER THEORY FOR INPUT AND STATE ESTIMATION

3.1 Introduction

Theory of state estimations stems from the necessity of estimating instantaneous state of a linear dynamic system by means of the output measurements which are both linearly related to the state and corrupted by noise. The state estimation arises from the fact that the control of complex dynamic systems need the knowledge of the motion field, but the availability of measurement points is limited and it not possible to measure all wanted variables.

The beginning of optimal estimation theory and of optimal estimate from noisy data is the least squares method, established by the early 1800s with the work of Gauss (1809). Then Norbert Wiener gave impulse to the theory of prediction, smoothing and filtering and to the theory of ergodic processes. The report titled “Extrapolation, interpolation and smoothing of stationary time series” dates back to the late 1940s (Wiener, 1949). In 1960 Kalman (1960) published the milestone contribution to the linear filtering and prediction problems with the well known Kalman Filter (KF). The Kalman Filter provides a means for optimally inferring, indeed it proves to be the optimal linear estimator for systems subjected to gaussian disturbances with gaussian measurement noise. The concept of filter grows in the 1930s and 1940s in the meaning of separation of signals from noise, both characterized by their power spectral densities. In addition the KF also includes the idea related to the solution of an inverse problem since it basically reconstructs the independent random variables starting from the dependent but measurable one. In this

chapter the basic concepts about the linear Kalman filter for state and input identification are introduced. Then the Chapter the focus shifts on the non-linear version of the filter and on its utilization as state and parameter estimator for non-linear systems.

3.2 The Kalman Filter

The model considered by the KF has uncertainties related to:

- unknown inputs;
- discrepancies between the real system and the analytical model;
- unknown initial conditions.

The KF is a recursive data processing algorithm, which provides the optimal state estimate of the system that is subjected to stationary stochastic disturbances with known covariances. More precisely, the Filter computes the conditional mean and covariance of the probability distribution of the state of the linear stochastic system with noises defined in the following. Let's consider the following time invariant linear system in discrete time,

$$x_k = Ax_{k-1} + Bu_{k-1} + Gw_{k-1} \tag{3.1}$$

$$y_k = Hx_k + v_k \tag{3.2}$$

where the system matrix are $A \in \mathbb{R}^{2nx2n}$, $B \in \mathbb{R}^{2nxr}$, $H \in \mathbb{R}^{mx2n}$ and $G \in \mathbb{R}^{2n}$. $x_k \in \mathbb{R}^{2n}$ is the state vector, $d_k \in \mathbb{R}^r$ is the deterministic input and $y_k \in \mathbb{R}^m$ is the available measurement vector. The sequence $w_k \in \mathbb{R}^{2n}$ is the known disturbance also known as process noise and $v_k \in \mathbb{R}^m$ is the measurement noise. It is assumed that the noises are Gaussian stationary white noise with zero mean and known covariance matrices (although these assumptions are quite distant from reality),

$$\begin{aligned} &E(x_k) = \hat{x_0} \\ &E((x_0 - \hat{x_0})(x_0 - \hat{x_0})^T) = P_0 \end{aligned} \tag{3.3}$$

$$E(w_k) = 0 \tag{3.4}$$

$$E(v_k) = 0 \tag{3.5}$$

and

$$E(w_k w_j^T) = Q\delta_{kj} \tag{3.6}$$

$$E(v_k v_j^T) = QR\delta_{kj} \tag{3.7}$$

$$E(w_k v_j^T) = 0 \tag{3.8}$$

where δ_{kj} is the Kronecker Delta. In addition, the state is uncorrelated with respect to the noises, i. e.

$$E(x_k w_j^T) = 0 \tag{3.9}$$

$$E(x_k v_j^T) = 0 \tag{3.10}$$

3.2.1 The state estimator

A linear estimator for a LTI is,

$$\hat{x}_{k+1} = F\hat{x}_k + Zd_k + L_k y_k \tag{3.11}$$

where $\hat{x}_k$ is the estimate of x_k and L_k is the observer gain. Let's define the error between the real state and its estimate,

$$e_k = x_k - \hat{x}_k \tag{3.12}$$

and substituting for the time station $k+1$ Eq. 3.1 and Eq. 3.2 into Eq. 3.12, it holds,

$$e_{k+1} = (A - L_k H_k)x_k + (B - Z)d_k + Gw_k + F\hat{x}_k - L_k v_k \tag{3.13}$$

replacing x_k with $\hat{x}_k - e_k$,

$$e_{k+1} = (A - L_k H_k)(\hat{x}_k - e_k) + (B - Z)d_k + Gw_k + F\hat{x}_k - L_k v_k \tag{3.14}$$

reordering

$$e_{k+1} = (A - L_k H_k)e_k + (B - Z)d_k + Gw_k + (A - L_k H - F)\hat{x}_k - L_k v_k \tag{3.15}$$

and taking the expected value of Eq. 3.15 and knowing Eqs. 3.4 and 3.5, one finally obtains,

$$E(e_{k+1}) = (A - L_k H_k)E(e_k) + (B - Z)E(d_k) + (A - L_k H - F)E(\hat{x}_k) \tag{3.16}$$

Since the expected values of the state estimate and of the input are not necessarily zero and since we want that the expected value of the error is zero, it is necessary that,

$$Z = B \tag{3.17}$$

and

$$F = A - L_k H \tag{3.18}$$

So the error in the time station $k + 1$ is a function of the error and the noises at the previous step,

$$e_{k+1} = (A - L_k H_k)e_k + Gw_k - L_k v_k \tag{3.19}$$

and its expected value

$$E(e_{k+1}) = (A - L_k H_k)E(e_k) \tag{3.20}$$

Hence, it is necessary that

$$lim_{k\to\infty} E(e_{k+1}) = 0 \tag{3.21}$$

or, in other words the eigenvalues of the matrix $(A - L_k H)$ must be inside the unit circle in the complex plane.

3.2.2 Innovation form of the Filter

Let's define now the error in the state before and after the measurement update reads,

$$e_k^- = x_k - \hat{x}_k^- \tag{3.22}$$

$$e_k^+ = x_k - \hat{x}_k^+ \tag{3.23}$$

where $\hat{x}_k^-$ is the a priori estimate and $\hat{x}_k^+$is the a posteriori estimate. The covariance of the estimation error before and after the update

$$P_k^- = E[e_k^- {e_k^-}^T] = E[(x_k - \hat{x}_k^-)(x_k - \hat{x}_k^-)^T] \tag{3.24}$$

$$P_k^+ = E[e_k^+ {e_k^+}^T] = E[(x_k - \hat{x}_k^+)(x_k - \hat{x}_k^+)^T] \tag{3.25}$$

We postulate the existence of the state estimate before and after that information from measurements became available, so

$$\hat{x}_k^- = A\hat{x}_{k-1}^+ + Bd_{k-1} \tag{3.26}$$

$$\hat{x}_k^+ = \hat{x}_k^- + K_k(y_k - H\hat{x}_k^-) \tag{3.27}$$

The first step represented by Eq. 3.26 identifies the prediction step of the Filter, while in the second step, an update of the current a priori state estimate occurs since the first estimate is corrected by the measurement vector that now is available. The a priori estimate error writes

$$e_k^- = Ax_{k-1} + Bd_{k-1} + Gw_{k-1} - A\hat{x}_{k-1}^+ - Bd_{k-1} \tag{3.28}$$

which reduces to

$$e_k^- = Ae_{k-1}^+ + Gw_{k-1} \tag{3.29}$$

and its the covariance results

$$P_k^- = AP_{k-1}^+ A^T + GQG^T \tag{3.30}$$

Then, let's take the a posteriori state estimate and use the substitution of Eq. 3.2,

$$\hat{x}_k^+ = \hat{x}_k^- + K_k(Hx_k + v_k - H\hat{x}_k^-) \tag{3.31}$$

substituting Eq. 3.23 into Eq. 3.31, yields

$$x_k - e_k^+ = x_k - e_k^- + K_k(Hx_k + v_k - H\hat{x}_k^-) \tag{3.32}$$

and reorganizing

$$e_k^+ = e_k^- - K_k(He_k^- + v_k) \tag{3.33}$$

So the second important result is the covariance of the a posteriori estimation error

$$P_k^+ = E[e_k^+ e_k^{+^T}] = E[(e_k^- - K_k(He_k^- + v_k))(e_k^- - K_k(He_k^- + v_k))^T] \tag{3.34}$$

$$P_k^+ = P_k^- - P_k^- H^T K_k + K_k R K_k^T - K_k H P_k^- - K_k H P_k^- H^T K_k^T \tag{3.35}$$

The goal is to find the gain $K_k$that minimizes this a posteriori covariance. Taking the derivative of Eq. 3.35 with respect to K_k, gives

$$K_k = P_k^- H^T (HP_k^- H^T + R)^{-1} \tag{3.36}$$

finally after obtaining the gain, we can reformulate the expression for the a posteriori covariance,

$$P_k^+ = (I - K_k H)P_k^- \tag{3.37}$$

The filter steps are summarized in table 3.1

3.2.3 The steady state form of the Filter

The formulation for the steady state version of the filter is quite similar. The difference resides in the fact that the covariance and the filter gain are not changing

Table 3.1: Discrete-Time filter equation.

Time update equations
$\hat{x}_k^- = A\hat{x}_{k-1} + Bd_{k-1}$
$P_k^- = AP_{k-1}^+A^T + GQG^T$
Measurement update equations
$K_k = P_k^- H^T(HP_k^- H^T + R)^{-1}$
$\hat{x}_k^+ = \hat{x}_k^- + K_k(y_k - H\hat{x}_k^-)$
$P_k^+ = (I - K_k H)P_k^-$

in time since once the transient response due to the error in the initial estimate $\hat{x}_0$ is dissipated, the state estimation error become stationary and consequently the error covariance converges at the steady state value. The steady state value is available from the solution of the discrete algebraic Riccati Equation

$$P = APA^T - APH^T(HPH + R)^{-1}HPA^T + GQG^T \tag{3.38}$$

This equation can be solved under conditions of uniqueness:

- A is stable
- the pair (A, H) is observable
- the pair $(A, GQG^T)$is controllable
- $R > 0$
- $GQG^T > 0$.

Similarly the gain results to be

$$K = PH^T(HPH^T + R)^{-1} \tag{3.39}$$

3.2.4 The Kalman-Bucy filter

The Kalman-Bucy filter is the continuous form of the filter. The continuous-time random process $x(t)$ and the observations are given by

$$\dot{x}(t) = A_c(t)x(t) + B_c(t)d(t) + G_c w(t) \tag{3.40}$$

$$y(t) = H_c(t)x(t) + v(t) \tag{3.41}$$

with, as usual

$$E[w(t)v^T(\tau)] = 0 \ \forall t, \tau \geq 0 \tag{3.42}$$

$$E[w(t)w^T(\tau)] = Q(t)\delta(t-\tau) \tag{3.43}$$

$$E[v(t)v^T(\tau)] = R(t)\delta(t-\tau) \tag{3.44}$$

$$E[x_0] = \bar{x}_0 \qquad E[(x-\bar{x}_0)(x-\bar{x}_0)^T] = P_0 \tag{3.45}$$

$$E[x_0 w^T(t)] = 0 \qquad E[x_0 v^t(t)] = 0 \tag{3.46}$$

The observer

$$\dot{\hat{x}}(t) = A_c(t)\hat{x}(t) + B_c(t)d(t) + K(t)[y(t) - H_c(t)\hat{x}(t)] \tag{3.47}$$

whilst the matrix Riccati differential equation to be solved reads,

$$\dot{P}(t) = A_c(t)P(t) + P(t)A_c^T(t) - P(t)H_c^T(t)R^{-1}(t)H_c(t)P(t) + Q(t) \tag{3.48}$$

and the gain in continuous time results,

$$K(t) = P(t)H_c^T(t)R^{-1}(t) \tag{3.49}$$

3.3 The Kalman Filter for input identification

Kalman filter for input identification is attractive since it is a model based method that allows minimum variance estimation of the input without a priori information about the dynamic evolution of the input forces. The Kalman filter for force identification includes unknown forces in the state vector and estimates the loads in conjunction with the states. As usual noise on both measurements and state variables is modeled as a stochastic process. Techniques based on filters stand out from purely deterministic methods in which no errors are added to the state system. In the following there are the main results about this application.

3.3.1 RLS approach

Tuan et al. (1996) and Tuan et al. (1997) show a Kalman-like observer joined with a Recursive Least Square (RLS) approach in order solve a typical Inverse Heat Conduction Problem (IHCP). In such a problem, it is desired to estimate the unknowns of a thermal system (heat fluxes or heat sources) providing temperature measurements in the interior of the body. In the papers, the goal is to estimate the thermal unknowns by using temperature measurements in order to estimate both the states and the operating load. The algorithm consists in two parts: the Kalman filter and the Recursive Least Square weighted by a forgetting factor.

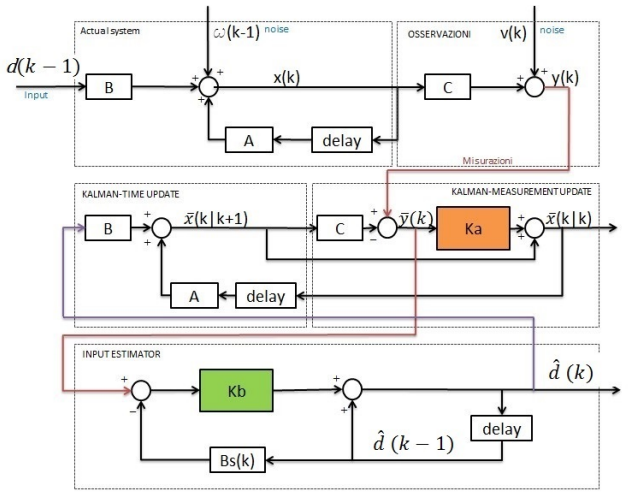

Figure 3.1: state and input observer layout.

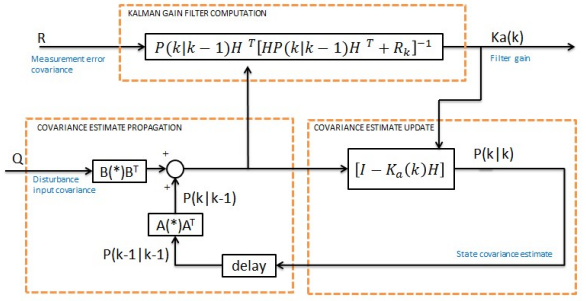

Figure 3.2: the Kalman observer.

Step	Equation
State	$x_{k+1} = Ax_k + Bd_k + w_k$
Measurements	$y_k = Hx + v_k$
Initialization	$\hat{x}_{k-1\|k-1}, P_{k-1\|k-1}, d_{k-1}, P_{b,k-1}$
Optimal Kalman observer	
A priori state estimate	$\hat{x}_{k\|k-1} = A\hat{x}_{k-1\|k-1} + B\hat{d}_{k-1}$
A priori error covariance	$P_{k\|k-1} = AP_{k-1\|k-1}A^T + BQB^T$
Innovation covariance	$S_k = HP_{k\|k-1}AH^T + R$
Kalman gain	$K_{a,k} = P_{k\|k-1}H^T S_k^{-1}$
Innovation	$\hat{y}_k = y_k - H\hat{x}_{k\|k-1}$
A posteriori state estimate	$\hat{x}_{k\|k} = \hat{x}_{k\|k-1} - K_{a,k}$
A posteriori error covariance	$P_{k\|k} = [I - K_{a,k}H]P_{k\|k-1}$
Recursive least square algorithm	
Sensitivity matrices	$M_k = [I - K_{a,k}H][AM_{k-1} + I]$
	$B_{s,k} = H[AM_{k-1} + I]B$
Input estimate gain	$K_{b,k} = \gamma^{-1}P_{b,k-1}B_{s,k}^T[B_{s,k}^T\gamma^{-1}P_{b,k-1}B_{s,k}^T S_{k-1}]^{-1}$
Error covariance	$P_{b,k} = [I - K_{b,k}B_{s,k}]\gamma^{-1}P_{b,k-1}$
Input estimate	$\hat{d}_k = \hat{d}_{k-1} + K_{b,k}[\hat{y}_k - B_{s,k}\hat{d}_{k-1}]$

Table 3.2: RLS algorithm

The Kalman filter generates the recursive relation between the observed value of the innovation without knowledge of the input and the theoretical residual assuming that the input is obtained. In this relationship there is a deterministic bias due to the unknown input and a random bias due to the process and measurement noise. In the meanwhile, the RLS algorithm uses the residual to extract the estimated deterministic input.The adaptive procedure can be implemented on-line. The starting point is the discrete time invariant system and the complete observer layout is in figure 3.1. In this procedure, the Kalman filter acts as a ”bias free“ estimator and the RLS function as a ”bias“ estimator. The input gain minimizes the difference between actual and estimated loads; the forgetting factor weights the error on the input estimate by giving less importance to the oldest samples. Details of the algorithm are shown in figures 3.2 and 3.3. In Table 3.2 is reported the

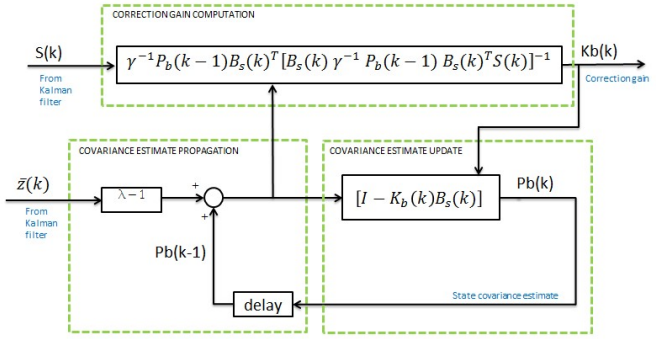

Figure 3.3: the RLS observer.

whole algorithm. The application of the Kalman Filter with a recursive estimator is also used in Liu et al. (2000) in order to determine the input force of a cantilever plate.

3.3.2 Minimum-Variance Unbiased input and state estimation algorithms

In (Gillijns and De Moor, 2007a,b), an extension of methods presented in Kitanidis (1987) and Darouach and Zasadzinski (1997) is presented and necessary and sufficient conditions of the method are discussed. The paper addresses the problem of unknown input identification without a priori knowledge on the input model and in the same time assumes optimality conditions leading to a Minimum-Variance

Unbiased (MVU) input and state estimation. The recursive filter is used on linear discrete-time system in order to jointly estimate the state and the input. The input estimate is obtained through a least square procedure and the extended state estimate is obtained from a standard Kalman approach. Results are coherent with both the Kitanidis (1987) and Darouach and Zasadzinski (1997) state estimation, and with the input estimation of Hsieh (2000). Consider the Linear Time Invariant (LTI) discrete-time system,

$$x_{k+1} = Ax_k + Bd_k + w_k \tag{3.50}$$

$$y_k = Hx_k + v_k \tag{3.51}$$

where $x_k \in \mathbb{R}^{2n}$ is the state vector, $d_k \in \mathbb{R}^r$ is the unknown input and $y_k \in \mathbb{R}^m$ is the measurement vector. The process noise $w_k \in \mathbb{R}^{2n}$ and the measurement noise $v_k \in \mathbb{R}^m$ are assumed to be mutually uncorrelated, zero-mean, white random signals with covariance matrices Q_k and R_k.The input has unknown model and no a priori assumption is made on it. The relevant pseudo-code results to be,

- Initialization: $x_0 = \hat{x}_{k-1|k-1}$, $P_0 = P_{k-1|k-1}$.
- Input estimation:
  1. $\hat{x}_{k|k-1} = A\hat{x}_{k-1|k-1}$is biased by the unknown input
  2. $P_{k|k-1} = AP_{k-1|k-1}A^T + Q$
  3. $\tilde{R}_k = HP_{k-1|k-1}AH^T + R$
  4. $M_k = (F_k^T \tilde{R}_k^{-1} F_k) F_k^T \tilde{R}_k^{-1}$, where $F_k = HB$
  5. $d \hat{-} 1_k = M_k(y_k - H\hat{x}_{k|k-1})$ is the MVU estimate of the unknown input given the innovation $y_k - H\hat{x}_{k|k-1}$.
- State estimation:

State update

1. $\hat{x}^*_{k|k} = \hat{x}_{k|k-1} + B\hat{d}_{k-1}$is the unbiased state estimate of x_k
2. $K_k = P_{k|k-1}H^T\tilde{R}_k^{-1}$ where the matrix K_k minimizes the variance of $\hat{x}_{k|k}$

3. $P^*_{k|k} = (I_n - BM_kH)P_{k|k-1}(I_n - BM_kH)^T + BM_kRM_k^TB^T$.

Measurement update

1. $\hat{x}_{k|k} = \hat{x}^*_{k|k} + K_k(y_k - H\hat{x}^*_{k|k})$ is the MVU estimator of x_k
2. $S^*_k = -BM_kR$
3. $P_{k|k} = P^*_{k|k} - K_k(P^*_{k|k}H^T + S^*_k)^T$.

Consider now the Linear Time Invariant (LTI) discrete-time system:

$$x_{k+1} = Ax_k + Bd_k + w_k \tag{3.52}$$

$$y_k = Hx_k + Dd_k + v_k \tag{3.53}$$

where $x_k \in \mathbb{R}^{2n}$ is the state vector, $d_k \in \mathbb{R}^r$ is the unknown input and $y_k \in \mathbb{R}^m$ is the measurement vector. The process noise $w_k \in \mathbb{R}^{2n}$ and the measurement noise $n_k \in \mathbb{R}^m$ are assumed to be mutually uncorrelated, zero-mean, white random signals with covariance matrices Q_k and R_k. The input has unknown model and no a priori assumption is made on it. The matrices A, B, H, D are known but the algorithm can be applied to time-variant system substituting A, B, H, D with A_k, B_k, H_k, D_k. It is possible to extend this procedure also to linear discrete-time system with direct feedthrough (Gillijns and De Moor, 2007a). The estimation of input and state is still joined: the input estimate is developed with a Weighted Least-Square approach (WLS), while the state estimate is performed using the Kitanidis (1987) approach. On the one hand, the state estimation problem is conceptually the same but on the other hand the input estimation problem is different in the two cases. The main difference lies on the delay on the input estimate. In absence of the direct feedthrough term, it is possible to estimate the input at time $k-1$ through information at $k|k-1$, since the first useful information about $\hat{d}_{k-1}$ comes from $\hat{y}_{k|k-1}$. Dually, in presence of the feedthrougth term, it is possible to acquire information about $\hat{d}_k$ by means of $\hat{y}_{k|k-1}$, directly and without delay. As a consequence, the first usefull information depends on Δt and on distances between inputs and outputs. An unbiased minimum-variance input estimate is eventually obtained from innovation term. Relevant recursive equations are here reported:

- Initialization: $x_0 = \hat{x}_{k|k-1}$, $P_0^x = P_{k|k-1}^x$.
- Input estimation:
  1. $\tilde{R}_k = HP_{k|k-1}AH^T + R$
  2. $P_k^d = (D\tilde{R}_k^{-1}D^T)^{-1}$
  3. $M_k = P_k^d D^T \tilde{R}_k^{-1}$
  4. $\hat{d}_k = M_k(y_k - H\hat{x}_{k|k-1})$ is the MVU estimate of the unknown input given the innovation $y_k - H\hat{x}_{k|k-1}$.
- State estimation:

Measurement update

1. $K_k = P_{k|k-}^x H^T \tilde{R}_k^{-1}$
2. $\hat{x}_{k|k} = \hat{x}_{k|k-1} + K_k(y_k - H\hat{x}_{k|k-1} - D\hat{d}_k)$
3. $P_{k|k}^x = P_{k|k-1}^x - K_k(\tilde{R}_k - DP_k^d D^T)K_k^T$
4. $P_k^{xd} = (P_k^{dx})^T = -K_k D P_k^d$

Time update

1. $\hat{x}_{k+1|k} = A\hat{x}_{k|k} + B\hat{d}_k$
2. $P_{k+1|k}^x = \begin{bmatrix} A & B \end{bmatrix} \begin{bmatrix} P_{k|k}^x & P_k^{xd} \\ P_k^{dx} & P_k^d \end{bmatrix} \begin{bmatrix} A^T \\ B^T \end{bmatrix} + Q$

Lastly, time update and measurement update equations are the same used in the Kalman filter with the significant difference that the unknown input is obtained from a least square estimation. The input estimate relies on the state covariance matrix and in turn the state estimate depends from the innovation taking into account for the input estimate.

3.3.3 The steady state observer method

Hwang et al. (2009) developed a procedure to estimate external loads using measured structural response and a steady state Kalman filter scheme. The procedure is reported in table 3.3. The estimation method is formulated in a closed-loop form in the modal space to define, in the frequency domain, the transfer function from actual load to estimated load. This method is applied to a SDoF system

subjected to sinusoidal load and to a MDoF system subjected to wind load, respectively. Wind load identification using steady state Kalman filter is extensively presented also in (Hwang et al., 2009). The scheme starts, as usual, from the system dynamic. The Kalman gain is obtained starting from the solution of the algebraic

Table 3.3: the steady state observer

Metric domain		Modal domain
$x_{k+1} = Ax_k + Bd_k$	actual state	$\zeta_{k+1} = A_m\zeta_k + B_m d_k$
$y_k = Hx_k + Dd_k + v_k$	actual meas.	$y_k = H_m\zeta_k + D_m d_k + v_k$
$\hat{x}_{k+1} = (A - KH)\hat{x}_k + Ky_k$	estimated state	$\hat{\zeta}_{k+1} = (A_m - K_m H_m)\hat{\zeta}_k + K_m y_k$
$\hat{y}_k = H\hat{x}_k$	estimated meas.	$\hat{y}_k = H_m\hat{\zeta}_k$
$\hat{x}_{k+1} = A\hat{x}_k + B\hat{d}_k$	at convergence	$\hat{\zeta}_{k+1} = A_m\hat{\zeta}_k + B_m\hat{d}_k$
$\hat{d}_k = B^+(\hat{x}_{k+1} - A\hat{x}_k)$		$\hat{d}_k = B_m^+(\hat{x}_{k+1} - A_m\hat{x}_k)$
$\hat{x}_{k+1} - A\hat{x}_k = K(y_k - H\hat{x}_k)$		$\hat{\zeta}_{k+1} - A_m\hat{\zeta}_k = K_m(y_k - H_m\hat{\zeta}_k)$
$\hat{d}_k = B^+K(y_k - H\hat{x}_k)$	estimated load	$\hat{d}_k = B_m^+K_m(y_k - H_m\hat{\zeta}_k)$

Riccati equation and it is used in steady state form in order to identify modal wind load. Hwang et al. (2011) extended the method to a rectangular shaped concrete chimney, by making use of measured responses from an aeroelastic wind tunnel tests.

3.4 Introduction to non-linear filters

The usual applications of the non-linear filtering are:

- the state estimation

Given the observations y_k the goals is to estimate the state x_k of the following discrete-time non-linear system

$$\begin{aligned} x_{k+1} &= f(x_k, d_k, w_k) \\ y_k &= h(x_k, v_k) \end{aligned} \tag{3.54}$$

with the unobserved state vector $x_k \in \mathbb{R}^{2n}$, the known exogenous input $d_k \in \mathbb{R}^r$, the measurements vector $y_k \in \mathbb{R}^m$, w_k and v_k the process and measurement noises, respectively. The non-linear function f correlates the state at time k with

the state at the current time $k+1$, and it is function of both the input function d_k and the process noise w_k . On the other side, the non-linear function h correlates the state $x_k$with the measurements y_k. It is assumed that noises have Gaussian probability distributions (white, with zero mean) uncorrelated with each other,

$$p(w) \sim N(0, Q) \tag{3.55}$$

$$p(v) \sim N(0, R) \tag{3.56}$$

- the parameter estimation

The parameter estimation consists in defining the non-linear map $G(\cdot)$ between inputs x_k and outputs y_k,

$$y_k = G(x_k, n_k) \tag{3.57}$$

The non-linear map is defined and parameterized by the vector n_k. It is also possible to update the parameters through a new state space representation,

$$n_{k+1} = n_k + r_k \tag{3.58}$$

The minimization function is defined as the difference between the real output and the one generated by the non-linear map,

$$e_k = d_k - G(x_k, n) \tag{3.59}$$

and the aim is to find a set of parameters that minimize a given error function.

- the dual estimation

The discrete state space non-linear system,

$$\begin{aligned} x_{k+1} &= f(x_k, d_k, w_k, n) \\ y_k &= h(x_k, v_k, n) \end{aligned} \tag{3.60}$$

where both states and parameters are unknown and so jointly estimated starting from the measured outputs y_k.

3.4.1 The process to be estimated

We can approximate both state vector and measurement vector by considering the noise to be zero. Then,

$$\hat{x}_{k+1} = f(\hat{x}_k, d_k, 0) \tag{3.61}$$

$$\hat{y}_k = h(\hat{x}_k, 0) \tag{3.62}$$

where $\hat{x}_k$ is the state estimation a posteriori. The traditional Kalman filter recursively propagates the first two moments of the probability distribution of the system state. However, if the dynamic system and the observation equations are non-linear, the value of statistical variables can be calculated only if the probability distribution of $\hat{x}_{k+1}$ is known. Conventionally for the linear case, it is assumed that the distribution of the state $\hat{x}_{k+1}$ is Gaussian, so that the statistical distribution is fully parameterized from the mean and the covariance. However, in the non-linear case, the distribution does not have a general shape and generally is no longer normal type.

3.4.2 The Extended Kalman Filter

One of the most known technique for performing the recursive estimation of non-linear systems is the Extended Kalman Filter (EKF), which extends the traditional Kalman filter to non-linear systems. In the EKF method, the state variable are approximated by Gaussian Random Variables (GRV) which propagate through the first order linearization (around a point) of the system equations. As in the case of the discrete Kalman filter, we obtain the estimates of both the state and covariance from time update equations at the current time k, starting from the previous step $k-1$. Then the measurement update equations correct the state and covariance estimate through the measurement y_k. Note that there is no theoretical guarantee that the estimator is the optimal one and that it is correct, since it provides only an approximation to optimal non-linear estimation. Its behavior is as good as the lower the initial error estimate is. Moreover, unlike the conventional Kalman filter, the gain and covariance matrices must be calculated at each step as a function of

the observations, together with the Jacobian of the matrices A_k and H_k, therefore, the implementation of EKF turns out to be more costly from a computational point of view.

3.4.3 The Unscented Transformation

The Unscented Kalman Filter (UKF) is a derivative-free version of the non-linear filter used as an alternative to the EKF. It was first proposed in (Julier and Uhlmann, 1996, 2004a) and further developed by van der Merve et al. (2000); van der Merve and Wan (2001a,b); van der Merve (2004); Wan et al. (2000); Wan and van der Merve (2001). by The basic component of the UKF is the Unscented Transformation (UT) that is base on a deterministic sampling approach. The state variables are approximated by a Gaussian probability distributions too and the distribution is represented using a set of points appropriately weighted. Indeed, these sampling points, propagated through the true non-linear model of the system and of the measurements, are able to capture both the a posteriori mean and the covariance of the Gaussian distribution. The nature of the transformation is such that the process and the observations models should not be "remodeled", because it is not necessary to linearize the equations, as is the case of the EKF. Therefore, UKF is computationally slender than the EKF. In details, given the Gaussian random variable χ , the UT gives a Gaussian approximation to the joint density distribution of χ and y (Julier and Uhlmann, 2004b), i. e.

$$\begin{pmatrix} \chi \\ y \end{pmatrix} \sim N\left(\begin{pmatrix} \bar{x} \\ \bar{y} \end{pmatrix}, \begin{pmatrix} P_\chi & P_{\chi y} \\ P_{y\chi} & P_y \end{pmatrix} \right) \tag{3.63}$$

where the random variable y is obtained by the non-linear transformation of χ. χ are the so called sigma points and capture the mean and the covariance of the original distribution. The sigma points are deterministically chosen . The unscented transformation is a method capable of calculating the mean and the covariance of a statistical variable which undergoes a nonlinear transformation. The transformation is based on the intuition that it is easier to approximate (using only some points) a Gaussian distribution with respect to an arbitrary function or non-linear transformation. The approach is shown in figure 3.4. It is necessary to choose a set of points, sigma points, where it is applied the non-linear function in order to ob-

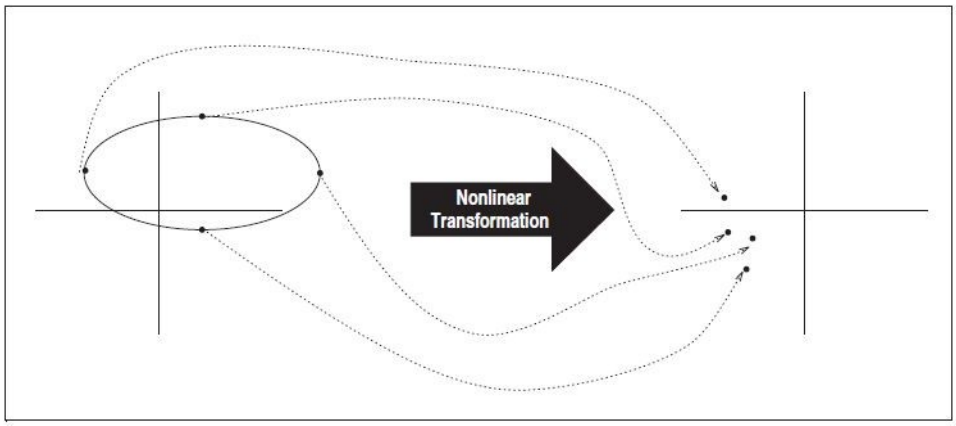

Figure 3.4: The Unscented Transformation

tain a set of transformed points; starting from these points, it is possible to calculate statistical variables. Consider the propagation of the random n-dimensional variable χ_k with mean and covariance $\bar{x}$ and P_χ , respectively, through the non-linear function $y = f(\chi)$. In order to define statistical properties of X, the matrix containing the sigma points is first defined and contains $2n + 1$ vectors named sigma points χ_i. Sigma points and their respective weights W_i are calculated according with the following expressions:

$$\chi_0 = \bar{x} \tag{3.64}$$

$$\chi_i = \bar{x} + (\sqrt{(n+\lambda)P_\chi})_i, \ i = 1, ..., n \tag{3.65}$$

$$\chi_i = \bar{x} - (\sqrt{(n+\lambda)P_\chi})_{i-n}, \ i = n+1, ..., 2n \tag{3.66}$$

$$W_0^m = \frac{\lambda}{\lambda + n} \tag{3.67}$$

$$W_0^c = \frac{\lambda}{\lambda + n} + (1 - \alpha^2 + \beta) \tag{3.68}$$

$$W_i^m = W_i^c = \frac{\lambda}{2(\lambda + n)} \tag{3.69}$$

where

- $\lambda = \alpha^2(n + k) - n$ is a scaling parameter;
- α outlines the spread of sigma points around the mean $\bar{x}$ and it usually is small and positive (i.e. 1^{-3});
- k is a secondary scaling parameter and it can be zero;
- β embeds the previous knowledge of the distribution of x_k and for Gaussian distributions $\beta = 2$;

These sigma vectors are propagated through the non-linear function in order to obtain the set of transformed sigma points,

$$y_i = f(\chi_i),\ i = 1, .., 2n \tag{3.70}$$

The mean and the covariance of y_i are approximated using the weighted mean and covariance of the transformed sigma points (a posteriori):

$$\bar{y} \approx \sum_{i=0}^{2n} W_i^m y_i \tag{3.71}$$

$$P_y \approx \sum_{i=0}^{2n} W_i^c \{y_i - \bar{y}\}\{y_i - \bar{y}\}^T \tag{3.72}$$

Moreover, the cross-covariance between χ and Y can be estimated as

$$P_{\chi y} \approx \sum_{i=0}^{2n} W_i^c \{\chi_i - \bar{x}\}\{\chi_i - \bar{x}\}^T \tag{3.73}$$

The matrix form of the UT is

- $X = [\bar{x}\ ...\ \bar{x}] + \sqrt{c}[0\ \sqrt{P}\ -\sqrt{P}],\ c = \alpha^2(n + k)$
- $Y = f(X)$
- $\bar{y} = Yw_m$,with $w_m = [W_0^m\ ...\ W_{2n}^m]^T$

- $P_y = YWY^T$, with $W = (I - [w_m \ ... \ w_m])\ x\ diag(W_0^c \ ... \ W_{2n}^c)\ x\ (I - [w_m \ ... \ w_m])^T$
- $P_{\chi y} = XWY^T$

The mean and the covariance are calculated by standard operations between matrices and vectors. This means that the algorithm is suitable for every type of process model and the implementation is very rapid because it is not necessary to calculate the Jacobian matrices as in the case of the EKF.

3.4.4 The Unscented Kalman Filter

Consider the discrete non-linear system of equations

$$\begin{aligned} x_{k+1} &= f(x_k, d_k; k) + w_k \\ y_k &= h(x_k, d_k; k) + v_k \end{aligned} \tag{3.74}$$

where x_k is the n-dimensional state, d_k is the input vector, w_k is the q-dimensional Gaussian process noise, y_k is the observations vector and v_k is the Gaussian measurement noise. It's assumed that w_k and v_k have zero mean and covariance,

$$E[w(i)w(j)^T] = \partial_{ij} Q(i) \tag{3.75}$$

$$E[v(i)v(j)^T] = \partial_{ij} R(i) \tag{3.76}$$

$$E[w(i)v(j)^T] = 0, \ \forall i, j \tag{3.77}$$

The UKF prediction and update steps can be presented as follows,

1. Prediction equations
   - Definition of sigma points:

$$X_{k-1} = [\bar{x}_{k-1} \ ... \ \bar{x}_{k-1}] + \sqrt{c}[0 \ \sqrt{P_{\chi,k-1}} \ -\sqrt{P_{\chi,k-1}}] \tag{3.78}$$

   - Propagate sigma points into the process non-linear equation:

$$\hat{X}_k = f(X_{k-1}, d_{k-1}; k-1) \tag{3.79}$$

- Compute the predicted mean:

$$\bar{x}_k = \hat{X}_k w_m \tag{3.80}$$

- Compute the predicted covariance:

$$P^-_{\chi,k} = \hat{X}_k W \hat{X}^T_k + Q_{k-1} \tag{3.81}$$

2. Update equations

- Compute the a priori sigma points:

$$X^-_{k-1} = [\bar{x}^-_{k-1} \ ... \ \bar{x}^-_{k-1}] + \sqrt{c}[0 \ \sqrt{P^-_{\chi,k}} \ - \sqrt{P^-_{\chi,k}}] \tag{3.82}$$

- Propagate sigma points into the non-linear equation of the measurements:

$$Z^-_k = h(X^-_k, d_k; k) \tag{3.83}$$

- Compute the predicted observations:

$$\bar{z}_k = Z^-_k w_m \tag{3.84}$$

- Compute the innovation variance (the measurement noise is considered additive and independent):

$$P_{z,k} = R_k + Z^-_k W[Z^-_k]^T \tag{3.85}$$

- Compute the cross-correlation matrix:

$$P_{\chi z,k} = X^-_k W[Z^-_k]^T \tag{3.86}$$

Finally, the filter gain, the state mean and the covariance read,

$$K_k = P_{\chi z,k} P^{-1}_{z,k} \tag{3.87}$$

$$x_k = x^-_k + K_k(y_k - \bar{z}_k) \tag{3.88}$$

$$P_{\chi,k} = P^-_{\chi,k} - K_k P_{z,k} K^T_k \tag{3.89}$$

CHAPTER 4

THE NOMI FOOTBRIDGE

4.1 Introduction

The Nomi-Calliano footbridge was funded by the Autonomous Province of Trento and was executed by the T&D Associated Engineers of Trento with the aim of connecting the two banks of the Adige River giving continuity to the cycling road. In particular, the design and the finite element model of the bridge are first presented together with a special attention to the vibrational phenomena related to pedestrian and wind action. Vibrational phenomena are already known to researchers and a wide literature about control device can be found. Indeed, a brief description of control in civil structures is reported focusing the attention on the concept of passive, active and semi-active control. Some bibliographic examples of structures endowed with passive, active and semi-active devices complete the overview on the structural control. Then, relevant issues inherent to the Nomi-Calliano footbridge are presented and according to the Setra' technical guide, the dynamic analysis methodology is described. The guide is designed to both give information about actions exerted by pedestrians and that may result in vibrational phenomena and to guide the designer of a new footbridge in the analysis of the dynamic effects induced by pedestrian. In general, these phenomena do not have effects at the ultimate state limit, although the user may feel some discomfort and the serviceability state limit may jeopardize. Consequently the analysis relative to this specific bridge is addressed in order to prevent unwanted vibrational behavior induced by pedestrian and wind. Analysis showed that the footbridge without additional damping devices suffers from the exceeding of some acceleration limits so the design of

a damping system composed by 4 TMDs is performed with the support of the experimental modal analysis. The modal analysis has the aims of identify the modal dynamic characteristics of the structure and consequently tune the damper parameters. Further analysis showed that the optimal solution for the specific footbridge was the insertion of 3 passive and one semi-active TMD. At this purpose, a more detailed focus on the Tuned Mass Damper and on its operating principles and relevant design parameters is reported. Finally, the structure is endowed with a permanent monitoring system integrated with the structure with the aim of checking along time the dynamic behavior related to pedestrian and wind action.

4.2 Control of structures

Structural control is related with the improvement of the dynamic behavior of a structure through the use of specific devices. Some structural typologies, such as concrete-steel composite floors, cable-stayed bridges or pedestrian footbridges, are characterized by high slenderness or low distributed mass, since, in general, the trend is toward taller, longer and more flexible structures. This increased flexibility may compromise the serviceability state since the excessive amplitude of external loads induced vibrations unsettles the users comfort. The structural control is an alternative to the modal properties modification (obtained through the alteration of the structural mass and/or stiffness) and encouraged by economic or aesthetic requirements. Suspended bridges affected by the dynamic action of the wind load and characterized by considerable span and high slenderness is a common and descriptive example of the issue related to the control of vibrations (Diana et al., 2006; Cigada et al., 2002). Also footbridges are affected by the dynamic interaction with the pedestrian and cycling load if the input periods of vibration are comparable with those of the structure (Occhiuzzi et al., 2002, 2008). The dynamic characteristics of the structure are usually modified with additional devices that increase damping or stiffness. This interaction between the generic damping device and the structure can be passive, active or semi-active (Symans and Constantinou, 1999; Spencer and Nagarajaiah, 2003). Passive systems usually modify the damping of the primary structure and are fully operative without any external sources of energy and with no necessity of a feedback control system. A second option is to increase the stiffness of the structure out of the resonant range. On the contrary,

active devices need of both one external source of energy and one control system specifically designed. A control feedback loop and sensors arranged over all the structure lead the active device that can be for example composed by pneumatic or hydraulic actuators and governed by a fluid-mechanical control system. The active control is expensive from both the points of view of money and design. Finally, semi-active systems permit a change in the mechanical characteristic of the device on-line at the cost of a limited dissipation of energy. Then the device, after the induced modification, acts like a passive object.

4.2.1 Passive control

Passive Control Systems do not require an external power of source and the energy in the controlled system can not increase. Passive devices need neither control algorithm nor acquisition of data from sensors. Passive devices are re-

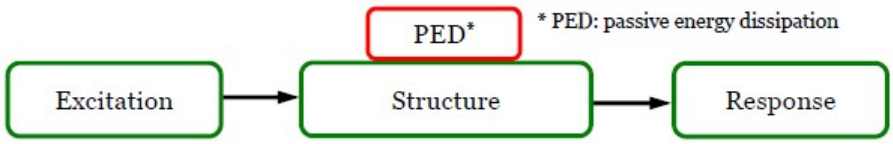

Figure 4.1: working layout of the passive device.

liable since they are liable to blackouts, relatively inexpensive, inherently stable, they consumes no external energy and they work even during a major earthquake. Passive controllers are based on the dissipation or the transfer of kinetic energy. Friction dampers, metallic yield dampers, viscoelastic dampers and viscous fluid dampers dissipate the excess of energy in the system while Tuned Mass Dampers (TMD) and Tuned Liquid Dampers (TLD) just transfer energy from the main system to a secondary one (Casciati et al., 2006). Friction devices slip at a predetermined optimum load before yielding occurs in primary structural members under severe loading conditions (Filiatrault et al., 2000). Obviously, compatible materials must be employed to maintain a consistent coefficient of friction over the intended life of device and it is furthermore important to minimize the stick-slip phenomena to avoid introducing high-frequency excitations. Metallic dampers use the inelastic deformation of metallic substances to dissipate energy and they usually are torsional beams, flexural beams and energy dissipators with various shapes. Viscoelastic

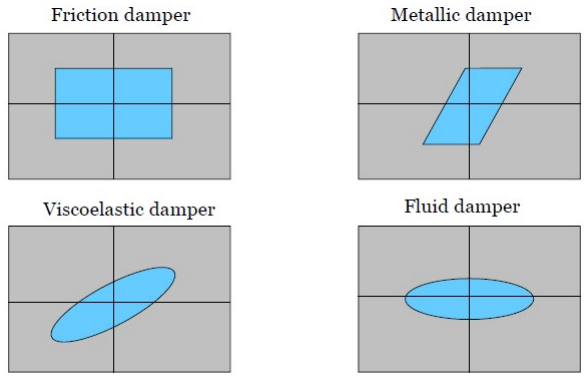

Figure 4.2: behavior of different types of dampers.

and fluid dampers use viscoelastic solid materials and viscous fluid materials, respectively; the first can have elastic plus rate-dependent behavior while the second can have linear or non-linear force-velocity relationship, and both store and dissipate energy for defined deformation levels. Finally, TMDs and TLDs behave as additional oscillators and act as vibration absorbers.

4.2.1.1 Millennium bridge

The suspension bridge opened in June 2000 has cables low positioned respect the level of the deck and is shown in figure 4.3. Detailed information about the footbridge design can be found in Dallard et al. (2001a,b). Despite the initial estimation of 80000/100000 people crossing the bridge during the first opening day, just a maximum of 2000 people (density of 1.3/1.5 people per square meter) were sufficient to activate unexpected excessive lateral vibrations. The oscillations were at frequency of around 0.8 Hz along the south span (first south lateral mode), 0.5 Hz and 1.0 Hz along the central span (first and second lateral modes, respectively). Vibration did not occur continuously and no vertical excessive vibrations were recorded. Pedestrian interacted with the bridge since as the amplitude of the bridge motion increased, the lateral force of the individual person increased too generating a coupling self-exciting effect. This effect was caused by the fact that this type of forces were applied at the resonant frequency and with a phase favorable for the motion of the bridge in such an evident way that the bridge was temporary closed to the public. The adequate level of damping was then achieved,

Figure 4.3: Millennium Bridge, London.

after a long re-design phase, by placing a ”bracing“ pattern of low friction fluid viscous dampers under the deck and a set of TMD with regard the vertical model of the main span (Dallard et al., 2001b).

4.2.1.2 San Michele all'Adige

The ”San Michele“ footbridge in figure 4.4 is located in San Michele, a little town close to Trento. The footbridge was founded by the Autonomous Province of Trento with the aim of improving the cycling and pedestrian link between San Michele and Grumo. The footbridge is a cable-stayed arch bridge made by steel. Cables have a radial disposition with a step of 2.5 m and the deck is 170 m long and with a net width of 3.20 m. The University of Trento was designate to perform dynamic analysis of sensitivity against both wind and pedestrian load. The result was that the structure was endowed with 3 TMDs tuned on the frequency of 0.67 Hz, 0.72 Hz and 2 Hz, respectively. TMDs tuned on the lower frequencies are horizontal and the one tuned on the higher frequency damps vertical oscillations.

Figure 4.4: San Michele Footbridge.

4.2.1.3 Ponte del Mare

The ”Ponte del Mare“ cable-stayed footbridge is shown in figure 4.5 and is located in Pescara at the mouth of the Pescara river close to the sea, in the center of Italy. The bridge has two curved decks sustained by cables connected to a tilted mast, as illustrated in figure 4.5. The outer deck is for pedestrians, while the inner one is for cyclists; both decks have constant radius, of approximately 80 m and 100 m, and their lengths are 173 m and 148 m, respectively. The two decks are spatial steel trusses connected to two prestressed concrete access ramps. The mast is made of steel filled with concrete and rises between the foot-track and the cycle-track decks, with inclination about 11° with respect to the vertical; two cables anchor the top of the mast to the ground. In order to ensure safety requirements under premature aeroelastic instability owing to wind and to mitigate pedestrian vibration, the bridge was provided with a passive control system designed by the University of Trento. It consists in viscous fluid dampers aimed to provide positive damping, but with limiting changes both in modal frequencies and shapes. The relevant design included 8 devices all endowed with viscous fluid dampers and some

Figure 4.5: Ponte del mare, Pescara.

with one spring positioned in series. In particular, three damper types, A, B and C, with differing parameter values are used and are installed at the locations shown in figure 4.6 a) and b). The dampers characteristic are reported in table 4.1 while dampers of Type A/B and C are illustrated in figure 4.6 c) and d).

Table 4.1: dampers characteristics, Ponte del Mare, Pescara - Italy.

	Damper A	Damper B	Damper C
Type	Elastic-viscous	Elastic-viscous	Viscous
Units	2	2	2+2
Damping constant	128.0 kNs/m	349 kNs/m	794 kNs/m
Spring stiffness	127.6 ($\pm$5%) kNm	127.6 ($\pm$5%) kNm	

4.2.2 Active control

A number of structures integrating active control technologies are in Japan and represent the starting point for this type of innovative smart structures (Nishitani and Inoue, 2001). We talk about active structural control in presence of devices able to both subtract and add energy to the structural system they are working on (Spencer and Nagarajaiah, 2003; Symans and Constantinou, 1999; Nishitani

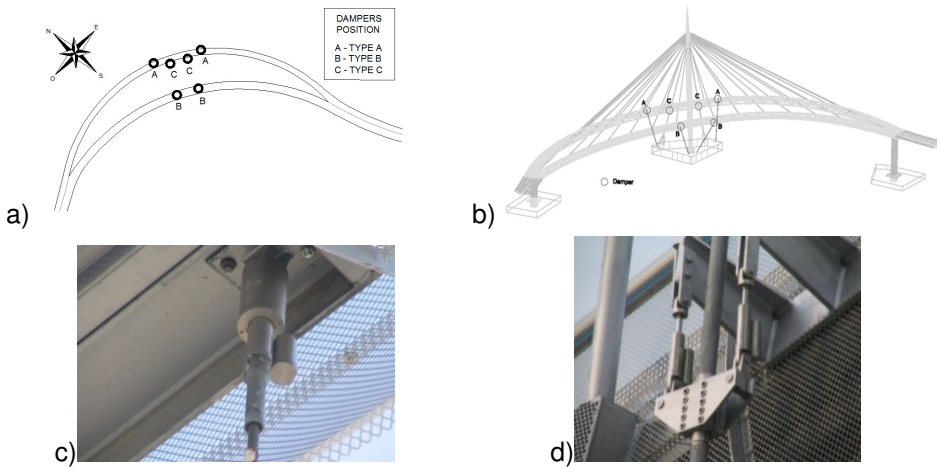

Figure 4.6: a) and b) passive control system positioning; c) damper Type A and B; d) damper Type C.

and Inoue, 2001) by using a certain amount of external energy and through a decision-making process based on data collected in real-time. Typically, electro-hydraulic or electro-mechanic actuators generate the control forces as a function of the structural response and, when possible, also of information about the external excitations. The controller measures the response of the structure and the external excitation and sends the control signal to the actuators thought an algorithm coded in the computer, as shown in figure 4.7. Civil Engineering structures are statically

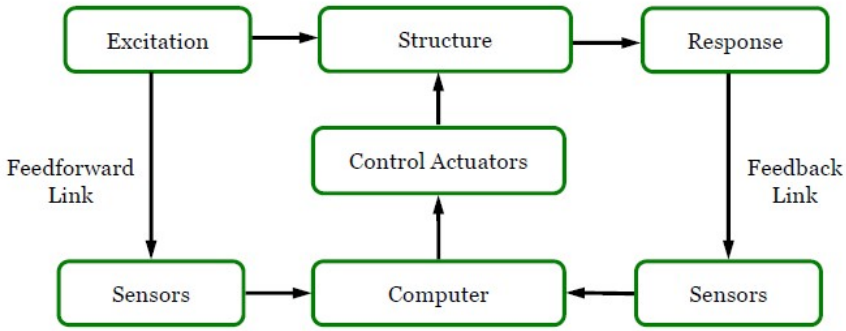

Figure 4.7: working layout of active devices.

stable, but the addition of purely active control forces may cause the destabilization

of the structure. In addition, other disadvantages of active control devices is the initial high cost, the requirement of periodic maintenance of both the actuators and the electric accumulators and the reliance on external sources of power (Spencer and Nagarajaiah, 2003). The most part of the active control systems is designed to suspend its activity during severe seismic events because of the high probability of blackouts. Indeed some devices require tens of kilowatts even if applied to small structures and they can reach many megawatts for huge structures (Soong et al., 1991). The active structural control is not very popular for seismic hazards but is still very useful for reducing wind-induced vibrations in bridges and tall buildings.

4.2.2.1 Kyobashi Building, 1989

The first full-scale application of the active control is the Kyobashi center (Kobori et al., 1991a,b), a 11-storey building erected in 1989 in Tokyo shown in figure 4.8. A system consisting of two Active Mass Dampers (AMDs) with masses of 4 t and 1 t respectively, was installed. They are auxiliary oscillators that influence the dynamic of the structure by adding an inertial force due to the mass, reducing the motion on a frequency range bigger than those of a passive mass damper. The function of the AMDs is to reduce the translational and rotational oscillations of the structure under the excitation induced by strong winds and moderate earthquakes. The total mass of the devices is the 1.1% of the total mass of the building.

4.2.2.2 Osaka ORC 200 Building, 1992

Another example of an ATMD is the 50-storey Osaka Building reported in figure 4.9. The system consists in two masses of 200 tt in total of weight equipped with a control force working along only one directions. The device works in a double fashion: along one direction of oscillation it is just a TMD, along the other one is controlled by a control load. The total mass of the primary structure is 57000 t while the mass ratio is 0.35 %.

4.2.3 Semi-active control

Semi-active control systems overcome the limitations of both passive and active devices. By definition, these systems can not feed power into the structure, but they have the same adaptability that characterizes the active control systems since

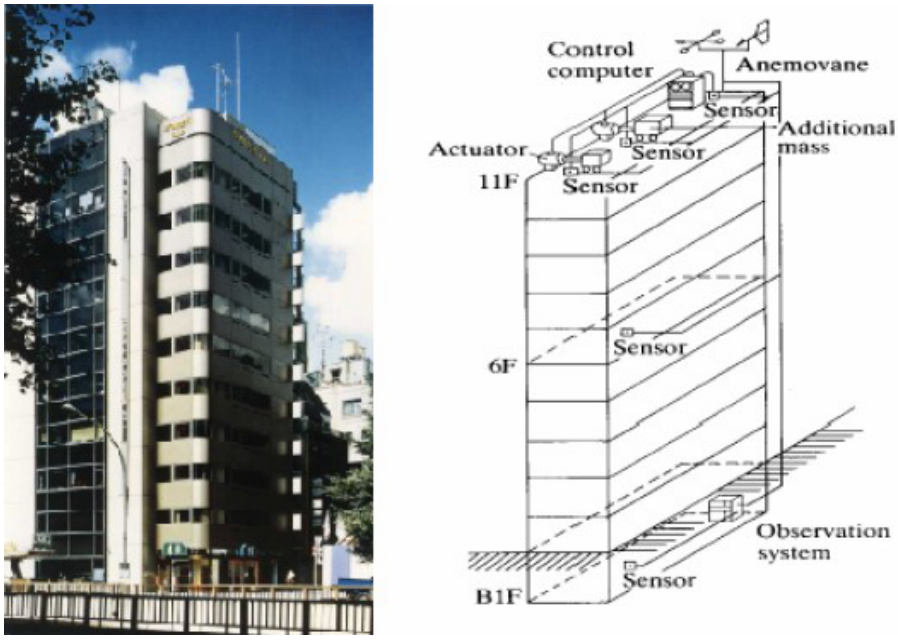

Figure 4.8: Kyobashi Building.

they are typically devices with one or more parameters tunable in real time. As for the active control, the system requires both a monitoring unit for the on-line data acquisition and a control unit for the execution of the control algorithm. Semi-active control systems require electrical power, but employ power of orders of magnitude lower compared to active systems and in certain cases the energy can be supplied by simple batteries. Preliminary studies (Spencer et al., 1997; Symans and Constantinou, 1999; Spencer, 2002) show that if properly implemented, these systems behave significantly better than passive systems, and that have the ability to reach the performance of active systems.

4.2.3.1 The Kajima Shinozuoka Building in Shinozuoka

The Kajima Shinozuoka Building build in Japan and completed on 2000 is the first real application of semi-active control for strong earthquakes. The building is a 5-story steel structure whose floor area is 11.8 m by 24 m and total structural height is 18.6 m (Kurata et al., 1999). The semi-active structural control system is installed in the structure to reduce structural deflections during earthquakes (Kurata et al., 1999; Lynch, 2002; Lynch and Law, 2002). Seth and Jerome (2005) implemented

Figure 4.9: Osaka Building

on the Kajima Shinozuoka Building the semi-active hydraulic dampers in figure 4.10 using both a centralized and decentralized network of wireless sensors and with a Linear Quadratic Control law (LQR).

Figure 4.10: Kajima Shinozuka Building - semi-active hydraulic damper.

4.2.3.2 The Bilbao footbridge

The Bilbao footbridge in figure 4.11 is a stainless steel structure next to the Guggenheim Museum spanning the river Nervin and linking the Deusto University with the district of Abandoibarra. The dynamic behavior is characterized by the possible excitation of higher vibrational modes because of large simultaneous pedestrian loading. The dynamic response of this structure was improved by installing several passive dampers and one semi-active TMD (Millanes and Pascual, 2004).

Figure 4.11: The Bilbao footbridge.

4.2.3.3 Forcheim footbridge

In the framework of EU-founded SPACE program (Semi active and Passive of Control the dynamic behavior of structures subjected to Earthquake, wind and vibration), experimental tests were carried out on the Forcheim footbridge (Figure 4.12) located 200 km from Munich (Occhiuzzi et al., 2008). The bridge was numerically modeled to compare numerical and experimental tests. Occhiuzzi et al. (2002) applied a LQR clipped scheme for a tunable TMD giving a physical description and discussing performances. Then a prototype of the semi active device was developed and the tunable TMD (figure 4.13) was installed with the purpose of

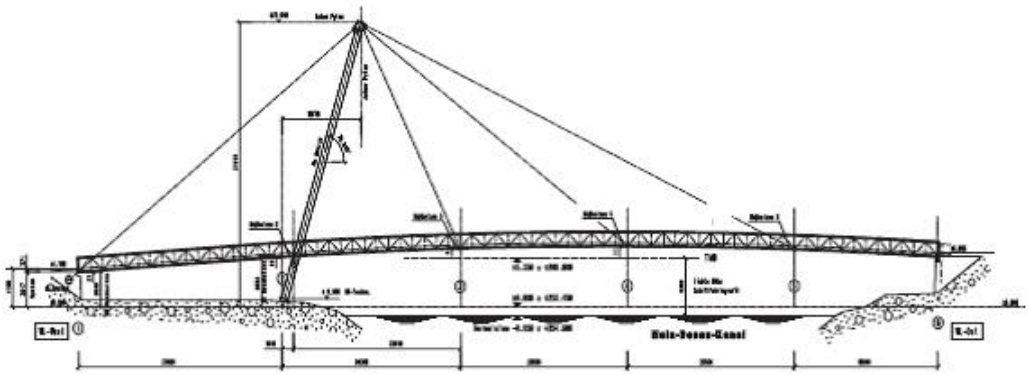

Figure 4.12: Forcheim footbridge, Munich

testing the vibrations reduction.

Figure 4.13: Semi-active MR TMD.

4.3 The Nomi Calliano footbridge design

The Nomi-Calliano footbridge in figure 4.14 was designed by the T&D Associated Engineers of Trento (Raia, 2010) with the aim of connecting the two banks of the Adige River giving continuity to the cycling road. The arch bridge has the deck in the lower part of the structure and is made with painted Corten steel. The structure is asymmetric along the direction orthogonal to the deck axis and in addition the arch is inclined respect to the vertical axis of about 30°, the resulting effect being that the whole deck is an overhanging element supported by cables. The arch has a hollow rectangular section with dimension 1200 mm of depth and high variable between 600 and 1200 mm with the maximum high on the key. The deck

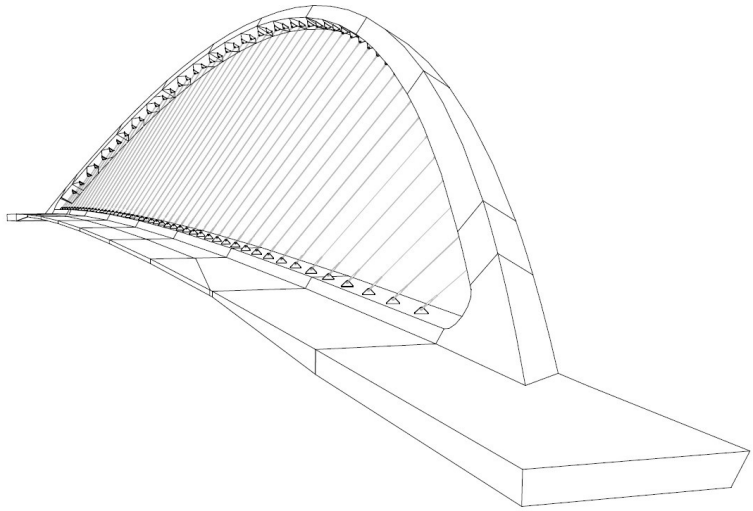

Figure 4.14: the Nomi-Calliano footbridge.

is composed by the upstream trapezoidal-like box section with high torsional resistance, while the downstream section is a cantilever beam composed by welded plates. The section is variable and goes from the maximum high near the shoulders to the minimum value in the center line. The deck is sustained by 50 steel cables made by spiral ropes with nominal diameter of 20 mm, fastened in turn to the arch that is the element transferring all the loads to the foundation system. Furthermore the deck is in-built with the foundation so it assumes also the function of chain in order to zero the pushing action generated by the arch. The footbridge has the net span of 102 m, the vertical deflection of 14.6 cm and the nett and gross width are 3.25 m and 5 m, respectively. Both the deck and the arch are composed by plates made by CORTEN S355 steel and in particular:

- S355J0W for elements with thickness less than 20 mm.
- S355J2W for elements with thickness between 20 mm and 40 mm.
- S355K2W for elements with thickness between 40 mm and 60 mm.

With regard the cables, the steel has characteristic tensile strength $f_{ptk} \geq 1570$ MPa and characteristic strength in correspondence of the 0.2 % of deformation of $f_{p(02)} \geq 1180$ MPa.

4.4 The FEM model

The FEM model is modeled with Ansys and composed of the deck, the arch and the foundation system for a total of 17300 nodes, 19700 elements and 103000 DoFs. The deck is modeled by means of the shell element SHELL181, the BEAM4 element is used to model the arch (with hollow sections) and the LINK180 element is used for the cables in order to take into account the stiffening effect. The foundation deformability is modeled by independent elastic springs (Winkler behavior) using the COMBIN14 element. Not structural masses such as the wood floor and the handrail are handled with the MASS21 element.

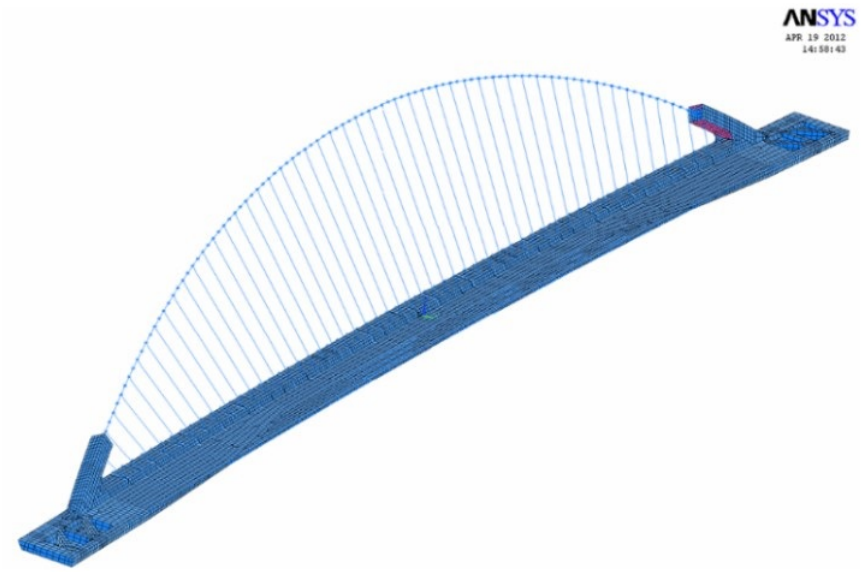

Figure 4.15: the Nomi-Calliano FEM model.

4.5 The dynamic analysis methodology

The technical guide Sètra (Setra', 2006) is based on researches started after the unexpected and unwanted oscillatory phenomena noticed in the Millenium bridge (Dallard et al., 2001b) and Solferino bridge (Blekherman, 2007) with the purpose of giving useful recommendations to the designers. The guide is designed to both give information about actions exerted by pedestrians and that may result in vibrational phenomena and to guide the designer of a new footbridge in the

analysis of the dynamic effects induced by pedestrian. In general, these phenomena do not have adverse effects on structure, although the user may feel some discomfort. The guide does not take into account for marathon, parades and inauguration nor for the wind aerodynamic action. The load induced by the action of the single pedestrian has a specific frequency range that changes in the case of slow/normal/fast walk or jog. From a mathematical point of view, the pedestrian moves in the time along the one axis and x is the pedestrian position in relation to the footbridge center line. The load of a pedestrian moving at constant speed v can therefore be represented as the product of a time component $F(t)$ by a space component $\delta(x - vt)$, δ being the Dirac operator,

$$P(x,t) = F(t)\delta(x(t) - \hat{x}(t)) \tag{4.1}$$

Experimental tests show that this is a periodic load with a fundamental frequency showed in table 4.2, that correspond to the number of steps per second. In particular, the normal walk has mean frequency of 2 Hz and standard deviation of 0.4 Hz. The periodic function $F(t)$ is expressed as a Fourier series using the first harmonic with frequency equal to the base frequency f_m. In detail the load due to one

Table 4.2: frequency range for walking and running (Setra', 2006).

Designation	Specific features	Frequency range for f_m [Hz]
Walking	Continuous contact with the ground	1.6 to 2.4
Running	Discontinuous contact	2 to 3.5

pedestrian write:

- the vertical component

$$F_v(t) = G_0 + 0.4G_0 sin(2\pi f_m t) \tag{4.2}$$

- the transverse horizontal component

$$F_{hT}(t) = 0.05G_0 sin(\pi f_m t) \tag{4.3}$$

- the longitudinal horizontal component

$$F_{hL}(t) = 0.2G_0 sin(2\pi f_m t) \tag{4.4}$$

Table 4.3: density of the crowd.

Class	density d
III	0.5 pedestrian/m^2
II	0.8 pedestrian/m^2
I	1 pedestrian/m^2

The mean value of 700 N may be taken for G_0 that represents the weight of one pedestrian.

4.5.1 Determination of the footbridge class according with Setra' guide

Footbridge class makes possible to determine the level of traffic on a bridge. Footbridges classes are reported in the follow:

- Class IV: seldom used footbridge, built to link sparsely populated areas or to ensure continuity of the pedestrian footpath in motorway or express lane areas.
- Class III: footbridge for standard use, that may occasionally be crossed by large groups of people but that will never be loaded throughout its bearing area.
- Class II: urban footbridge linking up populated areas, subjected to heavy traffic and that may occasionally be loaded throughout its bearing area.
- Class I: urban footbridge linking up high pedestrian density areas (for instance, nearby presence of a rail or underground station) or that is frequently used by dense crowds (demonstrations, tourists, etc.), subjected to very heavy traffic.

The density of the crowd is function of the class as shown in table 4.3. The crowd is uniformly distributed over the total area S of the footbridge

4.5.2 Determination of the resonant risk

The determination of the resonant risk is evaluated according to figures 4.16 a) and b) as a function of the structure natural frequencies. So for pedestrian bridges

belonging to the class I to III, it is necessary to determine the natural frequencies of vibration of the structure. Their determination should be made by taking two different configurations: the first in which pedestrians are considered merely as a forcing (every pedestrian causes a force of 700 N), the second in which pedestrians are intended as structural mass. Once defined the range it is possible to evaluate the acceleration serviceability limits.

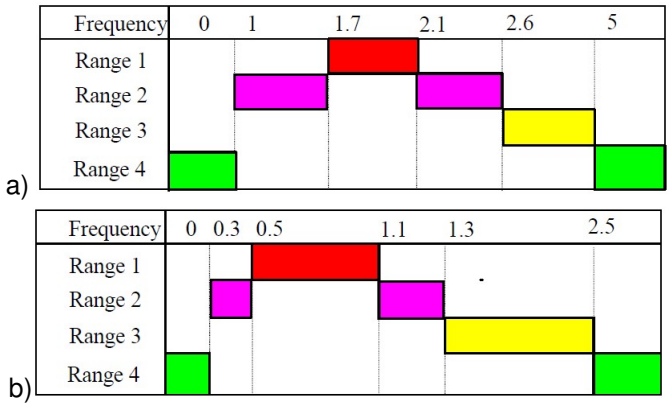

Figure 4.16: frequency range for a) vertical/longitudinal and b) transverse oscillations.

4.5.3 Choose of the comfort levels

The Owner determines one of the comfort level foreseen by the Setra' guide:

- Maximum comfort: accelerations undergone by the structure are practically imperceptible to the users.
- Average comfort: accelerations undergone by the structure are merely perceptible to the users.
- Minimum comfort: under loading configurations that seldom occur, accelerations.

The maximum limit for the vertical and horizontal acceleration are defined according to figure 4.17 for both vertical and horizontal accelerations. On the other hand, the EN 1990-Basis of Structural Design (1990, 2006) recommends the acceleration limits in table 4.4 for the serviceability state. In addition the important limit

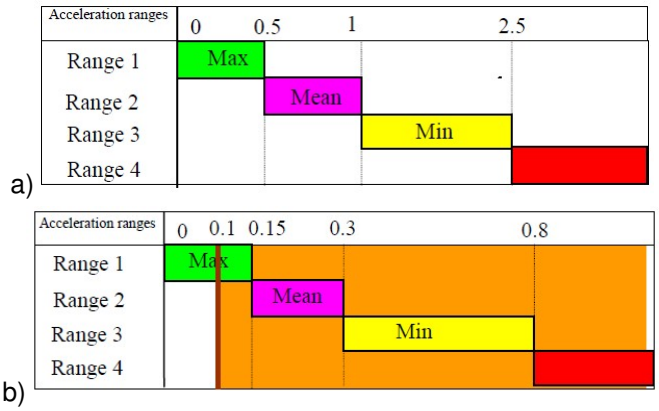

Figure 4.17: a) vertical and b) horizontal limit for accelerations.

Table 4.4: maximum values for acceleration according to EN1990 (1990, 2006).

	Max acceleration $[m/s^2]$
Vertical vibrations	0.7
Horizontal vibrations, normal flux	0.2
Horizontal vibrations, crowd	0.4

of 0.1 m/s^2 for the horizontal acceleration is settled in order to avoid the lock in phenomena.

4.5.4 Load cases

The load case are determined as function of both the frequency risk range and the class of the footbridge. Load cases are three:

- Case 1: sparse and dense crowd
- Case 2: very dense crowd.
- Case 3: effects of the second harmonic of the crowd.

So eqs. 4.2, 4.3 and 4.4 can be written for the whole area S of the bridge and for number of pedestrian equal to N_{eq}.

- the vertical component

$$F_V(t) = S\, N_{eq}\, 0.4\, G_0 cos(2\pi f_m t)\, \psi \tag{4.5}$$

Table 4.5: load cases.

Traffic	Class	Natural frequency range		
		1	2	3
Sparse	III	Case 1	None	None
Dense	II	Case 1	Case 1	Case 3
Very dense	I	Case 2	Case 2	Case 3

- the transverse horizontal component

$$F_{hT}(t) = S\, N_{eq}\, 0.05 G_0 sin(\pi f_m t)\, \psi \tag{4.6}$$

- the longitudinal horizontal component

$$F_{hL}(t) = S\, N_{eq} 0.2 G_0 sin(2\pi f_m t)\ \psi \tag{4.7}$$

where the load due to N_{eq} pedestrians eventually writes,

$$N_{eq} = 10.8\sqrt{N\xi} = 10.8\sqrt{272 * 0.002} = 7.96\,[ped] \tag{4.8}$$

and N is number of pedestrians involved with $N = Sd$ [pedestrian]. The load that is modified by a minus factor ψ which makes allowance for the fact that the risk of resonance becomes less likely since the frequency of the load is far from the natural one. Of course the direction of application of the load is the same as the direction of the mode shape in order to produce the maximum effect.

4.5.5 The soil stiffness

Using ANSYS ® was found that the modal frequencies vary significantly according to the stiffness of the soil (Lorenzi and Bursi, 2011), up to 18% between the natural frequency for the minimum and maximum stiffness of the soil in the mode 3. The mass of pedestrians affects the natural frequencies since the increase of the mass matrix values decrease the natural frequencies, with an average variation of 5% between the two cases. The stiffness matrix takes into account the geometrical non-linearity and is calculated at the end of the static load application, which considers also the stress stiffening effects. Assuming that the soil stiffness

variation is linear according to eq. 4.9,

$$K_i = K_{min} + \frac{i}{10}\left(K_{max} - K_{min}\right) \tag{4.9}$$

The natural frequencies for the first five critical modes are reported in table 4.6. The

Table 4.6: natural frequencies as function of the soil stiffness.

	Frequency [Hz]					
mode	K_0	K_2	K_4	K_6	K_8	K_{10}
1	0.74	0.76	0.76	0.77	0.77	0.77
2	1.21	1.22	1.22	1.22	1.22	1.23
3	1.22	1.34	1.39	1.41	1.42	1.43
4	1.88	1.91	1.92	1.92	1.93	1.93
5	2.17	2.19	2.20	2.20	2.21	2.21

classification of the critical modes is in tables 4.7 and 4.8. There is an inversion

Table 4.7: Main characteristic of the first five modes for K_{min}.

Mode	Frequency [Hz]	Element	Direction	Shape
1	0.74	arch	out of the plane	symmetric
2	1.21	deck	transverse and vertical	symmetric
3	1.22	deck	vertical	antisymmetric
4	1.88	arch	out of the plane	symmetric
5	2.17	deck	vertical	symmetric

of the shape of the second and third modes respectively because of the change of the soil stiffness from the minimum to the maximum stiffness. Figures from 4.18 to 4.22 show the first five mode shapes.

Table 4.8: Main characteristic of the first five modes for K_{max}.

Mode	Frequency [Hz]	Element	Direction	Shape
1	0.77	arch	out of the plane	symmetric
2	1.23	deck	vertical	antisymmetric
3	1.43	deck	transverse and vertical	symmetric
4	1.93	arch	out of the plane	symmetric
5	2.21	deck	vertical	symmetric

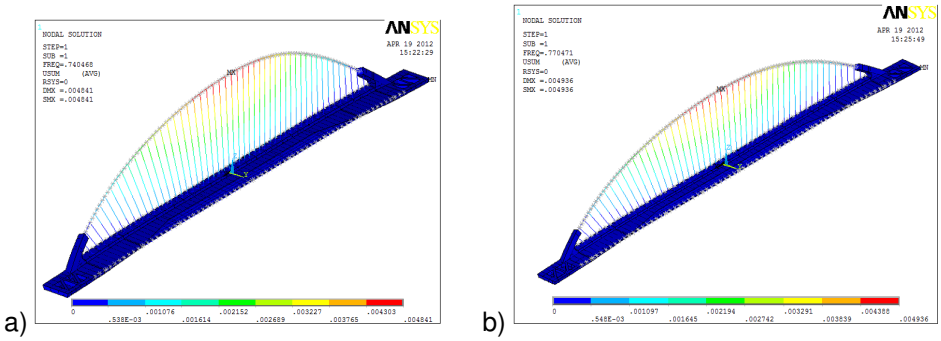

Figure 4.18: 1^{st} natural mode for a) K_{min} and b) K_{max}

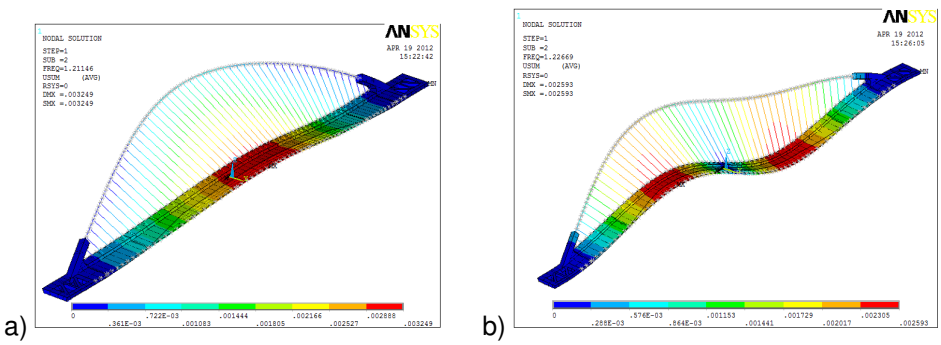

Figure 4.19: 2^{nd} natural mode a) K_{min} and b) K_{max}

a) 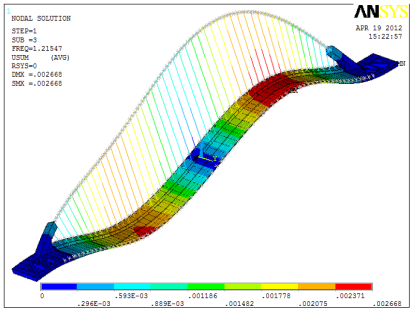

b) 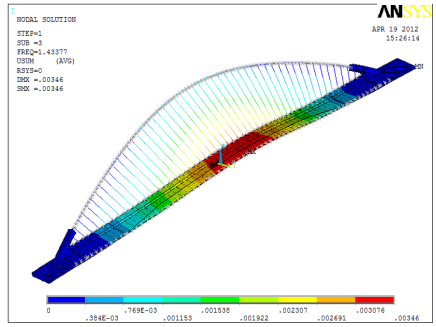

Figure 4.20: 3rd natural mode a)K_{min} and b) K_{max}

a) 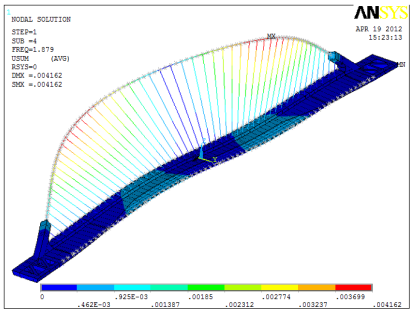

b) 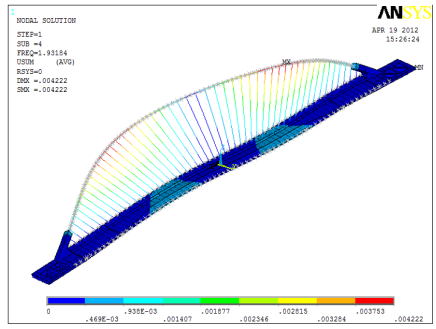

Figure 4.21: 4th natural mode a) K_{min} and b) K_{max}

a) 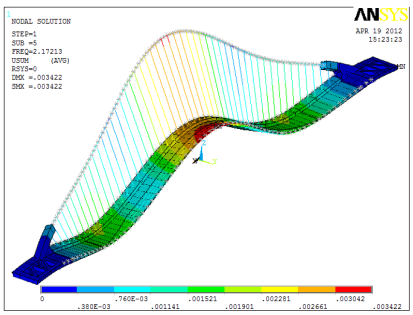

b) 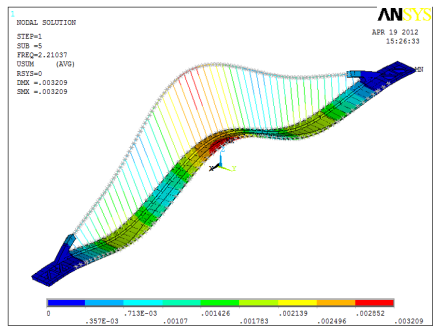

Figure 4.22: 5th natural mode a) K_{min} and b) K_{max}

4.5.6 Design loads

As indicated by the Province, the Nomi-Calliano footbridge belongs to Class II with average comfort. The acceleration limits according to the codes are as follows,

- $A_{v,max}$Setra = 1.0 m/s^2
- $A_{v,max}$EN1990= 0.7 m/s^2
- $A_{T,max}$Setra = 0.3 m/s^2
- $A_{T,max}$Setra = 0.1 m/s^2, because of the lock-in phenomena.

Eventually the limits chosen are 0.7 m/s^2 for vertical accelerations and 0.1 m/s^2 for transverse accelerations. The dynamic response of the structure is evaluated by assigning the dynamic load in resonance with the j^{th} mode. If application point are equally spaced, the action exerted by pedestrian can be described as,

$$F_{V,ij} = sign[\phi_{V,ij}]\frac{Amp_V}{N_{nodi}}\psi_V(f_i),\ i = 1, ..., N_{modi},\ j = 1, ..., N_{nodi} \tag{4.10}$$

$$F_{T,ij} = sign[\phi_{T,ij}]\frac{Amp_T}{N_{nodi}}\psi_T(f_i)\ i = 1, ..., N_{modi},\ j = 1, ..., N_{nodi} \tag{4.11}$$

$$F_{L,ij} = sign[\phi_{L,ij}]\frac{Amp_L}{N_{nodi}}\psi_L(f_i)\ i = 1, ..., N_{modi},\ j = 1, ..., N_{nodi} \tag{4.12}$$

where φ_{ij} is the j^{th} component of the i^{th} mode, N_{modi} is the number of node selected on the deck and f_i is the damped frequency of the i^{th} mode. As anticipated, the amplitudes of the harmonic loads write $Amp_V = N_{eq}0.4G_0 = 2230\,N$, $Amp_T = N_{eq}0.05G_0 = 279\,N$ and $Amp_L = N_{eq}0.2G_0 = 1115\,N$. So let's define the load "with the i^{th} shape" as the load with components having the same sign of the i^{th} mode,

$$F_{V,i} = (F_{V,i\,1}, ..., F_{V,i\,N_{nodi}}) \tag{4.13}$$

$$F_{T,i} = (F_{T,i\,1}, ..., F_{T,i\,N_{nodi}}) \tag{4.14}$$

$$F_{L,i} = (F_{L,i\,1}, ..., F_{L,i\,N_{nodi}}) \tag{4.15}$$

The total load $F_i = F_{V,i} + F_{T,i} + F_{L,i}$ is the amplitude of the i^{th} resonant load. The modal load is of course $P_i = \Phi^T \left(F_{V,i} + F_{T,i} + F_{L,i}\right)$. Remembering the dynamic amplification factor,

$$H(\beta_{ik}) = \sqrt{\left(\left(1 - \beta_{ik}^2\right)^2 + \left(2\xi\beta_{ik}\right)^2\right)} \tag{4.16}$$

it is easy to find the modal excitation at steady state for the i^{th} mode and k^{th} load shape

$$\lambda_{ik} = \frac{1}{\hat{K}_i} H(\beta_{ik}) P_{ik} \tag{4.17}$$

For any k frequency of the load, one has

$$\lambda_k = \left(\frac{1}{\hat{K}_1} H(\beta_{1k}) P_{1k}, ..., \frac{1}{\hat{K}_{N_{modi}}} H(\beta_{N_{modi}k}) P_{N_{modi}k}\right) \tag{4.18}$$

with $\beta_{ik} = \omega_k / \omega_i$ where k is the load frequency and i is the natural frequency of the structure. The steady state displacement, velocity and acceleration field, holds

$$u_k = \Phi \lambda_k \tag{4.19}$$

$$\dot{u}_k = \omega_k u_k \tag{4.20}$$

$$\ddot{u}_k = \omega_k^2 u_k \tag{4.21}$$

In tables 4.9 and 4.10 are summarized results for minimum soil stiffness while in tables 4.11 and 4.12 are summarized result for maximum soil stiffness. In the case of K_{min}, longitudinal acceleration are negligible and vertical accelerations exceed limits for a forcing load in resonance with the 5^{th}mode while transverse accelerations exceed limits for a forcing load in resonance with the 2^{nd} and the 5^{th}mode. For K_{max}, in the same way longitudinal acceleration are negligible but both vertical and transverse accelerations exceed limits for a forcing load in resonance with the $3^{rd}$and the 5^{th}mode. Consequently, in order to maintain the serviceability limit of the footbridge, a damping system composed by 4 TMDs was chosen.

Table 4.9: maximum vertical acceleration for minimum soil stiffness.

Modal load	Direction	Node	a $[m/s^2]$	Coordinates [node, x, y, z]
1	v	18	0.000	{3237, -35.1, 3.3, -0.91}
2	v	41	0.469	{8011, 0.9, 2.75, 0.12}
3	v	27	0.609	{5178, -20.1, 2.75, -0.04}
4	v	53	0.094	{10241, 17.7, 2.75, 0.03}
5	v	41	1.846	{8011, 0.9, 2.75, 0.12}

Table 4.10: maximum transverse acceleration for minimum soil stiffness.

Modal load	Direction	Node	a $[m/s^2]$	Coordinates [node, x, y, z]
1	t	42	0.001	{8018, 0.9, 0.44, 0.12}
2	t	42	0.389	{8018, 0.9, 0.44, 0.12}
3	t	36	0.060	{6760, -8.4, 0.44, 0.1}
4	t	62	0.038	{11816, 29.7, 0.47, -0.23}
5	t	41	0.604	{8011, 0.9, 2.75, 0.12}

4.6 Tuned Mass Damper

TMDs are passive devices used in the field of the structural control but they are common also in the automotive field (Hartog, 1940). The device introduces additional damping to the mode witch is tuned. It is constituted by a secondary mass supported by a spring and a damper and the mass is a percentage of the total mass of the mode to be damped. The mass vibrates with a phase shift respect to the bridge motion. Hartog (1940) showed that the resonance of the external force with the noticeable frequency generates a relative motion between primary and secondary mass sufficient to activate the damper and to dissipate energy. The damper activation has also the effect of enlarging the frequency interval over the TMD is effective. Indeed the resonance frequency is split into other two frequencies close to the initial and with the dynamic amplification factor lower than the original one. The goal of an optimal tuning is to make equal the amplification factor of these two frequencies by choosing the optimal level of damping. These devices need of

Table 4.11: maximum vertical acceleration for maximum soil stiffness.

Modal load	Direction	Node	a $[m/s^2]$	Coordinates [node, x, y, z]
1	v	41	0.000	{8011, 0.9, 2.75, 0.12}
2	v	55	0.606	{10636, 20.7, 2.75, 0.}
3	v	41	1.070	{8011, 0.9, 2.75, 0.12}
4	v	53	0.092	{10241, 17.7, 2.75, 0.03}
5	v	41	1.545	{8011, 0.9, 2.75, 0.12}

Table 4.12: maximum transverse acceleration for maximum soil stiffness.

Modal load	Direction	Node	a $[m/s^2]$	Coordinates [node, x, y, z]
1	t	42	0.000	{8018, 0.9, 0.44, 0.12}
2	t	58	0.021	{11007, 23.4, 0.44, -0.1}
3	t	42	0.797	{8018, 0.9, 0.44, 0.12}
4	t	64	0.013	{12121, 32.1, 0.53, -0.29}
5	t	41	0.601	{8011, 0.9, 2.75, 0.12}

an accurate design and suffer of mistuning since the dynamic characteristic of the structure may variate in time. Let's consider a SDoF structure without tuned mass damper and with structural mass m_s, structural stiffness k_s and damping c_s. The load acting on the primary structure $F_s(t)$ is harmonic and $u(t)$ is the displacement. The equation of motion of a SDoF subjected to an harmonic excitation reads,

$$m_s\ddot{u}(t) + c_s\dot{u}(t) + k_s u(t) = F_s(t) = p_0 sin(\omega t) \tag{4.22}$$

The particular solution is

$$x_p(t) = \bar{X}e^{i\omega t} \tag{4.23}$$

and substituting into the equation of motion, one obtains

$$x_p(t) = \frac{p_0}{k}\frac{1}{\sqrt{[1-[(\frac{\omega}{\omega_s})^2]^2 + [2\xi_s(\frac{\omega}{\omega_s})]^2}} = \frac{p_0}{k}\frac{1}{A} \tag{4.24}$$

where A is the Dynamic Amplification Factor (DAM)

$$A = \sqrt{(1-\beta^2)^2 + (2\xi_s\beta)^2} \tag{4.25}$$

with $\beta = \omega/\omega_s$. The angle phase is

$$\tan\vartheta = \frac{2\xi_s\beta}{1-\beta^2},\ 0^\circ < \vartheta < 180^\circ \tag{4.26}$$

At steady state, the dynamic behavior is equal to the corresponding static one multiplied by the amplification factor. The necessity to increase the dissipative capacity in order to reduce the peak at $\beta = 1$ is evident for structures with low damping ratio. By adding a second mass to the SDoF we obtain the 2DoF system, as shown in figure 4.23, whose dynamic behavior is governed by the following system of second order differential equations,

$$\begin{bmatrix} m_s & 0 \\ 0 & m_d \end{bmatrix} \begin{pmatrix} \ddot{u}_s \\ \ddot{u}_d \end{pmatrix} + \begin{bmatrix} c_s + c_d & -c_d \\ -c_d & c_d \end{bmatrix} \begin{pmatrix} \dot{u}_s \\ \dot{u}_d \end{pmatrix} + \tag{4.27}$$

$$+ \begin{bmatrix} k_s + k_d & -k_d \\ -k_d & k_d \end{bmatrix} \begin{pmatrix} u_s \\ u_d \end{pmatrix} = \begin{pmatrix} F_s(t) \\ 0 \end{pmatrix}$$

Hartog (1940) found the analytical steady state solution for sinusoidal load and

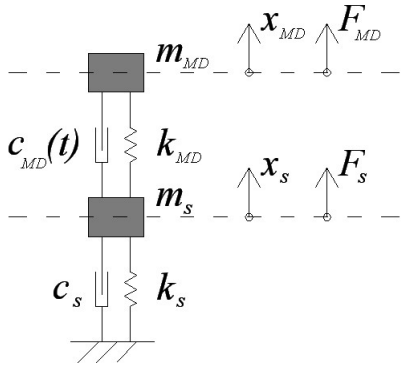

Figure 4.23: single oscillator endowed with the mass damper

zero structural damping ratio. So the dynamic amplification factor proves to be

$$A = \sqrt{\frac{(\alpha^2-\beta^2)^2 + (2\xi_s\alpha\beta)^2}{[(\alpha^2-\beta^2)(1-\beta^2) - \alpha^2\beta^2\mu]^2 + (2\xi_s\alpha\beta)^2(1-\beta^2-\beta^2\mu)^2}} \tag{4.28}$$

where $\alpha = \omega_d/\omega_s$ and the frequency of the damper is

$$\omega_d = \sqrt{\frac{k_d}{m_d}} \tag{4.29}$$

The damping ratio of the mass damper is

$$\xi_d = \frac{c_d}{c_{d,crit}} = \frac{c_d}{2m_d\omega_d} \tag{4.30}$$

and the TMD mass ratio is

$$\mu = \frac{m_d}{m_s} \tag{4.31}$$

where a convenient value should be $\mu > 0.01$. The insertion of the TMD involves many consequences since the number of DoF increases with the resulting increase of the number of natural modes of the structure. The two new frequencies are respectively smaller and bigger than the initial one and the damper mass oscillates with a circular frequency of ω_d. Of course, the TMD requires a proper tuning in order to minimize the maximum dynamic response. The initial peak is split into other two peaks of equal amplitude and focused on the frequencies of the new 2DoF. The optimal constant parameters for the optimal tuning of the MD are the optimal elastic stiffness α_{opt} and the optimal damping ratio ξ_{opt} and they were found by Hartog (1940)

$$\alpha_{opt} = \frac{1}{1+\mu} \lesssim 1 \tag{4.32}$$

$$\xi_{opt} = \sqrt{\frac{3\mu}{8(1+\mu)^3}} \tag{4.33}$$

The maximum amplitude of the two new peaks is

$$A_{max,opt} = \sqrt{1+\frac{2}{\mu}} \tag{4.34}$$

and it is a function of the mass ratio of the damper since it decreases with the increase of the mass of the damper. Of course, the coefficient μ influences the efficiency of the TMD and all the design parameters. In figure 4.24 α, ξ_d, c_d and k_d are the design parameters of the mass damper and they are plotted as function of the mass ratio of the system. In general α and k_d decrease when μ increases while ξ_d and c_d increase with μ. The TMD is sensitive to the mistuning due basically to the variations in the structure stiffness and in the structural mass along the time

(the first one can be caused by settlement of the constraints and the second by the presence of operating loads not expected or forecast in the design phase).

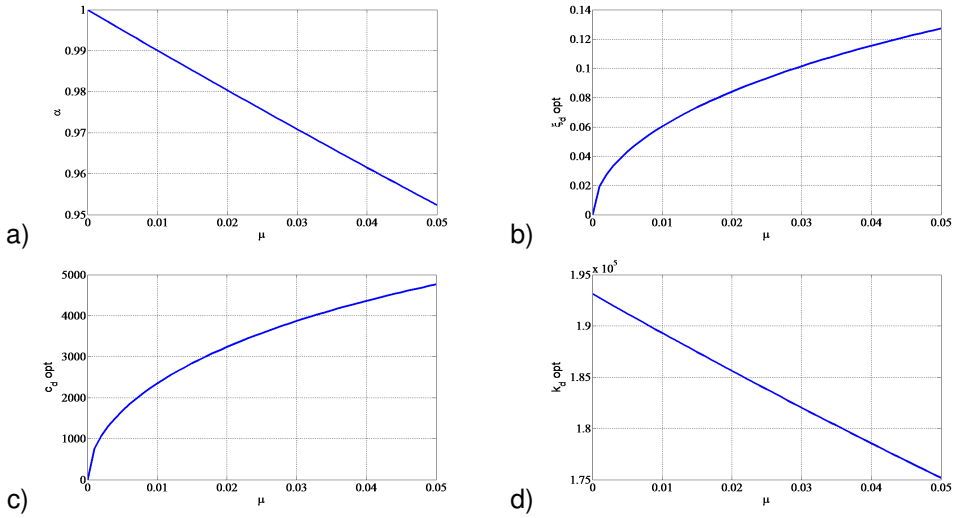

Figure 4.24: behavior of the optimal design parameters for the TMD as function of the mass ratio.

Figure 4.25 a) shows the behavior of the dynamic amplification factor of an optimal TMD subject to changes of the mass ratio ($1\% < \mu < 5\%$) and of the optimal stiffness parameter (with percentage difference of the 1%, 2%, 5% and 10% of α_{opt}). In particular figure 4.25 b) shows that the efficiency of the optimal damper can dramatically change as a function of the secondary mass, till the effect of the second mass totally vanishes. The effect of the damper damping ratio is also essential. When $\xi_d = 0$, we have just an oscillating mass over the primary structure. Indeed, in such a case, the amplification factor shows that the dynamic amplification is quite evident over both the two modal frequencies of the 2DoF, as shown in figure 4.26 a). When $\xi_d \neq 0$, the resonant peaks does not go to infinite and a better dynamic behavior is attained but still not the optimal one. It is not suitable to adopt damping ratio too high since for $\xi_d \to \infty$, the damper mass in no more an oscillating object but results to be rigidly fixed to the primary structure and the whole system become again a single DoF and the effect of the damper is just an increase of mass with a tiny variation of the modal frequency and no

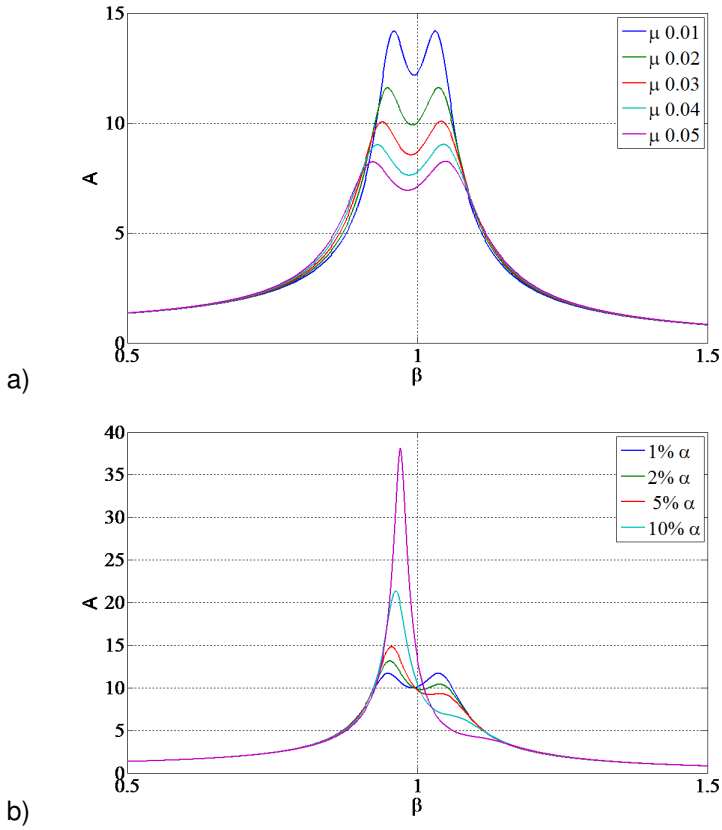

Figure 4.25: dynamic amplification factors as function of a)the mass ratio and of b)the optimal damper stiffness.

additional damping. The result is that when the dashpot has a huge damping, the coupling effect between structure and damper is useless. Figure 4.26 b) shows the dynamic factor for a ratio β equal to 1 and for different values of the damper damping ratio. The response amplitude of the structure is zero in correspondence of $\beta = \alpha$, that is when the frequency of the load is the same of the frequency of the oscillating mass; in this case, the additional mass oscillates in opposition of phase respect to the load. In figure 4.27 the dynamic amplification factors for tuned and mistuned TMD are shown (5% error) for different mass ratio. The possibility of mistuning is greater if the mass ratio is small, that happens for TMDs of small dimensions. It is important to remember that the Den Hartog solution considers zero structural damping; for $\xi_S \neq 0$, the results are just an approximation of the

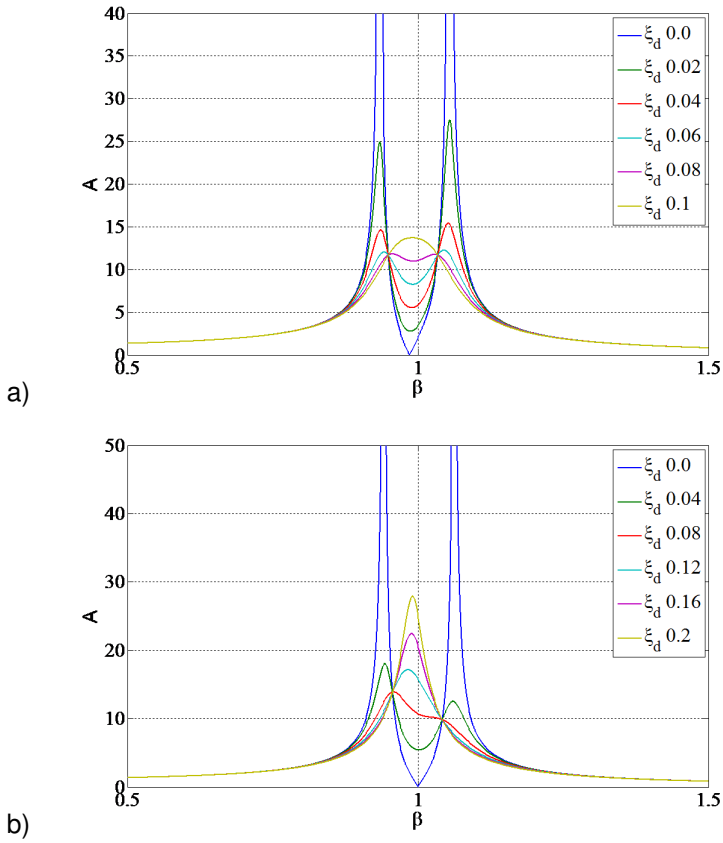

Figure 4.26: dynamic amplification factors as function of the damping ratio of the damper for a) $\beta \neq 1$ and b)$\beta = 1$

optimal one. However, if the structural damping is $<$ 1% the solution is still a good approximation.

4.6.1 The influence of the soil stiffness on the TMD design

The stiffness of the soil and its interaction with the footbridge influences the natural frequencies and mode shapes. In this subsection the influence of the soil stiffness on the TMD design is considered. In order to design the TMD for the i^{th} mode, it is necessary to do the conceptual and mathematical step from the i^{th} mode shape to the corresponding SDoF in principal coordinates. Given the well

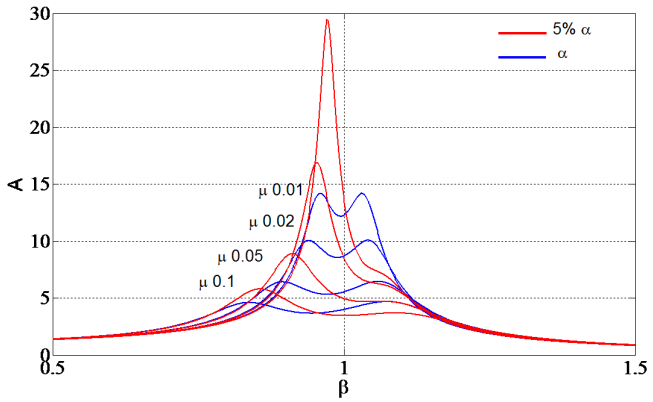

Figure 4.27: effects of the mistuning.

known equation of motion,

$$M\ddot{u}(t) + C\dot{u}(t) + Ku(t) = F(t) \tag{4.35}$$

the modal matrix is defined as

$$\Phi = \left(\phi_1, ..., \phi_m\right) \tag{4.36}$$

where ϕ_i is the i^{th} mode shape and N the number of degree of freedom of the discrete system. The geometric field is a linear combination of all the modes,

$$u(t) = \Phi\lambda(t) \tag{4.37}$$

where λ is the vector of the modal amplitudes. Eq. 4.35 became,

$$\Phi^T M\Phi\ddot{\lambda}(t) + \Phi^T C\Phi\dot{\lambda}(t) + \Phi^T K\Phi\lambda(t) = \Phi^T F(t) \tag{4.38}$$

and

$$\hat{M}\ddot{\lambda}(t) + \hat{C}\dot{\lambda}(t) + \hat{K}\lambda(t) = P(t) \tag{4.39}$$

If the damping is proportional and the matrices $\hat{M}$, $\hat{C}$ and $\hat{K}$ are diagonal, it is possible to decouple the equations of motion in N independent equations,

$$\hat{m}_i\ddot{\lambda}_i(t) + \hat{c}_i\dot{\lambda}_i(t) + \hat{k}_i\lambda_i(t) = P_i(t) \tag{4.40}$$

From 4.37, the shape of the node called s is,

$$u_s(t) = \Phi[row\ s]\lambda(t) = \sum_i \lambda_i\varphi_{is} \tag{4.41}$$

Consequently, when the displacement component of the i^{th} mode is much higher than the components due to other modes (that happens when the load is resonant with one natural frequency of the structure and the frequencies are well spaced), it is possible to round off the displacement of the node s as follows,

$$u_s(t) \cong u_{s,i}(t) = \lambda_i \varphi_{is} \tag{4.42}$$

Substituting eq. 4.42 into eq. 4.40 and pre-multiplying for φ_{is}^{-1},

$$\frac{\hat{m}_i}{\varphi_{is}^2}\ddot{u}_s + \frac{\hat{c}_i}{\varphi_{is}^2}\dot{u}_s + \frac{\hat{k}_i}{\varphi_{is}^2}u_s = \frac{P_i(t)}{\varphi_{is}} \tag{4.43}$$

and replacing with m_s, c_s and k_s, respectively the mass, damping and stiffness of the SDoF oscillator corresponding to a structure deforming exactly like the i^{th} mode,

$$m_s = \frac{\hat{m}_i}{\varphi_{is}^2},\ c_s = \frac{\hat{c}_i}{\varphi_{is}^2},\ k_s = \frac{\hat{k}_i}{\varphi_{is}^2},$$

where for $\varphi_{is} \to 0$ then $m_s,\ c_s,\ k_s \to \infty$. One obtains

$$m_s\ddot{u}_s + k_s\dot{u}_s + k_s u_s = \frac{P_i(t)}{\varphi_{is}} \tag{4.44}$$

Let now be $F_0(t)$ the dynamic load on the structure without TMD. The i^{th} modal component of this load is $P_{i0}(t)$,

$$P_{i0}(t) = \phi_i F_0(t) \tag{4.45}$$

Meanwhile in the damper installed on the node s, the elastic and damping forces in the TMD interact with the structure

$$F_s(t) = F_E(t) + F_D(t) \tag{4.46}$$

with

$$F_E(t) = k_d\left(u_s(t) - u_d(t)\right) \tag{4.47}$$

$$F_D(t) = c_d\left(\dot{u}_s(t) - \dot{u}_d(t)\right) \tag{4.48}$$

Similarly, the i^{th} modal component of $F_s(t)$ writes,

$$P_{is}(t) = \varphi_{is} F_s(t) \tag{4.49}$$

So the dynamic load and the forces inside the TMD are summed up together

$$P(t) = P_{i0}(t) + P_{is}(t) = \phi_i F_0(t) + \varphi_{is} F_s(t) \tag{4.50}$$

Substituting eq. 4.50 into eq. 4.44, one has

$$m_s \ddot{u}_s + k_s \dot{u}_s + k_s u_s = \frac{P_i(t)}{\varphi_{is}} = \frac{P_{i0}(t)}{\varphi_{is}} + F_s(t) \tag{4.51}$$

and taking into account also eqs. 4.47 and 4.48, holds

$$\begin{bmatrix} m_s & 0 \\ 0 & m_d \end{bmatrix} \begin{pmatrix} \ddot{u}_s \\ \ddot{u}_d \end{pmatrix} + \begin{bmatrix} c_s + c_d & -c_d \\ -c_d & c_d \end{bmatrix} \begin{pmatrix} \dot{u}_s \\ \dot{u}_d \end{pmatrix} + \tag{4.52}$$

$$+ \begin{bmatrix} k_s + k_d & -k_d \\ -k_d & k_d \end{bmatrix} \begin{pmatrix} u_s \\ u_d \end{pmatrix} = \begin{pmatrix} \frac{P_{i0}(t)}{\varphi_{is}} \\ 0 \end{pmatrix}$$

Since the TMD mass ratio has the following formulation,

$$\mu = \frac{m_d}{m_s} = \frac{m_d \phi_{is}^2}{\hat{M}_i} \tag{4.53}$$

it results evident that in order to maximize μ for the i^{th} mode, it is necessary to put the TMD in correspondence of the maximum component of the i^{th} mode shape. In tables 4.28 and 4.29 are shown the optimal values for the elastic spring and for the dash-pot of the TMD as a function of the soil stiffness.

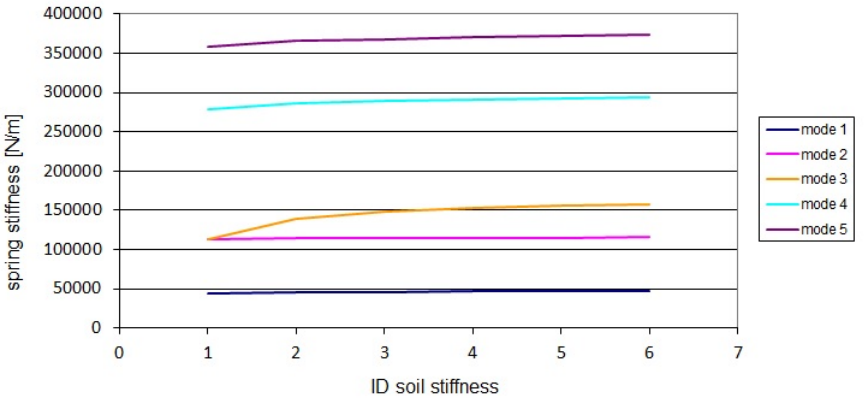

Figure 4.28: optimal stiffness of the TMD spring.

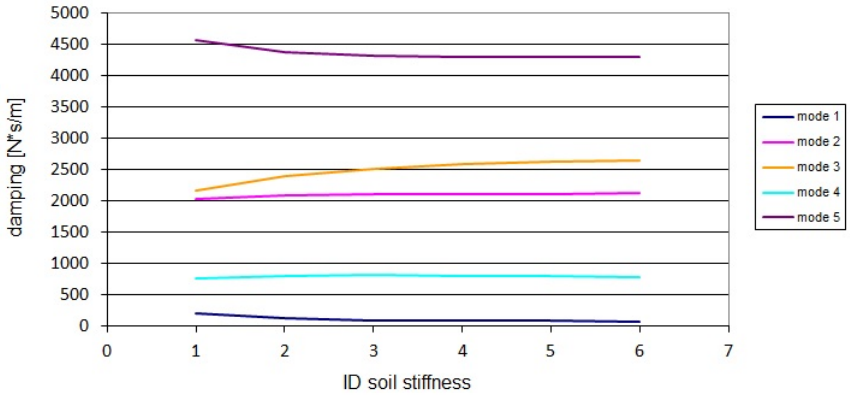

Figure 4.29: optimal damping of the TMD dashpot.

4.7 Experimental modal analysis and model updating

On the 12th of July 2012, an experimental campaign was carried out on the Nomi-Calliano footbridge with the aims to identify the modal dynamic characteristics of the structure and consequently tune the damper parameters. In detail, during the tests the structure was dynamically excited and the response measured by means of accelerometer acquisitions. Tests comprised environmental excitation signals, free decay signals (by releasing a mass hanging from the bridge) and hummer test signals. The identification tests were carried out on the structure not yet complete, in particular, can be highlighted the lack of the following elements:

- the TMDs;
- the wood planking level;
- the handrail.

4.7.1 Set-up

The set-up was composed by 8 fixed and 9 temporary accelerometers and is visible in figure 4.30. The effectiveness of the set-up was measured in terms of MAC matrix on the modal shapes projected on the set-up accelerometer positions and it appeared well decoupled till about 10 Hz. The 2600 kg masses were used to simulate the presence of the TMD masses.

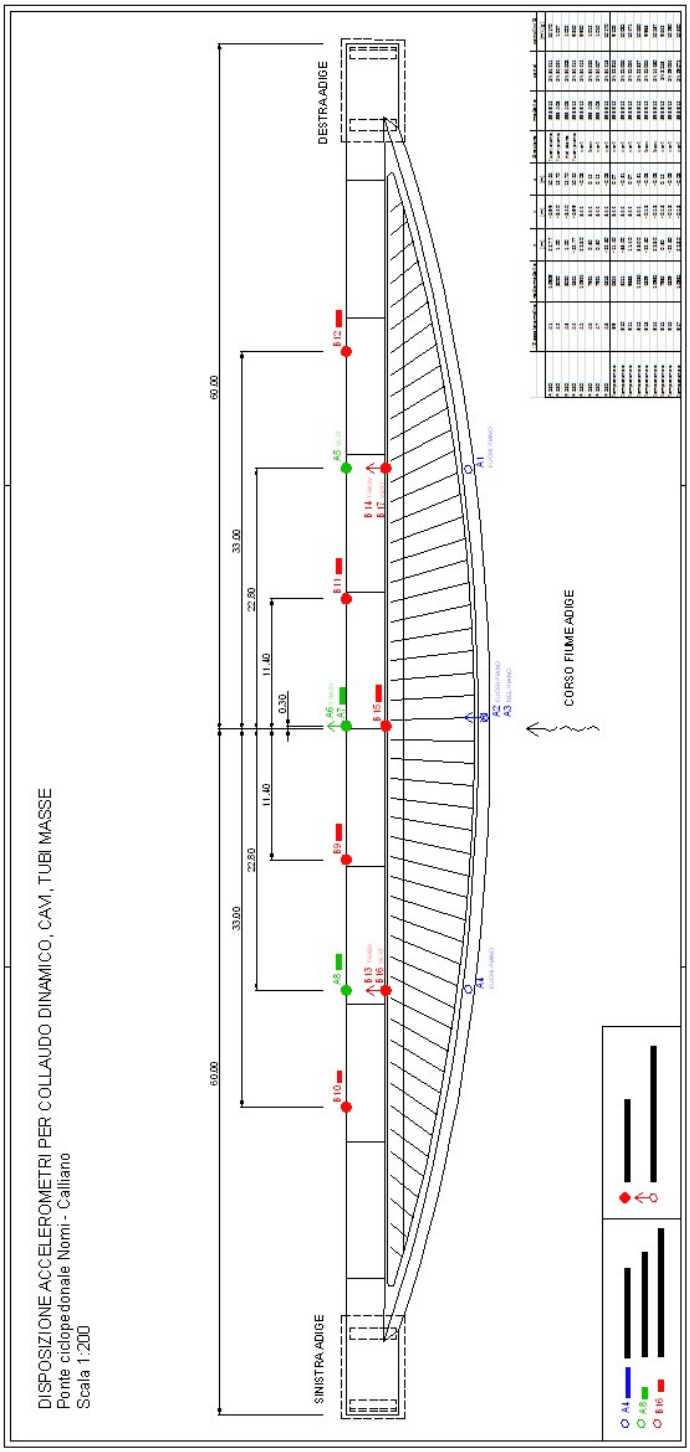

Figure 4.30: accelerometers set-up.

In more detail, all signals were acquired at 400 Hz and each test had 17 channels (8+9), becoming 18 during the hummer tests. The set of acquisition consisted in:

- environmental excitation from 12.00 pm to 14.00 pm;
- impulsive excitation due to the 26 kN mass unfasten;
- impulsive excitation due to the hummer in three relevant positions: in the middle and at one quarter of the deck and at the base of the arch;
- pedestrian load: 8 pedestrian well coordinated by means of a metronome on the natural frequencies of interest walked back and forth along the footbridge.

4.7.2 Results

Figure 4.31 shows how the first 7 vibrational modes are extremely clear (degli Studi di Trento, 2012). Identified mode shape are reported in figures 4.32 and are related to the structure partially incomplete before the TMD installation.

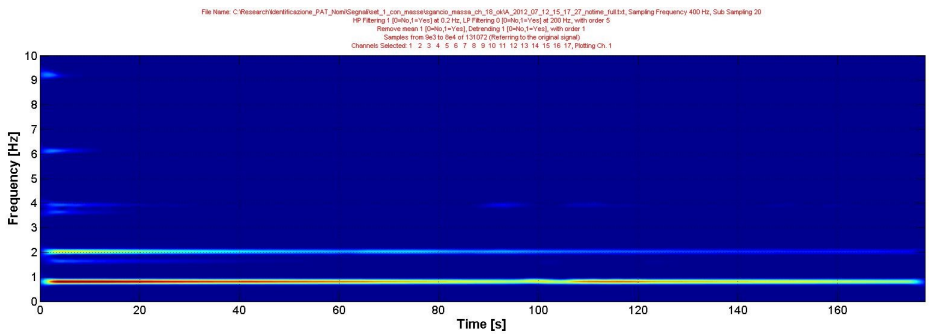

Figure 4.31: spectrogram referred to Ch.1 and generated by the test with the mass unfasten

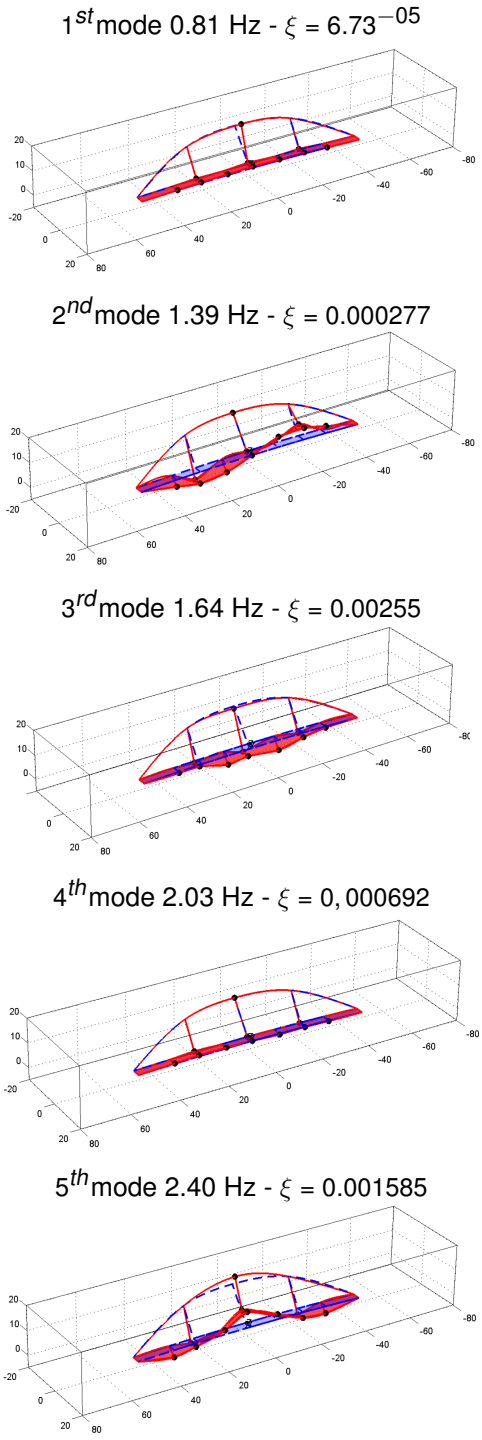

Figure 4.32: first five modes identified within the campain.

4.7.3 Refinement and updating

The refinement of the model was performed before the updating. The aim of the refinement is to have a model as similar as possible to the real identified conditions. So real situation reproduced into the model is:

- no handrails;
- presence of the masses;
- maximum soil stiffness;
- non structural elements attached to the lower part of the deck used in the construction phase and still present during the identification

In the first columns of table 4.13, the frequency variation between identified and FEM natural modes is reported. One notices that the variation appears high for both the 2^{nd} and 3^{rd} modes, with errors about the 10%-15 %. The numerical modes do not take into account for the inertial mass of the pedestrians. The first five frequencies and mode shapes are used to tune the steel elastic modulus of the FEM model. The model updating is performed updating the steel elastic modulus and using the discrete cost function in eq. 4.54. The cost function changes inside a predefined grid in order to match the vibrational properties of the model respect to the experimental data. Results of the updating are summarized in the last two columns of table 4.13. The error in decreased with a maximum value of about 8% on the 3^{rd} mode and a minimum of about 1% on the 5^{th} mode. The updating considers also the mode shapes by adding the MAC matrix in the cost function. The cost function writes,

$$obj = \sum_j p_{f,j} \left(\frac{f_{n,j} - f_{i,j}}{f_{ij}} \right)^2 + p_{m,j} \left(1 - MAC \left(\varphi_{n,j}, \varphi_{i,j} \right) \right)^2 \tag{4.54}$$

where

- $f_{n,j}$ numerical frequency of the j^{th} mode;
- $f_{i,j}$ identified frequency of the j^{th} mode;
- $\varphi_{n,j}$ numerical mode shape of the j^{th} mode;

Table 4.13: frequency variation between identified and FEM modes.

SDIT3 mode n^o	SDIT3 frequency [Hz]	ANSYS mode n^o	ANSYS frequency [Hz]	Error [%]	UPDATED frequency [Hz]	Error [%]
1	0.81	1	0.80	-1.2	0.85	4.7
2	1.39	2	1.25	-11.2	1.34	-3.7
3	1.64	3	1.43	-14.6	1.51	-8.6
4	2.03	4	1.99	-2	2.13	4.6
5	2.40	5	2.22	-8.1	2.38	-0.8

- $\varphi_{i,j}$ identified mode shape of the j^{th} mode;
- $p_{f,j}$ weight on the frequency;
- $p_{m,j}$ weight on the shape

The Hooke-Jeeves derivative free algorithm is used for the optimization. It belongs to the Direct Search family which don't assume the analytical shape of the cost function and for this reason are suitable for matching numerical and experimental data.

4.8 The damping system

On the basis of both the identified frequencies and the errors between real and updated values presented in table 4.13, a set of estimated frequencies is calculated and reported in table 4.14. These values are used to design TMDs according to the Den Hartog theory. The final design in reported in table 4.15 while the device location is shown in figure 4.33. The first mode is symmetric and involves the arch so the position of the TMD is in the center of the arch. The third mode is asymmetric and is positioned at one third of the deck span. Remaining devices damp two symmetric modes, the 2^{nd} and the 5^{th}, so they are positioned together in the middle of the deck. The footbridge is rigidly connected to the foundations in correspondence of its ends and is therefore characterized by hyperstatic external constraints. As a consequence, modal frequencies present a range of variation due to both uncertainty on the soil stiffness and gradients of temperature. In gen-

Table 4.14: estimated frequencies for TMD design.

Mode n^o	SDIT3 frequency [Hz]	Error [%]	ESTIMATED frequency [Hz]
1	0.81	4.7	0.78
2	1.39	-3.7	1.33
3	1.64	-8.6	1.56
5	2.40	-0.8	2.28

eral, de-tuning resulting from several sources such as alteration of the structural properties of the primary structure or deterioration of the TMD, leads to a loss in performance. At this purpose, a detailed study in case of extreme working condition of soil stiffness and temperature variation have been performed in Lorenzi and Bursi (2011) and resulted in a criticality on the 3^{rd} mode with a exceeding of the acceleration limit of 0.7 m/s^2. A Semi-active TMD may be a good compromise to overcome the de-tuning problem. In this case, the semi-active TMD is composed by its mass, the passive spring and the controllable damper and the control law is here used to modify only the damping. The semi-active TMD is a product of the Maurer & Sohnne company.

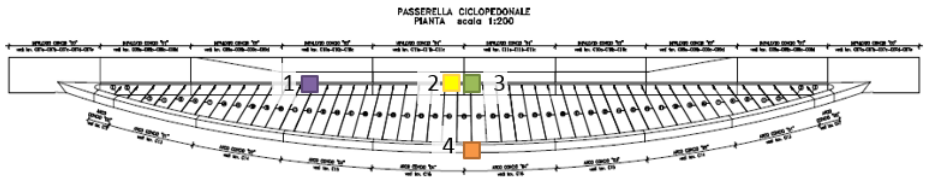

Figure 4.33: the disposition of the damping system on the footbridge.

4.9 The monitoring system

The bridge was equipped with a monitoring system integrated with the structure with the purpose of checking the actual response, with particular interest in the dynamic behavior related to the effect of wind and pedestrians. The monitoring started in May 2013 and the position of accelerometers is the one used in the experimental modal analysis campaign. In order to both identifying the wind load and to determine daily and seasonal temperature gradients on decks, the following sensors have been installed:

- 2 anemometers for the magnitude and direction of the wind: measuring range of 0-60 m/s and 0-360^o; analog output 2x4-20 mA and power supply of 12 VDC.
- 2 thermometers PT100 with 4 chords: measuring range of -150/+450^oC; precision of class B (+0.3^oC), analog output 4-20 mA and power supply of 24 VDC.
- 4 piezoelectric accelerometers 393B12: high sensitivity of 10 V/g, frequency from 0.15 to 1000 Hz, 2-pin MIL C-5015 connector.
- 4 piezoelectric accelerometers 393A03: low sensitivity of 1 V/g, frequency from 0.5 to 2000 Hz, 2-pin MIL C-5015 connector.

In addition the hardware comprises also one PXIe-6341 board for the acquisition of low signals (wind and temperature) and one PXIe-4492 for fast signals (accelerometers). The monitoring system has three type of outputs:

- Static monitoring: wind and temperature signal are acquired continuously and the sampling frequency is 1 Hz.
- Daily dynamic monitoring: all the accelerometers are acquired once a day for a duration of 328 s and with sampling frequency of 100 Hz.
- Threshold dynamic monitoring: the acquisition starts when a threshold on the acceleration, on the frequency range or on the wind velocity are exceeded. In particular, with regard accelerations, the limits are 0.07 m/s^2 and 0.035

m/s^2 for vertical and horizontal accelerometers on the deck, 0.15 m/s^2 and 0.3 m/s^2 for the out of plane and in plane, respectively, accelerometers positioned in the arch. The frequency range is 0-10 Hz and the wind velocity threshold is 14 m/s on both the anemometers.

With regard to the sensors placed on the deck, accelerations of relevant entity and induced by the cycle transit has been detected; however, the phenomena is not alarming since mainly due to the cycle impact on the wood axis not rigidly linked to the main structure. These high frequency vibrations (more than 30 Hz) are rapidly damped and do not belong to the frequency range interested by the pedestrian vibrational issue. The maximum values of vertical and horizontal acceleration on the deck in terms of RMS result to be 0.2 m/s^2 and 0.07 m/s^2, respectively.

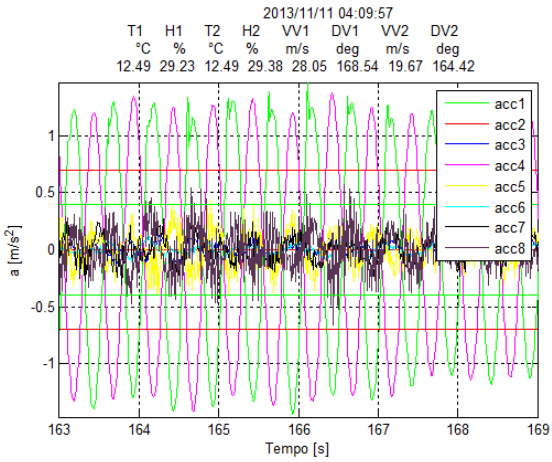

Figure 4.34: acquisition 2013_11_11_04_14_47_AFW.txt, contribution of the 4^{th}mode.

On the other hand with regard wind phenomena, the following behavior has been detected along the whole span of time interested by the monitoring. In presence of low entity wind events, the structure oscillates mainly according to the first mode; wind events with velocity higher than 15 m/s, excite the 4^{th} vibrational mode (event of 11/11/2013) since the 1^{st} one get damped by the presence of the TMD, as shown in figure 4.34. In this circumstance, the maximum values of vertical and horizontal acceleration on the deck in terms of RMS resulted to be 0.224 m/s^2

and 0.074 m/s^2, respectively. It is interesting to note that during the event of the 11/11/2013 between 1-11 a.m., the arch was interested by an high acceleration levels with magnitude higher than 1 m/s^2 while on the deck the value held around 0.4 m/s^2, so below the imposed limits.

4.10 Conclusions

The University of Trento performed the dynamic analysis of the Nomi-Calliano footbridge according to actual codes in order to avoid vibrational phenomena already observed in case such as the Solferino bridge or the Millennium bridge. The dynamic analysis led to the conclusion that a damping system composed by four TMDs needed to be added to the main structure tuned on the 1^{st}, 2^{nd}, 3^{rd} and 5^{th} mode and in order to ensure a behavior compatible with serviceability limits imposed by the owner. The campaign voted to the experimental modal analysis was organized in order to know the modal properties of the structure necessary for the correct design of the system of passive TMDs. Both impulsive and environmental excitation were used to obtain the first 7 vibrational modes. Since the identification tests were carried out on the structure not yet complete the model refinement and the model updating (Hooke-Jeeves derivative free algorithm is used for the optimization) needed to be performed in order to obtain the correct modal mass necessary for the design of the tuned devices. Correct frequencies are obtained after the model updating and model refinements and the correct design data for the passive TMDs are evaluated as a function of the adjustment process. The footbridge is rigidly connected to the foundations and therefore is characterized by hyperstatic external constraints. A detailed study in case of extreme working condition of both soil stiffness and temperature variations have been performed by the University of Trento and resulted in a criticality due to the exceeding of acceleration limits due to the third mode. The choose was oriented through the substitution of the passive TMD on the third mode with a semi-active one. After the detailed analysis and design of the damping system, the bridge was in addition equipped with a monitoring system integrated with the structure with the purpose of checking the actual response, with particular interest in the dynamic behavior related to the effect of wind and pedestrians. After the first three trimester of monitoring, no exceeding of the imposed limits is recorded. An interesting behavior is detected

and consists in the structure oscillation according to the 1^{st} mode in presence of low entity wind events; but when the wind velocity is higher than 15 $m/s$the mainly excited vibrational mode is the 4^{th}.

Table 4.15: TMD design.

M_{mod}	pos.	f	ω	m_{TMD}	μ_{eff}	α_{opt}	k_{TMD}	ξ_{opt}	c_{TMD}
$[kg]$		$[Hz]$	$[rad/sec]$	$[kg]$			$[kNm]$		$[kNs/m]$
Mode 1									
41649	1	0.78	4.91	400	1.0%	0.9905	9	0.059	0.23
Mode 2									
151521	2	1.33	8.34	2000	1.3%	0.9870	136	0.069	2.27
Mode 3									
135563	3	1.56	9.83	2000	1.5%	0.9855	188	0.073	2.82
Mode 4									
115693	4	2.28	14.31	2000	1.7%	0.9830	396	0.078	4.42

CHAPTER 5

INPUT IDENTIFICATION

5.1 Introduction

Problems are typically classified as direct and inverse, depending on what one is interested in estimating. In the direct problem, we usually have both the causes and the map between causes and effects and we search for the effects (displacements, accelerations and so on). We also may be interested in obtaining causes starting from effects as happens in the inverse problems, where we try to infer something from recorded output data sampled with a selected rate. A common inverse problem is the reconstruction of the inputs that generated a certain recorded data. This chapter deals with the input identification issue and with the analysis of associated problems. The input identificability is related to the effective possibility of reconstructing the inputs that generated the available outputs. The input

Figure 5.1: causes and effects on a structure.

reconstruction problem can be connected to several applications. For example,

damage detection can be related to the identification of some unknown inputs absent that we use to simulate the changes resulting from damage (Koupra et al., 2010). The Input Identification (ID) intended as identification of loads acting on a system can also be split up into moving (Law and Chan, 1997; Law and Fang, 2001; Yu and T., 2003) and static loads detection (Nordstrom, 2006). In this work, the input identification is used to validate the control strategies necessary for the semi-active control of the bridge and numerically simulated in the testing laboratory of the University of Trento.

5.2 Issues related to input identification

Number, location and time histories are the three aspects of the input identification problem. We focus on loads that are fixed in space and are applied to systems with a linear and time invariant behavior, while the input/output (I/O) map is available from a Finite Element model or from modal identification. A review of the literature indicates that a survey on both the magnitude and the time history of the loads have already received attention in many different fields since the demand of knowing the unknown load involves several branches such as impact load (Doyle, 1997; Inoue et al., 1995), contact force (Doyle, 1984) and damage detection (Koupra et al., 2010). In most cases, the input number and position is assumed to be given and one has not to do the same kind of effort about this information, since they are typically assumed to be known. A focus on the latter topics is in Maia et al. (2012), namely both the force numbering and localization are obtained by means of the concept of transmissibility of motion and using both the available measured responses and a numerical model. The method adopts a trial and error procedure that assumes an increasing number of forces acting on the system and their consequent combinations. A series of force number and position is numerically generated and for any combination, the expected responses obtained from a trial transmissibility matrix are compared with the measured ones. If the trial and the real transmissibility matrix are the same, a minimum in the difference between expected and real responses can be found and consequently the number and position of the inputs can be associated to the smallest response error. The limit here is the large number of combinations necessary to find this information and the fact that the model is always indispensable. In the first part of this chapter, we address

the question of determining the number and the spatial position of the inputs given a set of outputs and a model of the system. The premises are that the inputs are less than the number of outputs, they are persistently exciting the system and that the latter is linear and time invariant. The number of inputs and their position can be identified without difficulty using data and a model. It is shown that the number of inputs can be obtained from the effective rank of a matrix that can be formulated from the Fourier transform of windowed versions of the response signals and that the information on their location is encoded in the image of the same matrix. After the definition of the number of inputs, there is no assumption made regarding their spatial distribution. Namely, an input is a time history and it may be applied at one or at more than one location simultaneously. In a first phase, we restrict the attention to the case where loads are applied at distinguish points, so one time history means one load, two time histories mean two loads and so on. In a second phase, the presence of multiple inputs with both repeated time history and magnitude is addressed. It appears clear that it is mandatory to operate off line with a sufficiently long record when the three above mentioned aspect are examined at the same time. Furthermore, causes do not produce effects instantly since real problems are characterized by the presence of the inherent delay between inputs and outputs. The inherent delay is related to the wave propagation speed that characterizes the system. In this scenario, it appears evident that is not possible to speak in terms of ”real time“ if this means to find the input at exactly the same instant it occurred. In other words, sensors may be not necessary located in positions that guarantee the direct transmission of the sources to the outputs and this implies that we need time in order to receive information. This range of time is the Delay Range (DL) and within this range, the output values are exactly zero. Taking into account this consideration and in presence of problems where the input number and the locations are already known, the time histories can be computed in online fashion although not in real time. On the other hand, we usually manage models that assume the existence of a finite dimensional (FD) system that is the result of the discretization in space. It follows that during simulations, the use of discretized models may violate physics twice. 1) The state space model does not engrain the inherent delay of the real system and consequently they led to algorithm that can-

not work in general. 2)Finite element discretization of a continuum does not have impulse response functions with zero finite time segments. So the part of the impulse response functions that are zero in the continuum are very small in the model. The simulation of the discrete time system produces ”small“information during the delay phase that sometimes we pretend to use for identification purposes even if in reality there is absolutely no information because, in this delay span, there is no motion field. While in the forward problem, the delay and the ensuing zero outputs are not a critical point, on the other hand in the inverse problem of the input identification, we need to pay attention to this issue. Indeed, conditions 1) and 2) let to misguided attempts to avoid the non-minimum phase nature of the problem by the use of the ”not exactly zero“ values that are large respect to the machine precision. In the light of these considerations, it is evident that the term ”real“ associated with the input identification has no meaning because the input identification has at least one time step of delay. The input reconstruction can be just ”on line“ or ”off line“. On line algorithms must contain a ”delay parameter“ if they have to work in real problems. In addition, the input reconstruction can be handled in the frequency domain (Hwang et al., 2009) or in the time domain (Law et al., 2005; Lu and Law, 2006) if the inherent delay of the system and consequently the lag for the input reconstruction is relevant. In the time domain, the general solution of the inverse problem is simply obtained from the deconvolution of the impulse response from the output measurements. However, the deconvolution must be constrained by the true physics of the problem in order to avoid the formulation of ill-posed problems. In fact, the I/O arrangement and the inherent delay of the problem define if the input is identifiable or if it is identifiable on any subspace. It can be shown that the part of the input affected by the delay is strictly related and can be detected through inspection of the Toeplitz matrix kernel. This approach to the inverse problem has received much attention but the kernel structure has not been deeply investigated as a tool to connect the properties of the matrix H with the part of the solution not affected by the delay. In this respect, the well posedness of the problem implies the numerical stability of the solution. However a stable system can still be poorly conditioned. In fact, stability and conditioning are two different issues related to the problem of the input reconstruction even if they sometimes appear to be mixed

up. The ill conditioning is due to the sensitivity of the solution to noise in measured data and to error in initial conditions, and it shows up when the spectra of noise realization is outside the bandwidth of the system. The inputs act on the range of time and there are no loads supported on this range that give zero outputs. Consequently, in order to find the unique solution of the Deconvolution Problem (DP), it is necessary to avoid loads that can be added to the system without changing the output itself. The ill conditioning mirrors in the fact that there are many high frequency solutions of the ID problem, which match the recorded input.

5.2.1 The deconvolution approach

The equation of motion expressed with the discrete state space model reads,

$$\begin{aligned} x_{k+1} &= A_d x_k + B_d d_k \\ y_k &= C_d x_k + D_d d_k \end{aligned} \tag{5.1}$$

where $x_k \in \mathbb{R}^{2n}$ is the state vector, $d_k \in \mathbb{R}^r$ is the input vector and $y_k \in \mathbb{R}^m$ is the measurement vector. A_d, B_d, C_d and D_d are real matrices of appropriate dimension, respectively, the system matrix, the input influence matrix, the output influence matrix and the direct feed-through matrix. Solving for the output with zero initial conditions, yields

$$y_k = \sum_{i=0}^{k} Y_k d_{k-i} \tag{5.2}$$

where $Y_0 = D$ and $Y_i = CA^{i-1}B$ are the Markov of the system. This equation is written to provide the matrix convolution equation,

$$y_k = H_k d \tag{5.3}$$

The coefficient matrix H is an upper-block triangular Toeplitz matrix. Hence, the deconvolution problem has the following general solution,

$$d_k = H^{-*} y_k + N(H)h \tag{5.4}$$

where $N(H)$ is the null space of H and h is an arbitrary vector of appropriate dimension. The deconvolution problem can be addressed in several ways and can display ill-posedness or ill-conditioning. This approach is presented in Law et al.

(2005); Bernal and Ussia (2013) and it's based on finding the input force sequence U for a known sequence of outputs y_k. In the trivial case, H is full rank and the inverse problem is easy to treat because the null space of H is an empty space and we just need to invert a full column rank matrix; this is the special case of collocated measurements of acceleration with number of output greater than number of inputs. In this special case, the solution for the input is already recognizable as unique. In the most part of the cases, however, H is rank deficient and the null space of H is not an empty space and, as consequence, the solution is not unique on the complete output set. Nonetheless, this does not mean that there is no solution.

5.2.2 Input-output relations in time-domain

Let's consider a state space LTI system in discrete time in eq. 5.1, the dynamic response to a general input is already built into the model,

$$x_k = A_d^k x_0 + \sum_{i=0}^{k} A_d^{i-1} B_d d_{k-i} \tag{5.5}$$

and the corresponding output reads,

$$y_k = C_d A_d^k x_0 + \sum_{i=0}^{k} C_d A_d^{i-1} B_d d_{k-i} + D_d d_k \tag{5.6}$$

The output equation can be rearranged in order to highlight the Markov parameters Y_k . In this form it appears evident that the outputs are the result of the convolution between the Markov parameters and the input load.

$$\begin{bmatrix} y_0 \\ y_1 \\ ... \\ ... \\ y_{k-1} \\ y_k \end{bmatrix} = \begin{bmatrix} C_d \\ C_d A_d \\ ... \\ ... \\ C_d A_d^{k-1} \\ C_d A_d^k \end{bmatrix} x_0 + \begin{bmatrix} Y_0 & 0 & 0 & 0 & 0 & 0 \\ Y_1 & Y_0 & 0 & 0 & 0 & 0 \\ Y_2 & Y_1 & Y_0 & 0 & 0 & 0 \\ Y_3 & Y_2 & Y_1 & Y_0 & 0 & 0 \\ ... & ... & Y_2 & Y_1 & Y_0 & 0 \\ Y_k & ... & Y_3 & Y_2 & Y_1 & Y_0 \end{bmatrix} \begin{bmatrix} d_0 \\ d_1 \\ ... \\ ... \\ d_{k-1} \\ d_k \end{bmatrix} \tag{5.7}$$

The compact form reads

$$y_k = Ob_k x_0 + \sum_{i=0}^{k} Y_i d_{k-i} \tag{5.8}$$

where $Ob_k = C_d A_d^i$, $i = 0, ..., N$ are the elements of the observability matrix with $Ob_k \in \mathbb{R}^{mNxn}$ and N number of steps, $Y_i \in \mathbb{R}^{mxr}$ are the Markov parameters. If we define that $H \in \mathbb{R}^{(mxr)N}$ is the Toeplitz matrix and the initial conditions are non zero, the well know formulation of the convolution problem holds,

$$y_k = Ob_k x_0 + Hd_k \tag{5.9}$$

or, in a simplified formulation with zero initial conditions,

$$y = Hd \tag{5.10}$$

where

$$y = \begin{bmatrix} y_0 \\ y_1 \\ ... \\ ... \\ y_{k-1} \\ y_k \end{bmatrix}, \; d = \begin{bmatrix} d_0 \\ d_1 \\ ... \\ ... \\ d_{k-1} \\ d_k \end{bmatrix} \tag{5.11}$$

The deconvolution of the above equation is a critical aspect of the input reconstruction problem. The problem may not be well defined or posed indeed, because one may ask for the wrong question.

5.3 Number and location of inputs

We focus on the case of point loads that are fixed in space and that act on systems that are linear and time invariant. We address the question of determining the number and the spatial position of inputs given a set of outputs and, once located, the question of estimating time histories. The localization problem is solved using an approach that shows that the number of independent inputs can be extracted from the Fourier transform of the measured output data and that their position can be established with the aid of a model without the need for performing a combinatorial inspection of all the possible scenarios. Output data from a real system are continuous and given the non-stationarity of the input the Continuous Time Fourier Transform should be used (CTFT). The number and location problem is solved using a multiple experiment scheme that in practice is realized by dividing

the output signals into segments and by data sampling. In addition the Fourier Series perspective is adopted since the input in each segment is assumed periodic (which, of course, it is not). However, the initial conditions are not zero at the start of each segment and the arising approximation is due to the coefficients of the Fourier series expansion. The observations of the output are ”truncated“ since the response to the input in each window extends beyond the window itself, and as consequence, the output is ”inconsistent“ with the assumptions at the start of each segment for a time span that depends on the decay rate. In each segment, the approximation necessarily leads a loss of resolution so other variables - such as the size of the windows respect to the damping rate and the frequency inspected - start to matter. Notwithstanding, adequate accuracy can be obtained by using a Hanning window on the output and ensuring that the signal is sufficiently long so the fraction of the segments that is affected by initial conditions is not too large, that means that a good accuracy is obtained if the segments are long compared to the decay time of the free vibrations. Once the loads are located the histories can be estimated with a minimum lag that is affected by wave propagation delays but that is typically controlled by stability requirements. As is well-known, satisfying stability does not ensure accuracy and in this regard the paper shows that a key issue in attaining good conditioning is that the spectrum of the inputs that are to be identified, and the noise that is realized at the measurements, is contained within the bandwidth of the model.

5.3.1 On the number

Given the standard discrete-time space problem, the system outputs in the frequency domain are linear combination of the system transfer function,

$$Y(\omega) = G(\omega)U(\omega) \tag{5.12}$$

where $G(\omega)$ is the transfer matrix, $Y(\omega)$ is the transformed output signal and $U(\omega)$ is the input transform. In terms of the j^{th} experiment or window,

$$Y_j(\omega) = G(\omega)U_j(\omega) \tag{5.13}$$

The rank of $Y(\omega)$ is limited by the smaller rank of the matrices that appear into the product on the right hand side of eq. 5.13. At any given frequency $\omega = \omega_i$

and assuming that the number of experiment or window, is much greater than the number of outputs ($n_w > n_m$), the Fourier Transforms of the output can be gathered into a matrix called B_{fft} with number of rows and columns equal to the number of sensors and the number of experiments, respectively.

$$B_{fft}\{\omega\}(n_m, n_w) = \begin{bmatrix} & full & \end{bmatrix}_{n_m x n_w} \tag{5.14}$$

Since the vectors $Y_j(\omega)$ are the columns of the matrix $B_{fft}(\omega_i)$ and since each column of $B_{fft}(\omega_i)$ are linear combination of the transfer function $G(\omega_i)$, the rank of $B_{fft}(\omega_i)$ cannot exceed the number of independent inputs that is encoded in the product in eq. 5.13. In this respect, the Singular Value Decomposition (SVD) of the matrix $B_{fft}(\omega_i)$ provides information about input locations. The SVD of $B_{fft}(\omega_i)$ reads,

$$\begin{bmatrix} U(\omega_i), & S(\omega_i), & V(\omega_i) \end{bmatrix} = \begin{bmatrix} & full & \end{bmatrix}_{(n_m x n_m)} \begin{bmatrix} \# & & \\ & \# & \\ & & \# \end{bmatrix}_{(n_m x n_w)} \begin{bmatrix} & full & \end{bmatrix}_{(n_w x n_w)} \tag{5.15}$$

where $S(\omega_i)$ is the singular value matrix, $U(\omega_i)$ and $V(\omega_i)$, are the left and the right singular vector, respectively After rearranging the SVs corresponding to the frequency $\omega = \omega_i$ into the columns of the matrix $S_{sv} \in \mathbb{R}^{n_m x n_f}$, then the rank of S_{sv} shows the number of independent loads acting on the system. The numerical test refers to an 8-DoF uniform chain with unit masses and first fundamental mode frequency of 1.17 Hz. Inputs are Gaussian noises and are on the 1^{th} and 5^{th} DoF whilst measured outputs are accelerations in sensors #2, #3, #4, #6, #7, # 8. When it is not possible to collect N sets of data, it is necessary to take a long unique signal and divide it into segments providing a shift from the conceptual framework of the continuous Fourier transform to a periodic analysis in terms of Fourier series. Nevertheless, as the window size grows the relative importance of this error source decreases and for sufficiently long widows (the necessary length depending on the

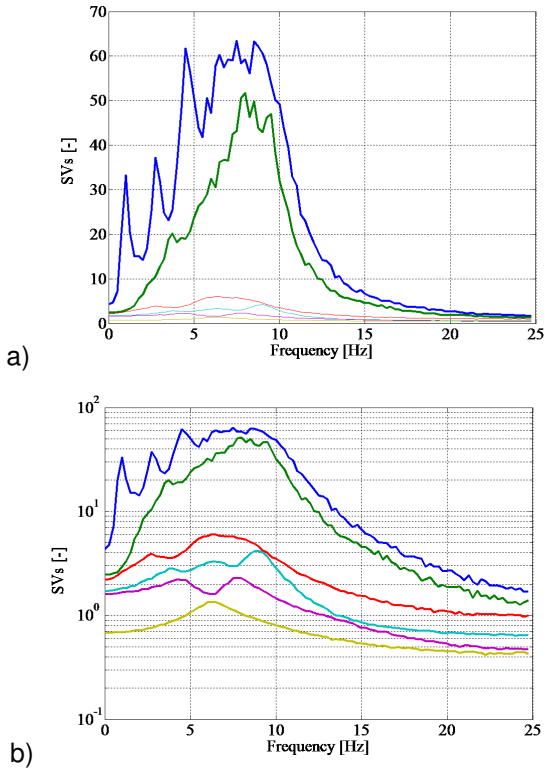

Figure 5.2: input quantification in a) linear and b) logarithmic scale

damping) and sufficiently accurate results can be obtained. From an implementation perspective, the approach is essentially the same as if using different tests, except that the output is windowed and it's transformed to frequency using the FFT in order to overcome to the periodic assumption. The FFT procedure is indeed sensitive to the window length not only respect the magnitude of each singular value, but also respect the ratio between the bigger and the smallest one. The increased ratio simplify the inspection of the plot and makes clearer the identification of the number of applied inputs since the small singular values tend really to zero. In this respect, we illustrates what happens when the sensitive variable changes size as a function of the highest period of the structure. Fig.5 shows that the clarity in the rank definition increases by increasing the window dimension where the window sizes are 1T, 4T, 15T and 30T, as shown in figure 5.3 a), b), c) and d), respectively. Last issue to keep in mind to search for the rank of the objective matrix, is that

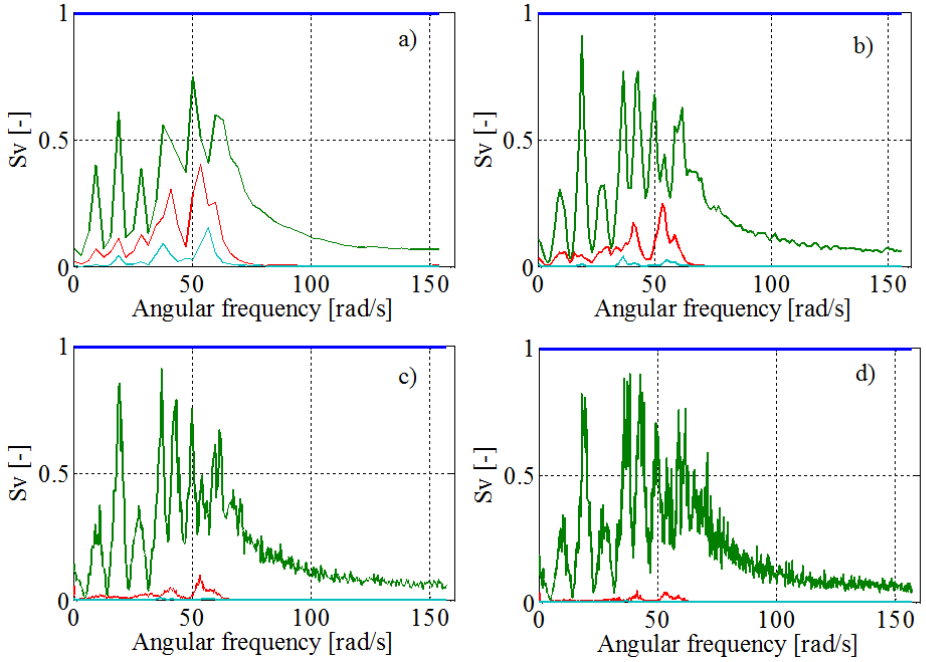

Figure 5.3: rank definition as a function of the window size.

the number of windows must be much greater than the number of outputs, so this condition defines a constraint about the minimum length of the original signal. In addition, around the resonance or in general inside the system bandwidth, it is not obvious to understand clearly the matrix rank since the peaks due to the transfer function cloud the information. As consequence, an extension of the inspected frequency range respect the system band is mandatory.

5.3.2 On the location

Once the number of input is defined, it is also possible to infer information about the acting loads position since $B_{fft}(\omega_i)$ also includes information about them. The columns of the left singular vector $U(\omega_i)$ related to the not small singular values of $B_{fft}(\omega_i)$ and consequently to the number of inputs, are named $Q(\omega_i)$ and writes,

$$Q(\omega_i) = U(:, 1 : \#input) \tag{5.16}$$

$Q(\omega_i)$ is span for $B_{fft}(\omega_i)$ and for both $G(\omega_i)$ and $B_{fft}(\omega_i)$ when the input location is the same. As consequence the span of $B_{fft}(\omega_i)$ is the same of the columns of the

transfer matrix if the columns are associated to the correct position of the inputs. If the angle between the two subspaces is small, the two spaces are nearly linearly dependent and the base of the two subspace is the same. In addition, we have a model, so it is possible to try all the load combinations in order to find the one that make the angle between two subspaces minimum: one subspace is specified by the columns of $B_{fft}(\omega_i)$ and the other by the columns of $G(\omega_i)$. $G(\omega_i)$ is a function of B_d or in other words, it depends by the input number and location. If the input location is correct, the subspace angle is minimum. Note that in the benchmark test with 8-DoFs, the combinations should be the following,

$$\begin{array}{l} Comb_1 = [1,2] \\ Comb_2 = [1,3] \\ Comb_3 = [1,4] \\ Comb_4 = [1,5] \\ Comb_5 = [1,6] \\ Comb_6 = [1,7] \\ Comb_7 = [1,8] \end{array} , \quad \begin{array}{l} Comb_8 = [2,3] \\ Comb_9 = [2,4] \\ Comb_{10} = [2,5] \\ Comb_{11} = [2,6] \\ Comb_{12} = [2,7] \\ Comb_{13} = [2,8] \end{array} , \quad \begin{array}{l} Comb_{14} = [3,4] \\ Comb_{15} = [3,5] \\ Comb_{16} = [3,6] \\ Comb_{17} = [3,7] \\ Comb_{18} = [3,8] \end{array} \tag{5.17}$$

However, in order to avoid the test on each combination, a second procedure can be used. It is possible to evaluate the position of a single input individually. In the same way, the information about each individual location is encoded into the columns of the left singular vector and it suffices understand which columns of the transfer matrix are contained in the span of $B_{fft}(\omega_i)$. Figure 5.4 is clearly visible that inputs are on the 1^{th} and 5^{th} DoF. Another issue is whether there is any input that is ”repeated“, namely, acting at more than one location. The test in figure 5.5 is referred to a 10 DoF system and corresponds to the case where we have a total number of inputs with n repeated time histories and with the same amplitude (in other words, we have two repeated time histories in position #2 and #5). Since the subspace angle in the band of the system is totally clouded, the previous non combinatorial analysis does not allow for correct positioning; see in this respect figure 5.5 a). This because the number of columns of b_2 is equal to the number of not repeated loads (one in this case) but its pattern is a combination of the two repeated inputs. Consequently, the presence of repeated inputs requires (in our approach anyway) a combinatorial analysis in order to correctly span the range of

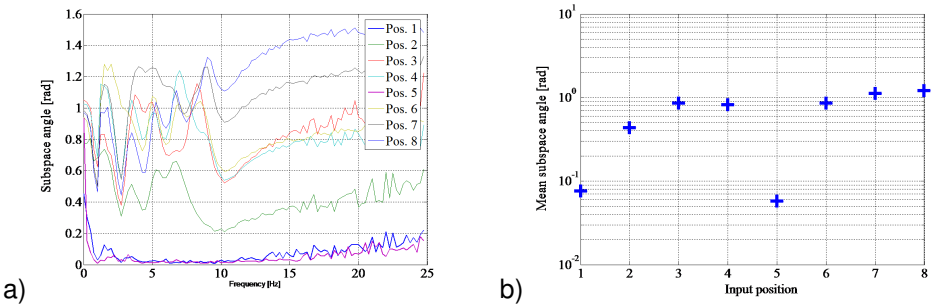

Figure 5.4: input position by a) inspection of the subspace angle vs frequency; and b) inspection of the means subspace angle related to each DoF.

the left singular vectors. This approach is not scalable if the number of repetitions is large, and consequently this issue can be a limitation in the case of large models. Anyway, the combinatorial analysis of figure 5.5 b) is satisfactory and correctly define the two locations.

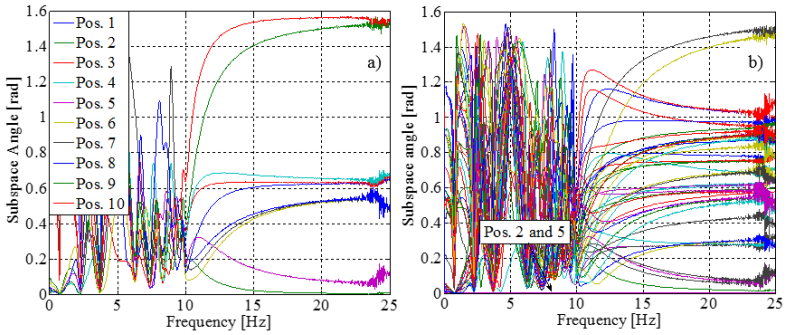

Figure 5.5: input position with repeated inputs: a) subspace angle vs. frequency without combinatorial analysis; and b) subspace angle vs. frequency with combinatorial analysis

5.4 Identificability

In literature (Bertero and Poggio, 1988), the identificability problem is usually presented as follows. Given the problem $y = Hd$, where $H : U \rightarrow Y$ is the linear continuous operator that map the space U into another space Y. We define $d \in U$ as the solution and $d_\epsilon \in U$ as the exact solution. The problem is well posed in

the sense of Hadamard, on the pair of topological spaces U and Y, if the following conditions hold:

1. Existence: given $\forall y \in Y$ exists a solution $d_\epsilon \in U$ of $y = Hd$ and $y : R(H) = Y$. This means that the solution exists and belong to the range of H.

2. Uniqueness: the solution d_ϵ is unique in U, i.e. there exists an inverse operator $H^{-1} : Y \rightarrow U$.

The problem is ill posed if one of the above conditions does not hold. In order to define the identificability concept, let's consider another approach. The Markov formulation of the direct problem with non-zero initial conditions within the time range $[0, \ell]$ results to be,

$$y_{[0,\ell]} - Ob_\ell x_0 = Hu_{[0,\ell]} \tag{5.18}$$

The general solution of eq. 5.18,

$$u_{[0,\ell]} = H^{-*} y_{[0,\ell]} - H^{-*} Ob_\ell x_0 + Zh \tag{5.19}$$

where $H \in \mathbb{R}^{(\ell_1 m) x (\ell_1 r)}$, Ob_ℓ is the observability block of order ℓ, ℓ is the total number of time steps and $\ell_1 = \ell + 1$ is the total number of time stations, $,^{-*}$stand for pseudo-inversion, $Z = N(H)$ is the null space of H and h is an arbitrary vector of appropriate dimension. If H has a null space, the general expression for the solution d yields,

$$\begin{bmatrix} u_0 \\ ... \\ u_p \\ u_{p+1} \\ ... \\ u_\ell \end{bmatrix} = H^{-*} y_{[0,\ell]} - H^{-*} Ob_\ell x_0 + Zh = \begin{bmatrix} u_0 \\ ... \\ u_p \\ \#_{p+1} \\ ... \\ \#_\ell \end{bmatrix} \tag{5.20}$$

where # is the part of solution u affected by the non-zero rows of $N(H)$. This means that the solution is not unique in this range. The null space of H is empty if data are collected from collocated accelerations. In this case there is only one set of d that gives the field y. Otherwise, the null space is a not empty space. The dimension

of the null space increases if the distance between the input and output position increases. Displacement measurements also increase the dimension of the null space. The dimension of the null space is relevant because it is an expression of the causality and consequently of the posedness of the iverse problem. The response of the FD model has time range $[0, \ell]$ but available information about the input are constrained over $[0, \ell - d]$, where d is some delay related to the not zero columns of the kernel of H. The observation of the kernel structure might avoid ambiguity related to the delay influencing the input estimation. If data are collected from collocated accelerations, then the null space of H is empty and consequently there is only one set of $u_{[0,\ell]}$ for the set $y_{[0,\ell]}$ since $Z = 0$. Otherwise, the null space is a not empty space and the inputs are identifiable within the range $[0, p]$ if the initial conditions are known and the kernel of H is of the form,

$$Z = \begin{bmatrix} 0_{pr\,x\,(\cdot)} \\ \bar{Z}_{(\ell_1 - p)r\,x\,(\cdot)} \end{bmatrix} \tag{5.21}$$

The response of the FD model has time range $[0, \ell_1]$ but the available information

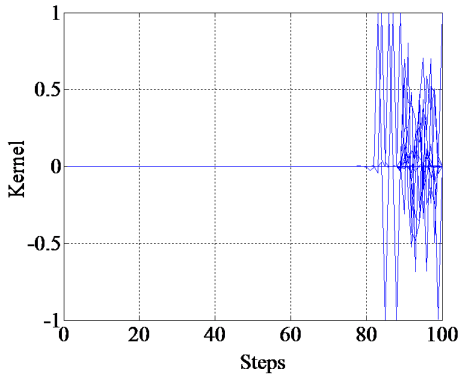

Figure 5.6: example of non empty null space.

are constrained over $[0, \ell_1 - p]$ by the not zero values of the rows of the kernel of H. The observation of the structure of the kernel avoids ambiguity related to the delay influencing the input estimation. Assuming the existence of the partition called Q_p in the form

$$Q_p = \begin{bmatrix} I_{pxr} & 0_{(pr)\,x\,(\ell_1 - p)} \end{bmatrix} \tag{5.22}$$

where p is the number of time stations and r is the number of inputs, the reconstructed input over $[0, p]$ is simply,

$$u_{[0,p]} = Q_p H^{-*} y_{[0,\ell]} - Q_p H^{-*} Ob_\ell x_0 + Q_p Z h \tag{5.23}$$

the pre-multiplication by Q_p selects the first p values of the identified input vector that is the part of the solution not affected by the null space, given that the necessary and sufficient condition for the input to be identifiable over p is,

$$Q_p Z = 0 \tag{5.24}$$

As noted before, the only form of Z that satisfies eq. 5.24 is in eq. 5.21. Since the necessary and sufficient condition for the uniqueness of $\bar{u}_p$ is that $Q_p Z$ is zero, the solution eventually writes

$$u_{[0,p]} = Q_p H^{-*} y_{[0,\ell]} - Q_p H^{-*} Ob_\ell x_0 \tag{5.25}$$

Tests on the kernel of a rod are shown in the following. The rod has a sectional area A = 4, Elastic modulus E = 100, density ρ = 1 and length L = 10. Numerically the rod can be modeled as a M-DoF composed by 40 masses. Since the wave velocity through the material is equal to $c_0 = \sqrt{\frac{E}{\rho}}$, the time necessary for a wave to pass through the rod is 1 s since the rod length is 10 units. The sampling time is 0.05 s and the damping ratio is 2%. The 40-DoF uniform chain system is shown in 5.7a with the load at coordinate #40 and the output at coordinate #1 and then moved at coordinate #20. 5.7b and c shown the kernel of both the cases. In the first case, the kernel is zero, except for the last 20 steps which correspond to the 1.0 second wave propagation time if dt = 0.05 s. Considering now that the output is in the middle of the system, the time of the wave propagation decreases to 0.5 seconds and consequently the kernel is zero for just the last 10 steps. Other two situations are described in figure 5.8a. In this case, we want to show that even in the presence of a further sensor in position #20 in addition to sensor #1, the delay time (see 5.8b) is exactly the same of the SISO case with output just at coordinate#20 (as shown in 5.8c). Indeed, the input is in the position #40 and the additional sensor is too far to reduce the delay time that remains 0.5 s. Let's now consider the same rod with now 2 acting loads located in position #5 (load #1) and

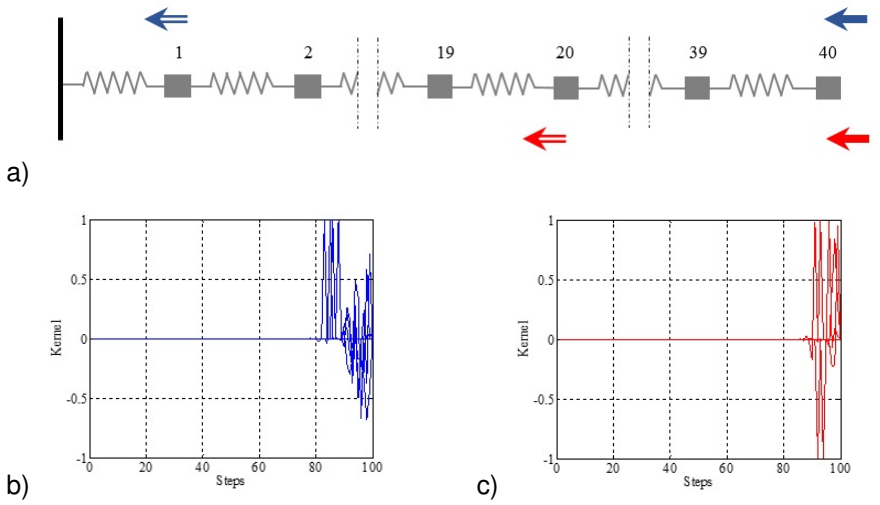

Figure 5.7: kernel of a 40-DoF chain system subjected to variation of the sensor location a) the model; b)SISO with the input in #40 and output on #1; and c) SISO with the input in #40 and output on #20.

#40 (load #2) and sensors are in position #2, #10 and #30, as shown in 5.9. The kernel rows have two sensitive information each related to each input. Bearing in mind that we always need a number of sensors greater or equal to the number of loads, the delay time necessary to the input #2 (in position #40) to reach the closest sensor in position #30 and to go through 10 masses is 0.25 s and 5 steps (magenta line) while the delay time necessary to the input #1 (in #5) to reach the nearby and closest sensor in position #2 is 0.125 that corresponds to 2.5 steps (blue line). For this specific configuration the identificability of both the inputs is ensured after 0.25s. After 0.125 s, there is just one sensor (#2) giving information about the load in position #5. After a while, also sensor in position #10 is receiving information about the same nearby load #1, but no information is arriving yet from the load in position #40 (at this point the problem is ill-posed even if we have the same number of sensors and inputs). After 0.25 s also information about load #2 arrives and the mathematical problem results to be well posed. Eq. 5.18 can be seen from a different point of view. If we are able to find the partition of H such that

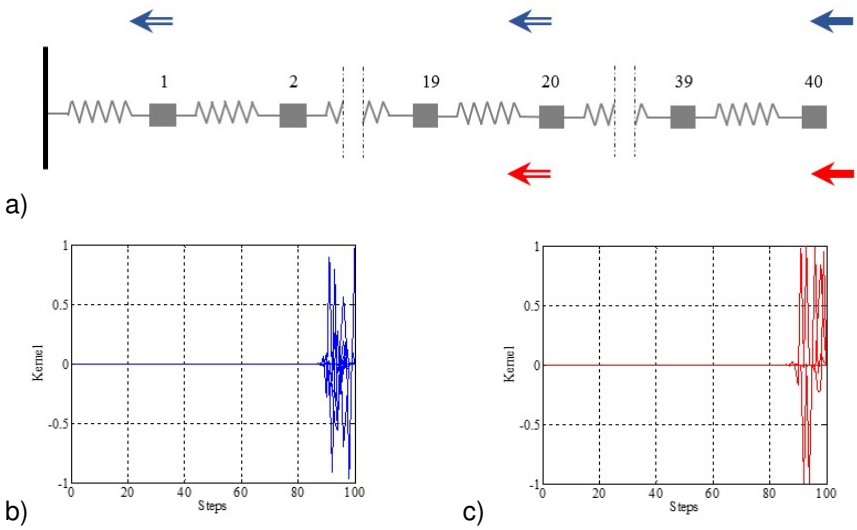

Figure 5.8: kernel of a 40-DoF chain system subjected to variation of the sensor location: a) the model; b)SIMO with the input in #40 and outputs on #1 and #20; and c) SISO with the input in #40 and output on #20.

$H_d \in^{(\ell_1 m)\ x\ (pr)}$ and $H_p \in^{(\ell_1 m)\ x\ (\ell_1 - p)xr}$, then

$$y_{[0,\ell]} - Ob_\ell x_0 = \begin{bmatrix} H_p | & H_d \end{bmatrix} \begin{bmatrix} \bar{u}_p \\ \bar{u}_d \end{bmatrix} \tag{5.26}$$

with $\bar{u}_p = u_{[0,p-\ell]}$ and $\bar{u}_d = u_{[0,\ell]}$. The resulting output is the sum of two parts,

$$y_{[0,\ell]} - Ob_\ell x_0 = H_p \bar{u}_p + H_d \bar{u}_d \tag{5.27}$$

In order to cancel the part related to the null space H_d, if we are able to find N_d, the solution can be reformulated as follows,

$$N_d y_{[0,\ell]} - N_d Ob_\ell x_0 = N_d H_p \bar{u}_p \tag{5.28}$$

and

$$\bar{u}_p = (N_d H_p)^{-*} N_d y_{[0,\ell]} - (N_d H_p)^{-*} N_d Ob_\ell x_0 \tag{5.29}$$

As shown in Bernal and Ussia (2013), by inspection of the size of H_p and H_d, it is possible to show that the number of outputs must be greater than the number of inputs to be identified. It is interesting to highlight a pedagogical step. The

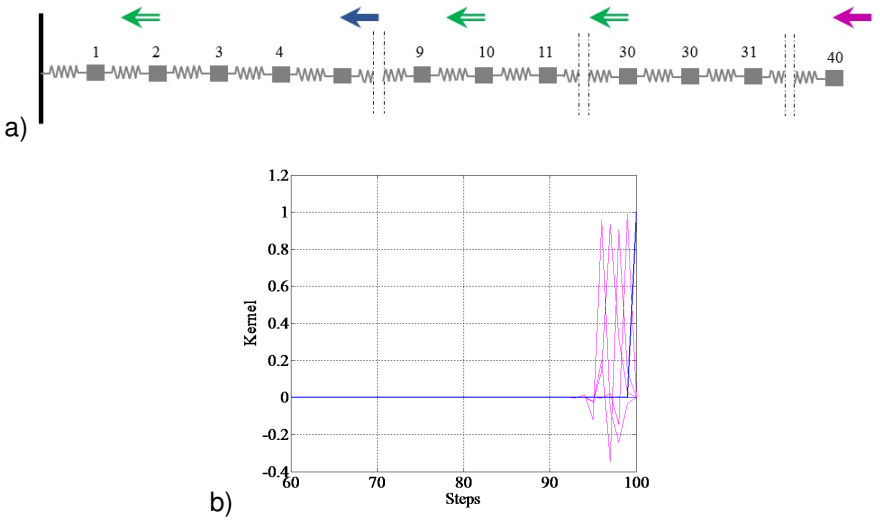

Figure 5.9: kernel of a 40-DoF chain system with inputs in position #5 and #40, a) the model; b) the kernel

existence of the kernel of H is guaranteed by the rank deficiency of the matrix itself. If H is rank deficient, it follows that also the partition H_d it is. Obviously, the kernel of H is just a subset and not a complete basis for N_d and N_p but at the same time it is a kernel for the two partitions H_p and H_d. This is the reason why we cannot use the kernel $N(H)$ in order to cancel the part of the solution affected by the not zero row of the kernel itself. In conclusion, the necessary condition for $\bar{u}_p$ to be identifiable is that H_d be rank deficient in order to ensure the existence of its kernel N_d. The fraction $\bar{u}_p$ of the solution u is so unique for $[0, p]$ and the partition for which this happens define the identifiable part of the input u. Indeed, there is a unique solution for a portion of the input and this set is called the identifiable set. The discussion leads to the evidence that the well posedness may be restored over a partition of the solution space or in other words over a partition of the available data. Searching for u given the whole set of data may drags to an ill posed problem while searching for u_p using the same set or searching for u using just a subset of the output data provide a well posed problem, but it can still be ill conditioned or unstable. The results show that the ill posedness may be removed just providing more information to the problem (the lag delay, i.e. the functional space of interest),

$$\begin{cases} ill: & find\ d_k\ given\ y_0 - y_k \\ well: & \begin{cases} find\ d_{k-\ell}\ given\ y_0 - y_k \\ find\ d_k\ given\ y_0 - y_{k-\ell} \end{cases} \end{cases} \tag{5.30}$$

Restoring existence and uniqueness means to redefine the solution U or the data set Y. The null space of H is a closed subspace of U and represents the subspace of invisible objects since it produces a zero image y of in Y. The range of H - $R(H)$ - is a closed subspace of Y and it is the subspace of visible objects since it produces a set of y that are images of some $u \in U$. In other words, the set of invisible objects is the part of solution that we want to discard and the set of visible objects is the part of data that we want to use. Let be U and Y spaces and let $U' \subset U$ be a fixed set. Now, we denote by $H(U')$ the image of U' under the map $H : U' \to Y'$ where $H(U') = Y' \subset Y$. The new subset Y' is in the range of H while U' is in the range of all the functions $\perp N(H)$. Well or ill posedness may depend from the question we are asking for. The ill posedness arises because the topological subspaces to be used for the restored solution are not yet defined. Their redefinition restores the well posedness of the problem but not necessarily also the well conditioning or the stability of the solution.

5.5 The segmented deconvolution algorithm

Reality is different from simulation. In treating with real problems there are several issues related to time and space discretization of the problem, indeed. The sampled measurements are corrupted by noise, the initial conditions are usually unknown, the impulse response function of the FD system have no dead time and the dimension of the inverse problem may be huge, since it increases also because of the number of time steps. In detail, the last condition is related to the fact that the time range and the sampling time of the measurement can lead to a big number of step and consequently to a huge dimension of the H matrix. For large dimension of the time vector, the batch (or off-line) mode became computationally impracticable and we necessarily have to deal with windows. The format of the inverse problem is the same but the windows authorize to reduce the dimension of the deconvolution problem and consequently to solve the whole problem in smaller

pieces. In this way, we work in a recursive fashion with the finite precision of the machine and solve the problem respect the part that is unique, i.e. the part that has $N_d H_p$ with full column rank. The SDR algorithm is outlined in Bernal and Ussia (2013) and solves recursively the deconvolution problem while the initial condition is continuously updated. The algorithm model is scheduled herein in figure 5.10. A

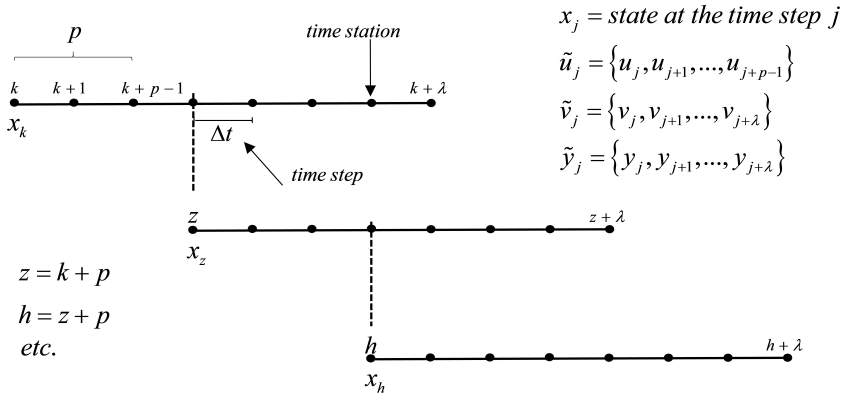

Figure 5.10: SDR algorithm

window size of $\lambda\Delta t$ slides along the time axis. At each slide, the $p-1$ first steps of the input related to the current window are obtained. The window then goes ahead exactly of p steps and so on, till the end of the signal. Referring to the figure, j is the general index used to indicate the position of the time station in the time axis, while k, z and h are effective relative positions of the time station. Note that the dimension of p respect to λ is selected so that the $p-1$ steps of the identified input are not affected by the not zero part of the kernel. In addition, after finding the first $p-1$ steps of the input, we search for the initial condition in p in order to continuously update the initial conditions.

5.6 Stability

Although existence and uniqueness conditions are ascertained, a recursive algorithm can still be unstable and lead to a divergent solution. The reason resides in the fact that any error on the solution in each window gets magnified in the next piece and the error on the state increases making the recursive solution diverges. Actually, the issues rooted in the recursion are related to the presence of noise in

the measurements and to the lack of knowledge about the initial condition. Starting from eq. 5.25 and according to the indexes in figure 5.10, the identificable part of the input is

$$\tilde{u}_k = Q_p H^{-*} \left[\tilde{y}_k - Ob_\lambda x_k \right] \tag{5.31}$$

Since there are errors in the initial conditions and noises on the measurements, the equation became

$$\tilde{u}_k + \delta\tilde{u}_k = Q_p H^{-*} \left[\tilde{y}_k - Ob_\lambda (x_k + \delta x_k) + v_k \right] \tag{5.32}$$

It is possible to isolate the portion of the identified input controlled by noise and unknown, which may generate numerical instability

$$\delta\tilde{u}_k = Q_p H^{-*} v_k - Q_p H^{-*} Ob_\lambda \delta x_k \tag{5.33}$$

As usual starting from

$$x_{k+1} = A_d x_k + B_d u_k \tag{5.34}$$

the recursion is as follow

$$x_{k+2} = A_d x_{k+1} + B_d u_{k+1} \tag{5.35}$$

$$= A_d (A_d x_k + B_d u_k) + B_d u_{k+1}$$

$$= A_d^2 x_k + A_d B_d u_k + B_d u_{k+1}$$

...

and, eventually

$$x_{k+p} = A_d^p x_k + A_d^{p-1} B_d u_k + B_d u_{k+p-1}$$

hence in a more compact form

$$x_{k+p} = A_d^p x_k + \begin{bmatrix} A_d^{p-1} B_d & A_d^{p-2} B_d & \dots & B_d \end{bmatrix} \begin{Bmatrix} u_k \\ u_{k+1} \\ \dots \\ u_{k+p-1} \end{Bmatrix} \tag{5.36}$$

Recognizing that the block row matrix is the controllability matrix in the reversed order, it writes

$$\delta x_{k+p} = A_d^p \delta x_k + Rc_{p-1} \delta \tilde{u}_k \tag{5.37}$$

We substitute eq. 5.33 into eq. 5.37 obtaining

$$\delta x_{k+p} = P_p \delta x_k + Z_p \tilde{v}_k \tag{5.38}$$

where

$$P_p = A_d^p - Rc_{p-1} Q_p H^{-*} Ob_\lambda \tag{5.39}$$

and

$$Z_p = Rc_{p-1} Q_p H^{-*} \tag{5.40}$$

In the absolute time line, the k and $k+p$ elements of the state vector advance as indicated in table 5.1, where j=1,2,3... is the number of recursions. Substituting

Table 5.1: k and $k+p$ in the time line with $p = 4$.

	k=(j-1)p+1	k+p
j=1	k=1	k=5
j=2	k=2	k=9
j=3	k=3	k=13
j=4	k=4	k=17 and so on.

the expression for k and $k+p$ in eq. 5.38, holds

$$\delta x_{jp+1} = P_p \delta x_{(j-1)p+1} + Z_p \tilde{v}_{(j-1)p+1} \tag{5.41}$$

and substituting for the first three recursions

$$j = 1,\ \delta x_5 = P_p \delta x_1 + Z_p \tilde{v}_1 \tag{5.42}$$

$$j = 2,\ \delta x_9 = P_p \delta x_5 + Z_p \tilde{v}_5$$

$$= P_p (P_p \delta x_1 + Z_p \tilde{v}_1) + Z_p \tilde{v}_5$$

$$= P_p^2 \delta x_1 + P_p Z_p \tilde{v}_1 + Z_p \tilde{v}_5$$

$$j = 3,\ \delta x_{13} = P_p \delta x_9 + Z_p \tilde{v}_9$$

$$= P_p(P_p \delta x_5 + Z_p \tilde{v}_5) + Z_p \tilde{v}_9$$

$$= P_p^3 \delta x_1 + P_p^2 Z_p \tilde{v}_1 + P_p Z_p \tilde{v}_5 + Z_p \tilde{v}_9$$

and so on. In agreement with this outcome, it is possible to write the more general formulation, i. e.

$$\delta x_{jp+1} = P_p^j \delta x_1 + \sum_{i=1}^{j} P_p^{i-1} Z_p \tilde{v}_{(j-i)p+1}, \quad j = 1, 2, 3, ... \tag{5.43}$$

Since the matrix P_p is raised to the power j corresponding to the number of recursions and that increases as the window shift along the time axis, the requirement for stability of the whole algorithm is defined on the eigenvalues of the P_p matrix,

$$\rho = ||\lambda||_{max} \leq 1 \tag{5.44}$$

The matrix P_p is function of the system matrices and of the algorithm parameters $\{p, \lambda\}$. Stability of theP_p matrix means to avoid the growth of the error on the identified input and the matrix is stable for a certain selection of p, λ and sensor position. A check on the radio of convergence based on these two important parameters is mandatory in order to ensure the numerical stability of the algorithm. It is important to note that the choice of p is related not only to the stability but also to the criticality related to the kernel of the Markov matrix.

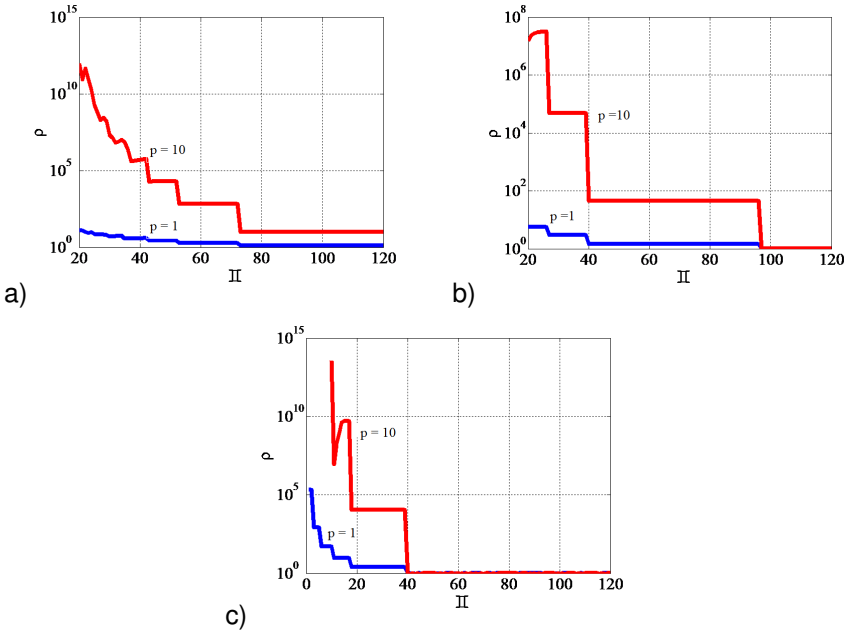

Figure 5.11: relationship between radius of convergence and parameter p.

The damping ratio is a parameter that can radically modify the identificability of the input. In the test, the rod with input in DoF #40 and output in DoF #30 with $p = 1$ and $\Delta t = 0.05$ is used. Figure 5.12 shows that for a damping ratio of 0.02 the radius of convergence swings around one for the window size greater than 40 time stations. When the damping decreases to 0.002, the radius of convergence stay still 1.011 even the size of the sliding window increases indefinitely and at the same time the curve draws back. The stability now is no more ensured since the radius of convergence is too close to one. Actually, from a mathematical point of view the convergence is reached only if the radius is less than one. However, in the case when it turns out to be more than one just because we have high machine precision, it is anyway possible to find a solution. The divergence is just outlined and it is possible to confuse it with a low frequency drift and eliminate it with a low pass filter or with other forms of regularization. By increasing the number of sensors (for example adding a sensor in DoF #35) and with a window size of 100 time station, the resultant in shown in figure 5.13 b) while figure 5.13 c) shows the filtered input. So the absence of an adequate level of damping is critical since

induce to add sensors or enlarge the sliding window dimension.

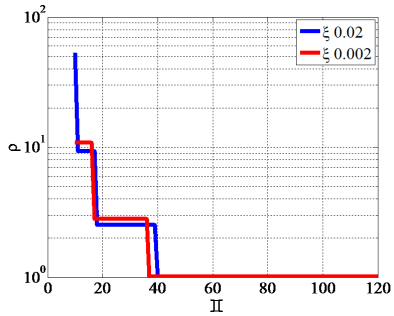

Figure 5.12: radius of convergence and damping

5.7 The Fisher information

Inferring anything from corrupted measurements necessarily reads to random variables since it is intuitive that the variance whit which one can infer depends on the level of noise on the system. The formulation of this idea in statistic is given by the Fisher Information (FI) theory. In this section, we expect to find a useful formulation for the FI in order have an accuracy measure for the inferred variables. The Fisher information is defined as,

$$FI(\theta) = E[score^2] = E\left[\left(\frac{\partial}{\partial\theta} log\ f(Y|\theta)\right)^2\right] = -E\left[\frac{\partial^2}{\partial^2\theta} log\ f(Y|\theta)\right] \tag{5.45}$$

- $log\ f(Y|\theta)$ is the logarithm of the likelihood function (that is the probability density function of Y conditioned by θ).
- The score shows how sensitively is the log of the likelihood function with respect to its parameter θ, i.e. it means that the score of the Fisher is a way to show the accuracy of the parameter estimation using noisy data.
- The Fisher information is a way of measuring the amount of information that an observable random variable Y (outputs) carries about an unknown parameter θ (inputs).
- The Fisher information is not a function of a particular observation.

In practice the likelihood function $log\ f(Y|\theta)$ is generally unknown so other quantities derived from the data are typically used to estimate $FI(\theta)$. For example, if

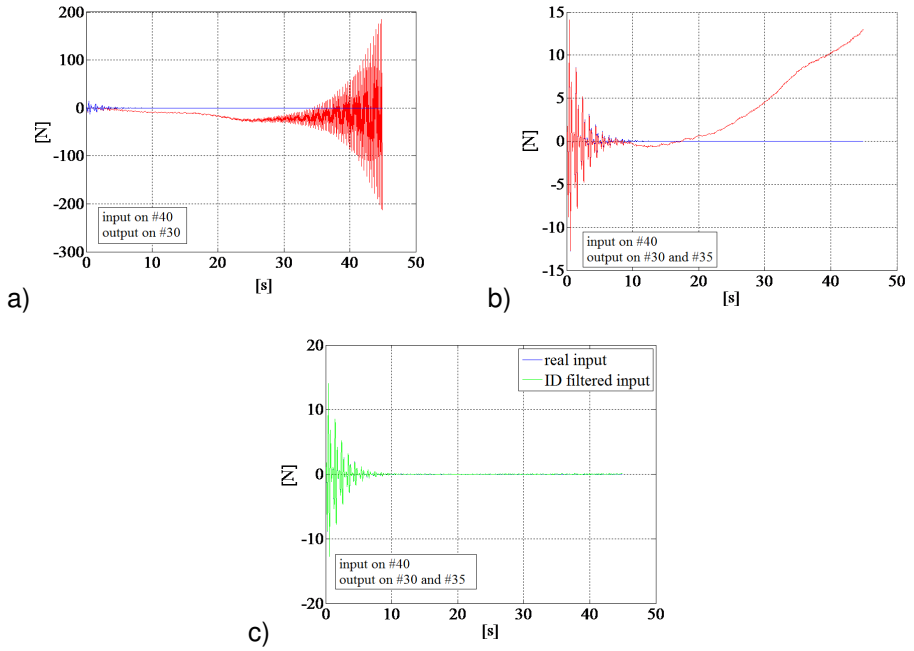

Figure 5.13: convergences problem: a) diverged solution, b) addition of a sensor, c) filtered identified input.

data Y can be used to generate a vector X whose distribution is a member of the linear exponential family having a mean $g(\theta)$ and a covariance Σ then the FI of the parameter θ contained in X can be obtained as (Van Den Bos, 2007)

$$FI(\theta) = \Im(\theta)^T \Sigma^{-1} \Im(\theta) \tag{5.46}$$

where

$$\Im(\theta) = \frac{\partial g}{\partial \theta} \tag{5.47}$$

To illustrate the significance of eq. 5.46 let the "true" value of Y be deterministically dependent on θ as depicted schematically in figure 5.14 for two cases. Let' s assume one wants to know the value of θ based on noisy values of Y. From the sketch it is evident that the statistical accuracy of θ depends on the slope of the functional relation at the location of the estimate and it is not difficult to see that the variances are related by the square of the local slope. The inverse of the Fischer information is a lower bound of any unbiased estimator of θ and it is called

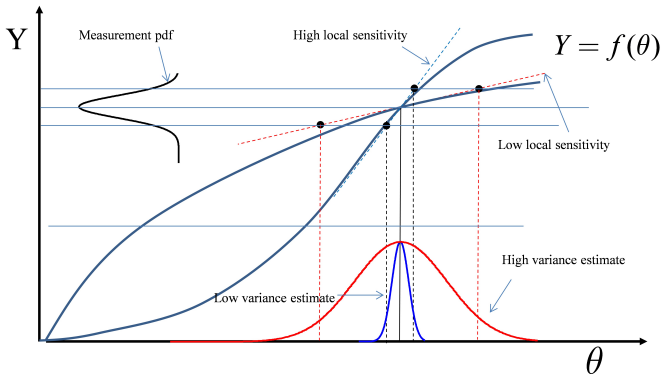

Figure 5.14: The dependence of Y on the parameter θ.

the Cramer Rao Lower Bound. The CRLB is the lower attainable variance on the reconstruction of the input.

5.8 Conditioning in the frequency domain

The problem, although well posed or stable, can be ill conditioned. The ill conditioning may be related to the physics of the problem. Usually what happens is that small changes in the observations produce a big change in the solution because of the presence of perturbation in the measurements. The effect of the ill conditioning is that there are many solution to the input identification problem that satisfy the recorded output. The classical procedure to evaluate the ill conditioning is through the conditioning number. The conditioning number is the ratio between the maximum and minimum singular value of the matrix (obviously excluding the zero singular values). A high CN is related to the ill conditioning of the solution.

$$SV = \begin{bmatrix} \# & & & \\ & \# & & \\ & & \# & \\ & & & \sim 0 \end{bmatrix}, \quad \frac{S_{max}}{S_{min}} \begin{cases} big & \rightarrow well\ cond \\ small & \rightarrow ill\ cond \end{cases} \tag{5.48}$$

Moreover, the ill-conditioning of the generalized solution depends on the number of data points and, in general, it increases by increasing this number. Indeed, in the frequency domain, the longer the time range, the bigger is the noise variance in the output available data. When the conditioning is inspected in the frequency domain the premise is that the variable are observed over all time. We want to ob-

tain information about conditioning by inspection of the Cramer Rao Lower Bound. Recalling that the Fisher information is,

$$FI(\theta) = \frac{\partial g^T(\theta)}{\partial \theta} \sum -1 \frac{\partial g(\theta)}{\partial \theta} \tag{5.49}$$

If the model for the observations is $g(\theta)$ and θ is the set of parameters, the derivative is simply the transfer function of the system in the z-domain,

$$\frac{dy(z)}{du(z)} = G(z) \tag{5.50}$$

where

$$F(z) = \frac{1}{\sigma_v^2} G^T(z) G(z) \tag{5.51}$$

And the minimum variance attainable is the Cramer Rao Lower Bound,

$$CRLB(z) = \sigma^2 \left(G^T(z) G(z) \right)^{-1} \tag{5.52}$$

The Cramer Rao Lower Bound is the minimum attainable covariance of an unbiased estimator. To show some the issues related to the ill conditioning in the frequency domain, let's take the 40-DoF rod. Figure 5.15 a) represent the CRLB for not collocated measurements, in particular the inputs are on the 5^{th} and 40^{th} DoF and the outputs are located on the 1^{st}, 10^{th} and 30^{th} DoF. Part b) of the same figure shows the collocated case, with inputs on the 10^{th} and 40^{th} DoF and outputs in the same positions. Both the plot include information about displacement, velocity or acceleration measurements. What it should be noted is that the ill conditioning increases quickly for frequencies that are outside the system bandwidth. High frequency disturbances arises almost always except for collocated measurements of velocity. So the final conclusion is that the Δt must be such that the realizations of the measurements noise are restricted to the bandwidth of the system or, in other words $\Delta t \geq 0.5 B_W$. Let's see the example in figures 5.16 and 5.17 where the case of non collocated measurements of both accelerations and displacements are analyzed. Figure 5.16 are referred to the rod with a stable solution after 11 and 6 steps in the case of the sampling time of 0.02 s and 0.05 s, respectively, and with acceleration sensors. The 50 Hz sampling generates in the identified input an high frequency disturbance that can be assimilated to the ill conditioning and that totally

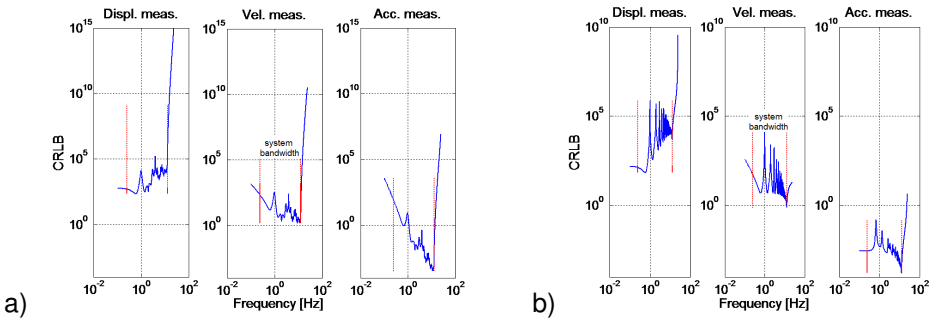

Figure 5.15: the CRLB for a) not collocated; and b) collocated measurements.

distort the identified signal. On the other hand, using the sampling frequency of 20 Hz, there is a low frequency conditioning that shows through a low frequency drift. Figure 5.17 are referred to the rod with stable solution after 18 and 7 steps and with displacement sensors. Displacement measurements manifest only the high frequency ill conditioning, so the 20 Hz sampling seems to be a good solution.

5.9 Conditioning in the time domain

An exact expression for the error in the p-inputs at the $jp+1$ time station can be obtained by substituting eq. 5.43 into eq. 5.33. After some tedious, albeit elementary tracking of indices, one gets

$$\delta\tilde{u}_{j\cdot p+1} = -Q_p H^{-*} Ob_\lambda P_p^j \delta x_1 + \sum_{i=0}^{j} D_i \tilde{v}_{(j-i)p+1} \tag{5.53}$$

where

$$D_i = -Q_p H^{-*} Ob_\lambda P_p^{i-1} Z_p \tag{5.54}$$

and

$$D_0 = Q_p H^{-*} \tag{5.55}$$

with $D_i \in \mathbb{R}^{(pr)x((\lambda+1)m)}$. To simplify we focus on the situation where the window advances one time station at a time, so $p = 1$. In this case the vector in eq. 5.53 contains the input vector only at the $j+1$ time station. Letting q be the number of the input in the input vector, then with a_q as the q^{th} row of the matrix that pre-multiplies the error in the initial state and b_q as the concatenation of all the q^{th} rows of the

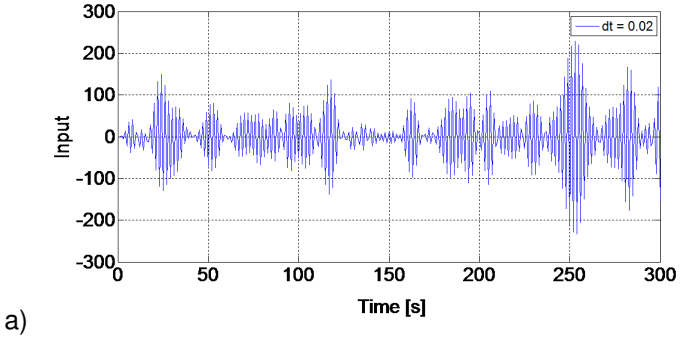

a)

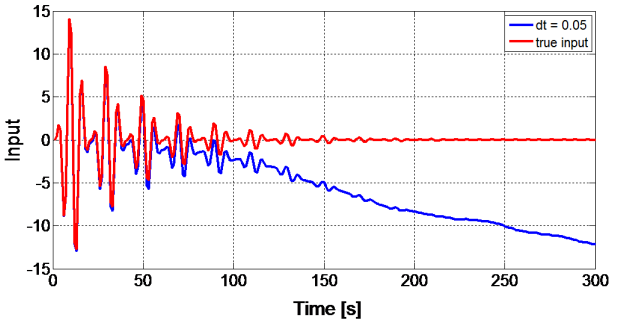

b)

Figure 5.16: example of bad conditioning in the frequency domain.

matrices D_i, one has

$$\delta u_{j+1}^{(q)} = a_q^T \delta x_1 + b_q^T V \tag{5.56}$$

where $a_q \in \mathbb{R}^{1\,x\,2n,}$, $b_q \in \mathbb{R}^{1\,x\,(j+1)(\lambda+1)m}$ and $V \in \mathbb{R}^{(j+1)(\lambda+1)m\,x\,\ell}$ is the concatenation of all the noise sequences $\tilde{v}_{(j-i)+1}$. Note that the vector V is not strictly random since its length is ,$(\lambda+1)m(j+1)$ while there are only $(j+\lambda)m$ independent noise entries. To aid in clarity with regards to the indices Appendix B presents an illustration in a specific scenario. Assuming that the first term in eq. 5.56 can be neglected for sufficiently large j (or for any j if the error in the initial state is negligible) one has

$$\delta u_{j+1}^{(q)} \cong b_q^T V \tag{5.57}$$

b_q is the concatenation of the rows of the D_i matrices and is nothing else that the index of the ill conditioning in the time domain. If b_1 is not increasing, then adequate performance are guaranteed as shown in figure 5.18.

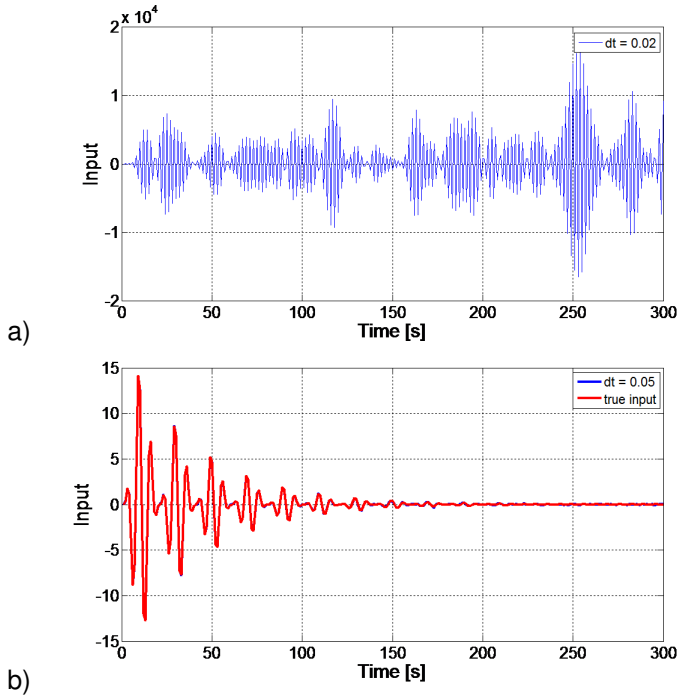

Figure 5.17: example of good conditioning in the frequency domain.

5.10 Singular Values Truncation

Assuming the following definition of the estimated input, i.e.

$$u_p = QH^{-*}y - QH^{-*}Ob\,x_0 \tag{5.58}$$

It is possible to sum up the general effects of noise as,

$$u_p = QH^{-*}(y + v) \tag{5.59}$$

The expectation is that

$$H^{-*}y \gg H^{-*}v \tag{5.60}$$

$$\frac{1}{s_{max}}||\bar{y}|| \gg \frac{1}{s_{min}}||noise|| \tag{5.61}$$

To decide on the singular value cutoff let the maximum and the minimum singular values of S_1 be s_{max} and s_{min}. The worst scenario is having the signal parallel to

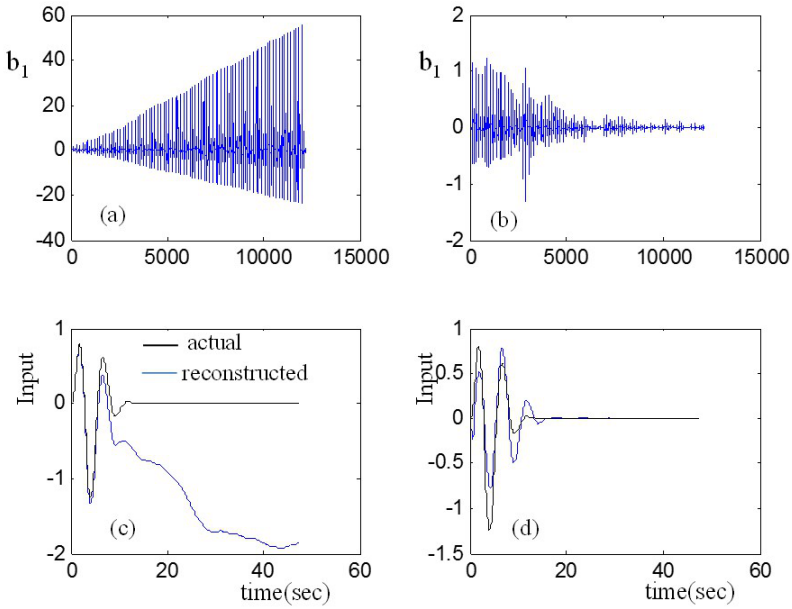

Figure 5.18: example of ill conditioning in the time domain.

the first singular vector and the noise parallel to the last. The ratio of the amplified (de-amplified) vector norms is thus

$$\frac{1}{s_{max}}||\bar{y}|| = \frac{1}{\beta}\frac{1}{s_{min}}||noise|| \tag{5.62}$$

$$\frac{||noise||}{||\bar{y}||}\frac{s_{max}}{s_{min}} = \beta \tag{5.63}$$

from where it follows that a possible criterion for singular value truncation is

$$\frac{s_{min}}{s_{max}} = \frac{NSR}{\beta} \tag{5.64}$$

Regularization produces effect on both stability and conditioning. As shown in figures 5.19 and , the stability limit decreases if truncation is performed. In addition, the un-regularized solution shows an increase in the standard deviation of the estimation error as presented in figure 5.20 a) and b).

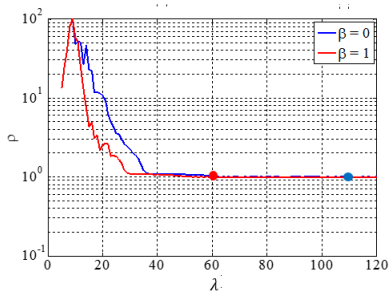

Figure 5.19: effect of regularization on stability.

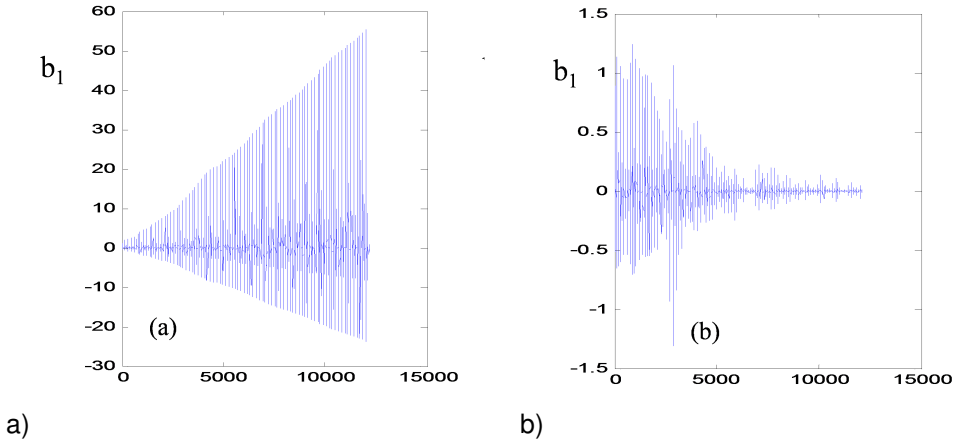

a) b)

Figure 5.20: effect of regularization on conditioning in time domain.

5.11 Experimental test

This experiment was conducted at the Department of Civil and Environmental Engineering of the Northeastern University at the Structural Dynamics and System Identification Lab. The structure is an aluminum beam fixed at one end as shown in Figure 4. The shaker originates a burst pseudo-random input with a whole duration of 6.5 s in position #6 and the measurement set up includes 3 accelerometers PCB, as shown in figure 5.21. The sampling frequency is 1280 Hz and a 7 DoF model is used are used to discretize the structure. The modal frequencies are obtained from the model and they are 13, 83, 239, 467, 726, 1016, 1350 Hz.

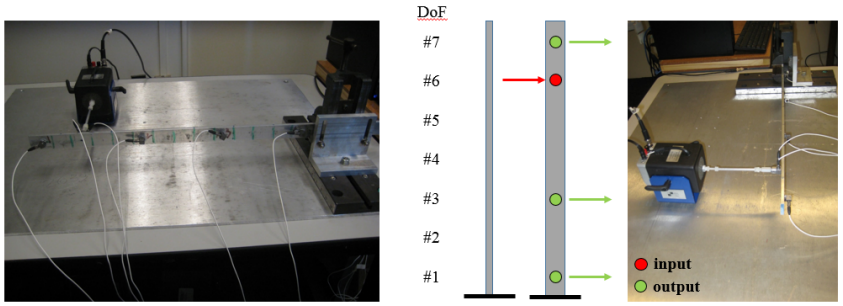

Figure 5.21: the set-up of the experimental test on the beam.

5.11.1 Tests on number and position

Data collected from the test provided information about both the number and position of the actual input. Figure 5.22 a) shows the singular values along the frequency line of the matrix and as consequence, it is possible to infer that the number of independent acting load is just one. Figure 5.22 b) shows then that right input position is the one on 6th DoF.

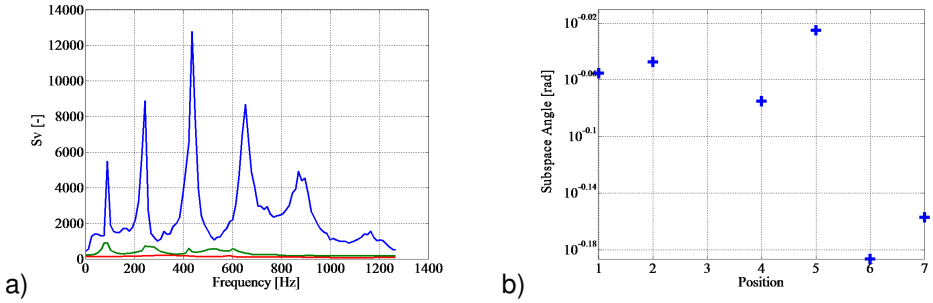

Figure 5.22: number and position of independent inputs acting on the beam.

5.11.2 Tests on the time histories

The SDR algorithm is stable for $\lambda > 10$ steps, the sampling frequency is f_C=1280 Hz and the band is B_W=13 Hz-1350 Hz. Even if the high frequency conditioning is avoided but we still have low frequency drift so the error due to the noise increases with time and it is related to the low frequency ill conditioning. The input at coordinate #6 is reconstructed and compared with the actual values in fig-

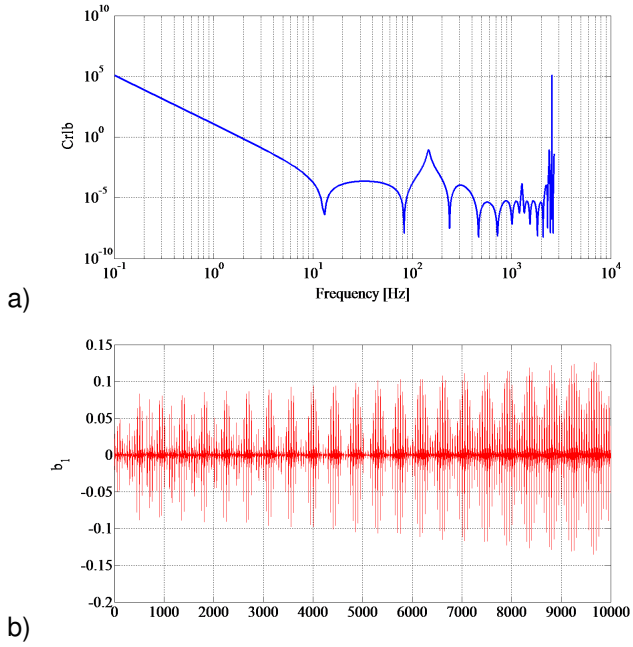

Figure 5.23: conditioning in a) frequency; and b) time domain in the experimental test.

ure 5.24. The reconstruction in not exact because 0.5% NSR was added to the measurements.

5.12 Conclusions

The Chapter addressed the determination of both number and position, and time histories of unmeasured inputs. In the time domain, the general solution of the inverse problem is simply obtained from the deconvolution of the impulse response from the output measurements. However, the deconvolution must be constrained by the true physics of the problem in order to avoid the formulation of ill-posed problems. In fact, the I/O arrangement and the inherent delay of the problem define if the input is identifiable or if it is identifiable on any subspace. It should be noted that FD models are made up of the sum of a series with finite terms. In this respect, finite element discretization of a continuum does not have impulse response functions with zero finite time segments. So the part of the impulse response functions that are zero in the continuum are very small in the model and

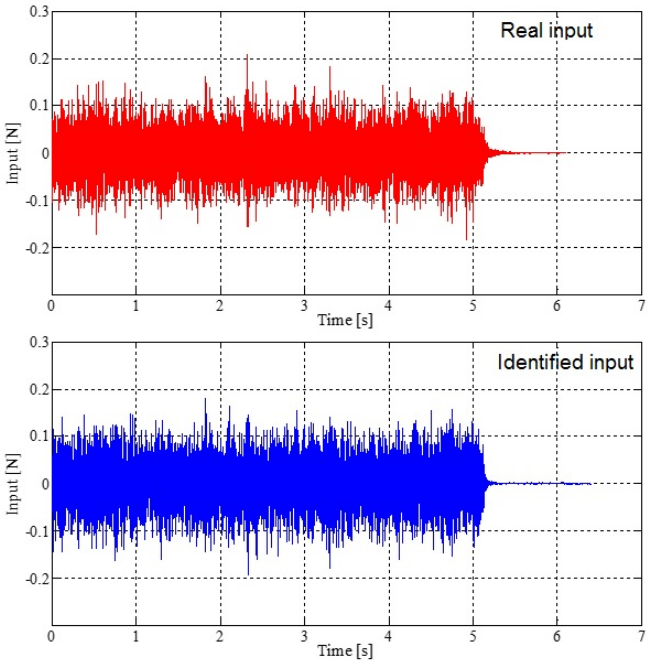

Figure 5.24: comparison between the actual and the predicted input.

have no consequence in the solution of forward problems but can bring to huge mistakes in the solution of the inverse problem. In this respect, it can be shown that the part of the input affected by the delay is strictly related and can be detected through inspection of the Toeplitz matrix kernel. In a first phase the number and the position of the unknown input is addressed. The chapter explains that the number of inputs can be determined in a batch mode and with reasonable accuracy from the effective rank of a matrix formed using the Fourier transform of the output signals. The position of the acting loads is subsequently established by inspecting the generalized angles made by the columns of the transfer matrix of the model with the basis identified from the data. Once the input mapping is complete the time history of the load can be inferred with good accuracy using a sequential deconvolution algorithm. The sequential deconvolution is an iterative method that takes into account for the inherent delay of the system. For this purpose, the kernel is fundamental for the comprehension of constraints and limitations on the input reconstruction especially if the input reconstruction has to be solved in the recursive

fashion. The kernel makes clear which part of the solution is affected by the delay and consequently if the I-O arrangement leads to the knowledge of inputs over the whole time range of outputs or just on a subset of the axis time. The size of the recursion window and the prediction lag have to be chosen carefully because they affects the stability of the algorithm. Stability conditions are derived and result to be function of the size of the forward shift, the observability, the Toeplitz matrix and the state transition matrix. The ill conditioning conditions are investigated as well as the conditioning in time and frequency domain in order to analyze the solution accuracy. In this respect the error in the estimated inputs is a function of both the noise and the error in the initial condition and as a consequence an index of ill conditioning in time domain is derived. In frequency domain, the CRLB is a tool to select the step for time discretization in order to limit the ill conditioning of the solution. Both numerical and experimental tests have been performed with good results.

5.13 Appendix A - Dead Time in Finite Dimensional Systems Impulse Response Functions

This appendix presents a proof showing that the impulse response functions of FD systems have no dead time. We begin by developing an expression for the impulse response and then present the proof (Bernal and Ussia, 2013). The input to state and state to output description of an arbitrarily damped linear system with an excitation at coordinate "s" and a measurement at a spatially separated location "z" is,

$$\begin{aligned} \dot{x} &= Ax + Bf_s \\ y_z &= Cx \end{aligned} \tag{5.65}$$

Taking f_s as an impulse $\delta(t)$, y_z is rendered the impulse response h_z, and one can thus write

$$\begin{aligned} \dot{x} &= Ax + B\delta(t) \\ h_z &= Cx \end{aligned} \tag{5.66}$$

The Jordan decomposition of A is $\Phi^T \Lambda \Phi$ and thus taking $x = \Phi Y$ gives

$$\begin{aligned} \dot{Y} &= \Lambda x + \Gamma\delta(t) \\ h_z &= \Psi x \end{aligned} \tag{5.67}$$

where $\Gamma = \Phi Y$ and $\Psi = C\Phi$. Accepting that A is not defective $\Lambda = diag(\lambda_j)$, then the solution for the j^{th} term of eq. 5.67 writes

$$Y_j(t) = Y_{0,j} e^{\lambda_j t} \tag{5.68}$$

where the initial condition of the generalized coordinate is obtained by noting that from eq. 5.66 one has

$$\int_0^{\epsilon} \dot{x} dt = A \int_0^{\epsilon} x dt + B \int_0^{\epsilon} \delta(t) dt \tag{5.69}$$

and thus given the definition of the impulse, for $\epsilon \to 0$, $x_0 = B$. So it yields that $Y_0 = \Phi^{-1} B$ and substituting eq.5.68 into eq. 5.67 gives

$$h_z = \sum_{j=1}^{N} c_j e^{\lambda_j t} \tag{5.70}$$

where $c_j = \varphi_j Y_{0,j}$, $\Psi = \{\varphi_1, ..., ...\varphi_N\}$ and N is the system order.

- Preposition: the function $h_z = \sum_{j=1}^{N} c_j e^{\lambda_j t}$ is is not zero for any time segment of finite extent.

- Proof: let the time segment be some arbitrary span $[t_1, t_2]$, if the impulse is to be zero over this segment then

$$\sum_{j=1}^{N} c_j e^{\lambda_j t} = 0, \ t_1 \leq t \leq t_2 \tag{5.71}$$

If any of the c_j terms are zero they fall out of the series so, for generality we write

$$\sum_{j=1}^{N_1} c_j e^{\lambda_j t} = 0, \ t_1 \leq t \leq t_2 \tag{5.72}$$

where $N_1 \leq N$. There is also the possibility that there are some zero eigenvalues, letting the number of zero eigenvalues as $q \geq 0$ and placing them as the last entries in the series one has

$$\sum_{j=1}^{N_1 - q} c_j e^{\lambda_j t} = P, \ t_1 \leq t \leq t_2 \tag{5.73}$$

where we now have $\lambda_j \neq 0$ and $P = -\sum_{j=N_1+1-q}^{N_1} c_j$. Differentiating eq. 5.73 gives

$$\sum_{j=1}^{N_1-q} c_j \lambda_j e^{\lambda_j t} = 0,\ t_1 \leq t \leq t_2 \tag{5.74}$$

from where it follows that

$$e^{\lambda_1 t} = \sum_{j=2}^{N_1-q} \bar{c}_j e^{\lambda_j t} \tag{5.75}$$

where $\bar{c}_j = -\dfrac{c_j \lambda_j}{c_1 \lambda_1}$. Substituting 5.75 into 5.73 one has

$$\sum_{j=2}^{N_1-q} \bar{c}_j e^{\lambda_j t} = P,\ t_1 \leq t \leq t_2 \tag{5.76}$$

where one can easily confirm that $\bar{c}_j = (c_1 \bar{c}_j + c_j)$. Since eq. 5.76 is exactly the same as A.13 the procedure carried out to eliminate the first term of the series can be repeated until there is a single term left and one has 5.73

$$\sum_{j=N_1-q}^{N_1-q} \hat{c}_j e^{\lambda_j t} = P,\ t_1 \leq t \leq t_2 \tag{5.77}$$

where $\hat{c}_j$ is some constant. A necessary condition for eq. 5.77 to be satisfied is that the eigenvalue $\lambda_j = 0$ and since none of the eigenvalues in the series are zero one concludes that eq. 5.77 is a contradiction and it thus follows that the initial premise, i.e., that the impulse response was zero over the time interval selected, is not possible – concluding the proof.

5.14 Appendix B - Illustration of Vectors in 5.9

Suppose that we want to characterize the error at $t = 2\Delta t$ so in eq. 5.53 we have $j = 2$, and the equation writes

$$\delta \tilde{u}_3 = -Q_p H^{-*} Ob_\lambda P_p^2 \delta x_1 + D_0 \bar{v}_3 + D_1 \bar{v}_2 + D_2 \bar{v}_1 \tag{5.78}$$

For $r = 2$, $\lambda = 3$ and $m = 3$, one has

$$\begin{bmatrix} \delta u_3^{(1)} \\ \delta u_3^{(2)} \end{bmatrix} = \begin{bmatrix} row\,\#1 \\ row\,\#2 \end{bmatrix} \{\delta x_1\} + \begin{bmatrix} row\,\#1 \\ row\,\#2 \end{bmatrix}_{D_0} \bar{v}_3 + \begin{bmatrix} row\,\#1 \\ row\,\#2 \end{bmatrix}_{D_1} \bar{v}_2 + \begin{bmatrix} row\,\#1 \\ row\,\#2 \end{bmatrix}_{D_2} \bar{v}_1$$

(5.79)

The rearrangement of eq. gives

$$\delta u_3^{(1)} = \left[\; row\,\#1 \; \right] \{\delta x_1\} + \left[\; row\,\#1|_{D_0} \quad row\,\#1|_{D_1} \quad row\,\#1|_{D_2} \; \right] \begin{bmatrix} \tilde{v}_3 \\ \tilde{v}_2 \\ \tilde{v}_1 \end{bmatrix} \tag{5.80}$$

$$\delta u_3^{(2)} = \left[\; row\,\#2 \; \right] \{\delta x_1\} + \left[\; row\,\#2|_{D_0} \quad row\,\#2|_{D_1} \quad row\,\#2|_{D_2} \; \right] \begin{bmatrix} \tilde{v}_3 \\ \tilde{v}_2 \\ \tilde{v}_1 \end{bmatrix} \tag{5.81}$$

The b_q^T vectors are

$$b_1^T = \left[\; row\,\#1|_{D_0} \quad row\,\#1|_{D_1} \quad row\,\#1|_{D_2} \; \right] \tag{5.82}$$

$$b_2^T = \left[\; row\,\#2|_{D_0} \quad row\,\#2|_{D_1} \quad row\,\#2|_{D_2} \; \right] \tag{5.83}$$

and the vector $V \in \mathbb{R}^{(j+1)\lambda m \, x \, 1}$ that is the concatenation of all the noise sequences $\tilde{v}_{(j-i)+1}$, is now

$$V = \begin{bmatrix} \tilde{v}_3 \\ \tilde{v}_2 \\ \tilde{v}_1 \end{bmatrix} \tag{5.84}$$

where

$$\begin{aligned}
\tilde{v}_3 &= \begin{bmatrix} v_3^{(1)} & v_3^{(2)} & v_3^{(3)} & v_4^{(1)} & v_4^{(2)} & v_4^{(3)} & v_5^{(1)} & v_5^{(2)} & v_5^{(3)} & v_6^{(1)} & v_6^{(2)} & v_6^{(3)} \\ & v_7^{(1)} & v_7^{(2)} & v_7^{(3)} & & & & & & & & & \end{bmatrix}^T \\
\tilde{v}_2 &= \begin{bmatrix} v_2^{(1)} & v_2^{(2)} & v_2^{(3)} & v_3^{(1)} & v_3^{(2)} & v_3^{(3)} & v_4^{(1)} & v_4^{(2)} & v_4^{(3)} & v_5^{(1)} & v_5^{(2)} & v_5^{(3)} \\ & v_6^{(1)} & v_6^{(2)} & v_6^{(3)} & & & & & & & & & \end{bmatrix}^T \\
\tilde{v}_1 &= \begin{bmatrix} v_1^{(1)} & v_1^{(2)} & v_1^{(3)} & v_2^{(1)} & v_2^{(2)} & v_2^{(3)} & v_3^{(1)} & v_3^{(2)} & v_3^{(3)} & v_4^{(1)} & v_4^{(2)} & v_4^{(3)} \\ & v_5^{(1)} & v_5^{(2)} & v_5^{(3)} & & & & & & & & & \end{bmatrix}^T
\end{aligned} \tag{5.85}$$

CHAPTER 6

MODELING AND SEMI-ACTIVE CONTROL OF A MAGNETO-RHEOLOGICAL TUNED MASS DAMPER

6.1 Introduction

This chapter deals with the identification and control of a non-linear adaptive rotational Magneto-Rheological (MR) damper produced by Maurer Söhne Gmbh and used in a Magneto-Rheological Tuned Mass Damper (MR-TMD) installed on the Nomi-Calliano footbridge. The chapter consists in three parts involving modeling and identification of the hysteretic damper and the control of the semi-active TMD.

The first macro part treats about the theory related to modeling of hysteretic systems. The discussion is then divided between a panoramic on the classical models used in the literature to describe hysteresis cycles and a more detailed presentation related to MR fluids. In this respect, non-linear models for general hysteretic systems are first presented with fundamental definitions and mathematical issues and, eventually, a review on main modification to the original Bouc-Wen model is reported. Then, in more detail, non-linear models used in the current literature specific for MR fluids are briefly described (Bouc-Wen based models, Hyperbolic tangent, Dahl, LuGree and non-parametric models).

The second macro part involves aspects related to the parametric identification of the non-linear hysteretic damper used on the Nomi-Calliano footbridge. In detail, the investigation is directed to the identification of an accurate parametric model of the MR damper being part of the semi-active TMD. Since, many control strategies are known as model based, a focus on the nature of the MR fluid and eventually

on the damper dynamics is needed in order to identify both main properties and a detailed analytical model. Tests on the MR damper were conducted at the Materials and Structural Testing Laboratory of the University of Trento and the Test Rig 1 -TT1- was used. The TT1 is a dynamic system developed by the Department of Civil, Mechanical and Environmental Engineering of the University of Trento being part of the project SERIES and now used for the experimental tests on the damper. The identification of the model parameters is obtained using a non-linear constrained optimization tool. In addition, a wide part of this second part is dedicated to the study of the Unscented Kalman Filter (UKF) as a tool for identification of non-linear models. Numerical tests on several classical models of hysteresis such as Bouc-Wen, Baber-Wen, Baber-Noori and Foliente model are performed. Moreover a final experimental test was performed using a set of time-invariant experimental data recorded from the damper positioned on the TT1 test rig. The final outcome of the model identification was a model based on the Bouc-Wen model validated at the end of the test campaign by means of experimental data.

Finally, the third part regards the semi-active control of the MR TMD installed on the footbridge. In this respect, a semi-active control strategy known as clipped-optimal control law was numerically simulated. Simulations also involved some real data recorded from the actual structure by means of the installed permanent monitoring system. Since the analysis involved just the third critical mode, actual data, provided by accelerations in 8 points of the bridge, were projected in the modal domain. After the projection, a modal load has been detected through the input identification tool presented in Chapter 5. The reconstructed input was then applied on the simplified 2DoF model outlined by the Den Hartog theory and used in the validation of the controller. Eventually, the experimental set-up of the control system and the positioning on the footbridge of the device is described and performed.

6.2 Non-linear models for hysteretic systems

Hysteresis is a mechanical phenomenon that supplies restoring force against movement and dissipates energy. The input-output relations between variables involves memory effect since restoring force depends not only by the instantaneous deformation but also on the whole history of deformation. In addition, when the

input displacement is periodic, the restoring force appears to be asymptotically periodic too, with the same period. The hysteresis loop is the result of the force-displacement plot and the parameters characterizing the model define of course the loop shape. In the following section we describe the classical Bouc, the Wen, the Bouc-Wen and other Bouc-Wen type models.

6.2.1 The Bouc model

The dynamic equation of a SDoF system in presence of the restoring force governed by the Bouc model proposed in Bouc (1966, 1971) can be written as,

$$\begin{cases} m\ddot{u}(t) + c\dot{u}(t) + ku(t) + z(t) = d(t) \\ \dot{z}(t) = [A - \beta z sign(\dot{u}(t))]\dot{u}(t) \end{cases} \tag{6.1}$$

where $d(t)$ is the external load and A, $\beta > 0$. From a mechanical point of view, the term $z(t)$ is the component that depends from the velocity time history $\dot{u}(t)$. Then a modification (Bouc, 1966) of the original model was proposed in order to better modeling the hysteresis loop shape in particular the unloading branches,

$$\begin{cases} m\ddot{u}(t) + c\dot{u}(t) + ku(t) + z(t) = d(t) \\ \dot{z}(t) = [A - \beta z sign(\dot{u}(t)) - \gamma|z(t)|]\dot{u}(t) \end{cases} \tag{6.2}$$

where A, $\beta > 0$ and $\gamma < \beta$.

6.2.2 The Wen model

Wen (1980) introduced an additional modification related to the issue of the post yielding stiffness. The motion of an oscillator with non-linear stiffness is described in the following form of the Newton's second law,

$$m\ddot{u}(t) + f(\dot{u}(t), u(t)) = d(t) \tag{6.3}$$

By introducing the parameter α which defines the post to pre-yielding stiffness ratio, the restoring force results,

$$f(t) = \alpha ku(t) + (1 - \alpha)kz(t) \tag{6.4}$$

where k is the initial total stiffness. So the new Wen model results to be,

$$\begin{cases} m\ddot{u}(t) + c\dot{u}(t) + \alpha ku(t) + z(t) = d(t) \\ \dot{z}(t) = \left\{(1 - \alpha)k[A - |z(t)|^n(\gamma + \beta sign(z(t)\dot{u}(t))]\right\}\dot{u}(t) \end{cases} \tag{6.5}$$

6.2.3 The Bouc-Wen model

Wen (1976) introduced a modification to the Bouc model. The model is described by the following second order non-linear dynamic differential equation,

$$\begin{cases} m\ddot{u}(t) + c\dot{u}(t) + ku(t) + z(t) = d(t) \\ \dot{z}(t) = A\dot{u}(t) - \beta\dot{u}(t)|z(t)|^n - \gamma|\dot{u}(t)|z(t)|z(t)|^{n-1} \end{cases} \tag{6.6}$$

also written as

$$\begin{cases} m\ddot{u}(t) + c\dot{u}(t) + ku(t) + z(t) = d(t) \\ \dot{z}(t) = [A - |z(t)|^n(\gamma + \beta sign(z(t)\dot{u}(t))]\dot{u}(t) \end{cases} \tag{6.7}$$

A, β, γ and n are the hysteresis parameters that define the shape of the hysteresis cycle where A is the oscillator stiffness, $\beta > 0$, $-\beta < \gamma < +\beta$ and $n > 0$, respectively. Modifications into the relationship between these parameters modify the behavior of the cycle inducing softening or hardening effects as reported in table 6.1 (Baber and Wen, 1980). In addition figure 6.1 shows how the parameter n influences the shape of the cycle. Properties related to the physical consistency

Table 6.1: relationship between β and γ and their effects on hysteresis

$\beta + \gamma > 0$ $\gamma - \beta > 0$	Weak softening
$\beta + \gamma > 0$ $\gamma - \beta = 0$	Weak softening on loading, mostly linear unloading
$\beta + \gamma > \beta - \gamma$ $\gamma - \beta < 0$	Strong softening loading and unloading, narrow hysteresis
$\beta + \gamma = 0$ $\gamma - \beta < 0$	Weak hardening
$\beta + \gamma < 0$ $\beta + \gamma > \gamma - \beta$	Strong hardening

of the model are listed below (Ismail et al., 2009):

- BIBO stability: for any bounded input, the output of the true hysteresis in bounded since the treated system are stable and in open loop.

- Consistency with the asymptotic motion of the physical system.
- Passivity is related to the energy dissipation: the system does not generate energy and the model is passive respect to a storage function W.
- Thermodynamic admissibility is verified when a model fulfill the second principle of the Thermodynamics; in the case of the Bouc-Wen model it happens if $n > 0$, $\beta > 0$ and $-\beta \leq \gamma \leq \beta$ hold.
- Accordance with the Drucker's postulate implies that the system should not produce negative energy dissipation when the unloading-reloading process occurs without the load reversion. The Bouc-Wen model violates this postulate and attempts to reduce this violation have been done (Carli, 1999; Casciati, 1988, 1989; Dominiquez et al., 2008).

We are in presence of a black-box approach that means what follows: given a set of experimental input-output data, one searches for the set of parameters of a model which could match the available data and the match is good enough such that the error between numerical and experimental results is small. In any case, the model requires physical and mathematical consistency. Mathematical consistency on the other hand consists in the existence and uniqueness of the solution and also in the uniqueness of the description of the model; the last issue is related to the fact that the parameters of the model are redundant since there exists an infinite number of parameter set the lead to the same input-output shape. The modeling of an hysteretic system using the above-mentioned laws is an arduous task and sometimes alternative model combining physical understanding of the hysteretic behavior and some kind of black box modeling have been proposed.

6.2.4 The Baber-Wen model

The Baber Wen model takes into account for both the stiffness and strength degradation effects on the hysteresis cycle (Baber and Wen, 1981, 1980).

$$\begin{cases} m\ddot{u}(t) + c\dot{u}(t) + \alpha k u(t) + z(t) = d(t) \\ \dot{z}(t) = \left\{ \frac{(1-\alpha)}{\eta} [A - \nu |z(t)|^n (\gamma + \beta sign(z(t)\dot{u}(t))] \right\} \dot{u}(t) \\ \dot{e}(t) = z(t)\dot{u}(t) \end{cases} \tag{6.8}$$

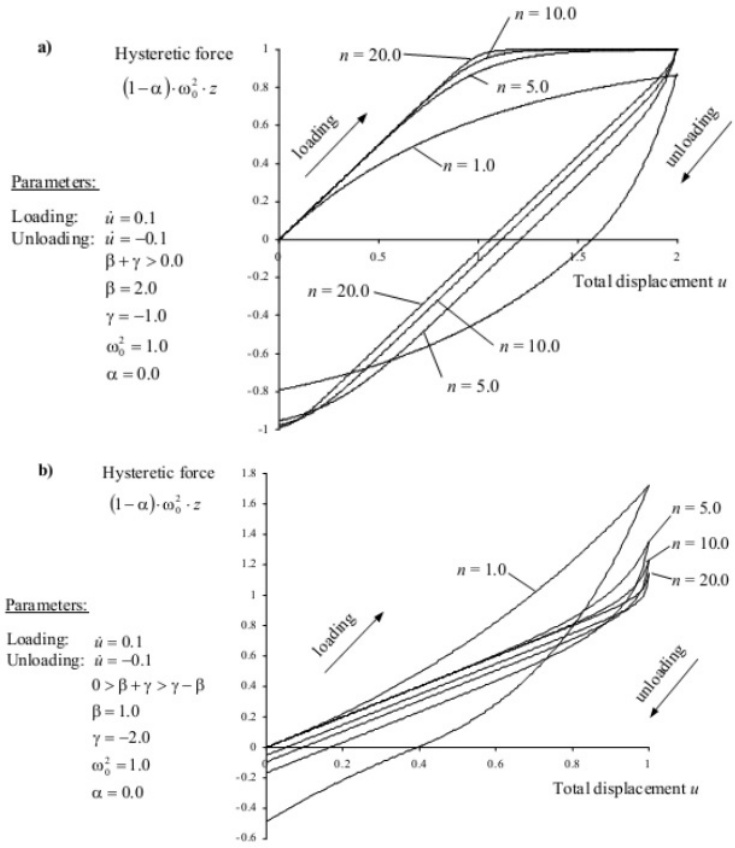

Figure 6.1: increasing effect of the parameter *n* on: a) softening; and b) hardening hysteresis model (Heine, 2001).

with

$$\nu = \nu(e) = \nu_0 + \delta_\nu e \tag{6.9}$$

$$\eta = \eta(e) = \eta_0 + \delta_\eta e \tag{6.10}$$

$$A = A(e) = A_0 - \delta_A e \tag{6.11}$$

where, as usual, A, β, γ, n and α, k, A_0 are the hysteresis parameters, while δ_A, δ_ν, δ_η, $\nu_0$and η_0 are the degradation parameters. In details,

- α is the ratio between the post yielding and the initial stiffness of the system already introduced in Wen (1980).
- $k = m\omega_0^2$
- $c = 2\xi_0\omega_0 m$
- $e = \int_0^t z\dot{u}dt$ is the total energy dissipated by the cycle
- ν and η are the controlling parameters for strength and stiffness degradation, respectively and have energy dependent evolution.

6.2.5 The Baber-Noori model

The model introduced by Baber and Noori (1986) gives a good approximation of hysteresis systems with degrading and pinching phenomena. The final result of Baber and Noori's work is the following model,

$$\begin{cases} m\ddot{u}(t) + c\dot{u}(t) + \alpha k u(t) + z(t) = d(t) \\ \dot{z}(t) = \left\{ \frac{(1-\alpha)h}{\eta} [A - \nu|z(t)|^n(\gamma + \beta sign(z(t)\dot{u}(t))] \right\} \dot{u}(t) \\ \dot{e}(t) = z(t)\dot{u}(t) \end{cases} \tag{6.12}$$

as in the previous model A, v and η are linearly varying functions of the element total energy dissipation,

$$A = A(e) = A_0 - \delta_A e \tag{6.13}$$

$$\nu = \nu(e) = \nu_0 + \delta_\nu e \tag{6.14}$$

$$\eta = \eta(e) = \eta_0 + \delta_\eta e \tag{6.15}$$

while the pinching is modeled through a specific function $h(z, e)$,

$$h = h(z, e) = 1 - \zeta_1 e^{\left(-\frac{z^2}{2\zeta_2^2}\right)} \tag{6.16}$$

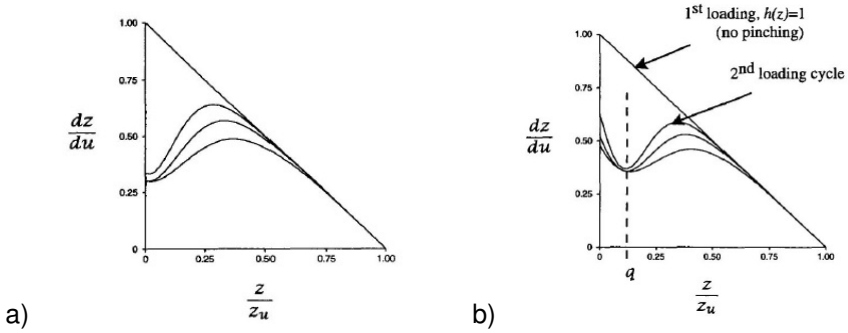

Figure 6.2: pinching function for: a) the Baber-Noori and b) Foliente model (Foliente, 1995).

whose behavior is shown in figure 6.2 a). The function h is Gaussian (zero mean) and with values into the range $[0, 1]$; when the pinching is maximum $z = 0$ and $h \sim 0$. Other parameters are summarized in the following,

$$\zeta_1 = \zeta_1(e) = \zeta_{1,0}(1 - e^{-pe}) \tag{6.17}$$

$$\zeta_2 = \zeta_2(e) = (\xi_0 + \delta_\xi)(\lambda + \zeta_1) \tag{6.18}$$

where p, $\zeta_{1,0}$, ξ_0, δ_ξ, and λ are constant parameters that define the shape and the entity of the pinching effect. In particular,

- $\zeta_1 \in [0, 1]$ controls the pinching;
- $\zeta_{1,0}$ is the maximum value of ζ_1;
- p controls the rate of changing of ζ_1;
- ζ_2 governs the extension of the region interested by the pinching;
- ξ_0, δ_ξ and λ control the evolution of ζ_2.

6.2.6 The Foliente model

A further modification to the model with degrading and pinching was added by Foliente (1995) and Foliente et al. (1996),

$$\begin{cases} m\ddot{u}(t) + c\dot{u}(t) + \alpha k u(t) + z(t) = d(t) \\ \dot{z}(t) = \left\{ \frac{(1-\alpha)}{\eta} h[A - \nu|z(t)|^n(\gamma + \beta sign(z(t)\dot{u}(t))] \right\} \dot{u}(t) \\ \dot{e}(t) = z(t)\dot{u}(t) \end{cases} \tag{6.19}$$

In particular, the function $h(z, e)$ has non-zero mean and equal to $\bar{z}$. The maximum pinching effect occurs for $z = \bar{z} = qz_u$ as shown in figure 6.2 b). The function $h(z, e)$ writes

$$h = h(z, e) = 1 - \zeta_1 e^{\left(-\frac{(zsign\dot{u} - \bar{z})^2}{\zeta_2^2} \right)} \tag{6.20}$$

and

$$\bar{z} = \bar{z}(e) = qz_u = q\left(\frac{1}{\nu(\gamma + \beta)}\right)^{\frac{1}{n}} \tag{6.21}$$

Other parameters result to be

$$\nu = \nu(e) = \nu_0 + \delta_\nu e \tag{6.22}$$

$$\eta = \eta(e) = \eta_0 + \delta_\eta e \tag{6.23}$$

$$\zeta_1 = \zeta_1(e) = \zeta_{1,0}(1 - e^{-pe}) \tag{6.24}$$

$$\zeta_2 = \zeta_2(e) = (\xi_0 + \delta_\xi)(\lambda + \zeta_1) \tag{6.25}$$

6.3 MR fluids and hysteresis mathematical models

A MR fluid is typically composed for the 20-40 % (Spencer et al., 1997) of their total volume by micron size (3-5 micron) soft iron particles, e.g. carbonyl iron,

suspended in a non-magnetic fluid that acts as a carrier matrix for the polarizable part. The particle size range from $10^{-7}$to 10^{-5} m (Carlson and Jolly, 2000). Upon the application of a magnetic field, the rheological properties of these materials drastically change since they modify the basic consistence from linear viscous fluid to semi-solid state and the aggregation is reversible. The magnetization of the fluid yields to the formation of chain-like structures composed by the magnetic part of the fluid, parallel to the applied magnetic field and that restrict the flow of the fluid dramatically changing the rheological behavior of the material. The change is really quick (of the order of milliseconds) and fits to real-time control applications. Of course, the yield stress is field dependent since the yield strength is controllable as a function of the magnetic field in the coil of the device (Jolly et al., 1996). Carrier fluids can be petroleum based oils, silicone, mineral oils, polyesters, polyethers, water synthetic hydrocarbon oil (Carlson and Jolly, 2000) and other. The basic physical properties are summarized in table 6.2.

Table 6.2: typical MR fluid properties (Carlson et al., 1996; Carlson and Jolly, 2000).

Property	Typical value
Maximum yield strength	50-100 kPa
Maximum field	$\sim$250 kA/m
Plastic viscosity	0.1-1.0 Pa s
Operable temperature range	-40/+150°C
Contaminants	unaffected by most impurities
Response time	¡ milliseconds
Density	3-4 g/cm^3
$\frac{\eta p}{\tau_y^2}$	$10^{-10} - 10^{-11}$s/Pa
Maximum energy density	0.1 J/cm^3
Power supply (typical)	2-25 V @1-2 A (2-50 watts)

Relevant MR fluids models currently used in literature are here reported.

- The Bingham model consists of a Coulomb friction element placed in parallel with a viscous damper as shown in figure 6.3.

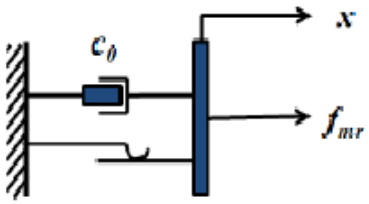

Figure 6.3: the Bingham model (Zapateiro De La Hoz, 2009)

The Bingham model is often used to characterize the the stress-strain relationship. The stress is proportional to the viscosity, defined as the ratio between shear stress and gradient of the velocity orthogonal to the strain direction,

$$\tau = \mu \frac{du}{dy} \tag{6.26}$$

The flow of the fluid is governed by the Bingham model when the body behaves as a solid until the yielding stress is reached, then exhibits a linear relation between the stress and the rate of deformation. Then the stresses $\tau \geq \tau_y$ result

$$\tau = \tau_y + \mu\dot{\gamma} \tag{6.27}$$

meanwhile for stresses below $\tau < \tau_y$, the fluid behaves elastically,

$$\tau = G\gamma \tag{6.28}$$

where G is the complex material modulus. The force f_{mr} is given by the following equation

$$f_{mr} = f_c sgn(\dot{x}) + c_0 x + f_0 \tag{6.29}$$

where c_0 is the damping coefficient, f_c is the frictional force, $\dot{x}$ is the velocity of the head of the piston and f_0 is a general term used to model non-zero mean effects. Modification to the Bingham model can be found in Stanway et al. (1985, 1987); Gamota and Filisko (1991).

- Bouc-Wen based models have been extensively used to describe the rheological behavior of dissipative device such as MR fluid dampers since it possesses a behavior resembling that of the real MR dampers. Dominiquez et al.

(2008, 2006) proposed a model based one the Bouc-Wen and including both the amplitude and frequency of the excitation and the current flowing into the device, as input variables finding the solution of the evolutionary variable z as a function of 16 current/excitation dependent parameters. A more involved model is presented by Spencer et al. (1997) based on the results of damping testing on a Lord MR damper and showed in figure 6.4.

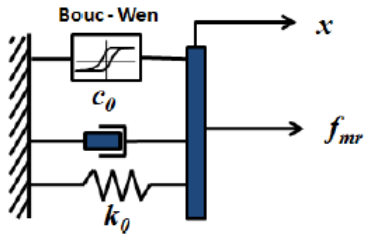

Figure 6.4: the Bouc-Wen mechanical model (Zapateiro De La Hoz, 2009)

- Hyperbolic tangent model is presented by Gamota and Filisko (1991) and simplified by Gavin (2001). The model illustrated in figure 6.5 consists in a damping coefficient c_0 and a stiffness k_0 both describing the post-yield behavior while c_1 and k_1 represent the pre-yield behavior, respectively. The Coulomb friction element is also present. Actually the model is constituted by two Voight elements separated by a mass m_0 representing the inertia of the device or of the fluid. This model is used to approximate the both a signum function and a yielding mechanism.

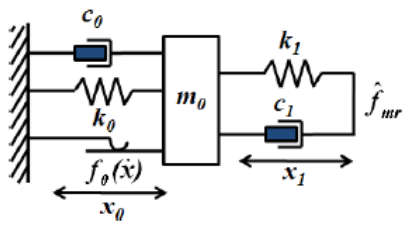

Figure 6.5: the Hyperbolic tangent model (Zapateiro De La Hoz, 2009)

- Dahl friction model presented in figure 6.6 is described by the following set of equations,

$$\begin{aligned} F &= k_x(v)\dot{x} + k_w(v)z(t) \\ \dot{z} &= \rho\left(\dot{x} - |\dot{x}|z\right) \end{aligned} \tag{6.30}$$

Ikhouane and Dyke (2007) and Ikhouane et al. (2007) proposed the use of the

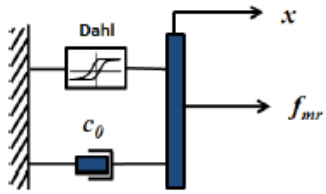

Figure 6.6: the Dahl friction model (Zapateiro De La Hoz, 2009)

Dahl model in conjunction with a viscous dash-pot for the behavior of damping devices. The model is also suitable for a possible dependence of the parameters from voltage.

- LuGree model is used in Jimenez and Alvarez-Icaza (2005) in order to model a MR damper. The LuGree model is an extension of the Dahl model and is a way to describe friction dynamics. The parameters are voltage dependent and the model is given by,

$$\begin{aligned} f_{mr} &= \sigma_0 zv + \sigma_1 \dot{z} + \sigma_2 \dot{x} \\ \dot{z} &= \dot{x} - \sigma_0 \eta_0(v)|\dot{x}|z \end{aligned} \tag{6.31}$$

where σ_0 (N/mV), σ_1 (Ns/m) and σ_2 (Ns/m) are the characteristic parameters of the model, stiffness and dissipation coefficients, respectively. η_0 is related to the voltage through the relation $\eta_0(v) = a_0(1 + a_1 v)$ with a_0 (V/N) and a_1 (V^{-1}) are constant parameters.

- Non parametric such as neural network, fuzzy logic models and n-order polynomial equations are also present in the literature (Nelles, 2001).

6.4 Non-linear identification of the MR damper

The goal of model identification is the realization of an accurate analytical model based on the input-output measurements from actual structures or devices. With

regard to the linear identification, the most popular classification of methods entails: a) time domain such as Autoregressive methods (Maia and Silva, 1997; Leuridan et al., 1985; Giorcelli et al., 1994), the Eigensystem Realization Algorithm (ERA) (Maia and Silva, 1997; Juang and Phan, 2001), the Stochastic Subspace Identification method (SSI) (Van Overschee and De Moor, 1996), b) frequency domain (Zanotti, 2012) and c) time-frequency domain strategies (Cohen, 1995; Ceravolo, 2004; Hlawatsch and Boudreaux-Bartels, 2006). Another common classification is related to the objective of the identification; direct methods directly identify the system matrices (mass, stiffness matrices of the system model, when the system is small enough) while indirect methods estimate the modal characteristic of the structure (frequencies and mode shapes) by means of the Frequency Response Function (FRF). However, structures under sever load condition may exhibit non-linearity since the restoring force shows hysteretic behavior, or one can be in presence of local element with a clear non-linear behavior. So the second big branch of the model identification is related to non-linear systems. A first partition for non-linear identification methods is between parametric and non-parametric methods; the first class of methods use a priori knowledge of the model class and lead to the identification of model parameters by searching in the parameter space. The latter, do not require any assumption about the type and the order of the non-linearity of the system but at the cost of a certain mathematical complexity. An exhaustive classification is in Zanotti (2012) and reported in figure 6.7. The main distinction is between Non-Instantaneous and Instantaneous methods. In particular, the Kalman filter for parameter estimation is part of the so called on-line methods in time domain. Indeed, adaptive estimation procedure are really attractive to perform on-line identification of non-liner systems (Smyth et al., 2002). In this section a modified version of the Bouc-Wen model is used for simulating and identifying the non-linear behavior of the MR damper to be used within the damping system of the Nomi-Calliano footbridge. Identifying a model consists in proposing a set of unknown parameters and an identification algorithm able to precisely simulate the input-output measured relationship. An overview of the identification method is proposed in Ismail et al. (2009), so in addition to the above-mentioned classification, one can add the following techniques:

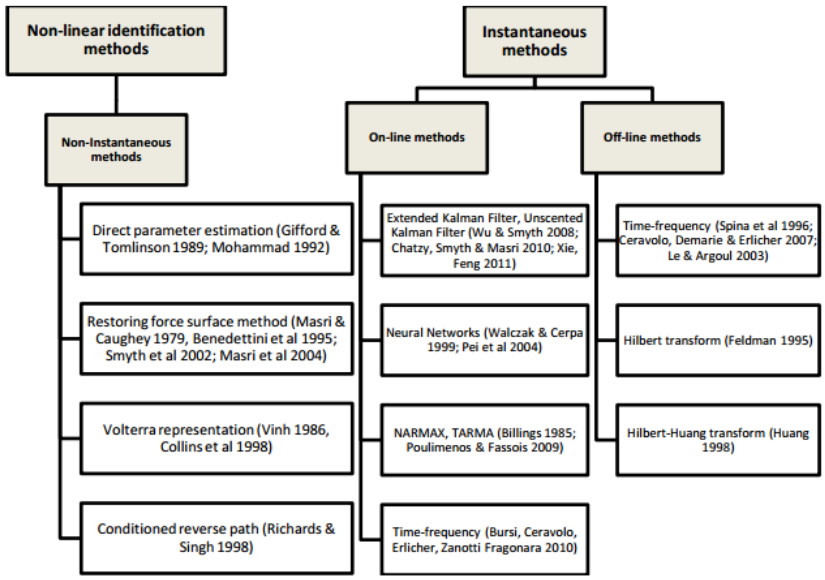

Figure 6.7: classification of non linear identification methods (Zanotti, 2012).

- Least-square based (Smyth et al., 1999);
- Bootstrap filter based (Li et al., 2004)
- Simplex method (Ramallo et al., 2004; Gunstona et al., 2004);
- Genetic Algorithm (GA) based (Kwok et al., 2007; Ma et al., 2006); briefly, the GA deals with a set of potential solutions, i.e. the MR damper parameters, called chromosomes randomly generated to represent parameters. The algorithm proceeds along iteration called generations, going through the selection, crossover and mutation operation till the best chromosome solution is found
- Constrained non-linear Optimization (Savaresi et al., 2005);
- Non-parametric identification (Masri et al., 2004).

In this chapter, both a constrained non-linear and a Kalman filter based optimization are used. In the first stage of identification, the hysteresis parameters are identified by the solution of a non-linear minimum constrained problem. In the

second identification stage, the UKF technique is tested as a tool for non-linear identification of the model parameters.

6.4.1 MR damper and test description

Tests on the MR damper aimed to identify the parametric model toke place using an experimental platform -the Test Rig 1 (TT1) - already existing in the Materials and Structural Testing Laboratory of the University of Trento. The TT1 is a dynamic system developed by the Department of Civil, Mechanical and Environmental Engineering of the University of Trento (Italy) as part of the project SERIES (Seismic Engineering Research Structures for European Synergies) to study and validate control techniques for evaluation of accuracy of Real-Time Heterogeneous Simulations (RHS). By default there are two masses of 234 kg each free to translate and rotate and handled by four electromechanical actuators. Different type of springs and dampers are also available for the variation of the parameters of the dynamic system. The masses are arranged on guides equipped with bearings to definitely reduce the friction. The hardware of the TT1 is presented in figure 6.8 and consists of four actuators Parker 890 CD (Common Drive) powered by the Parker 890 CS - Common Bus Supply, four load cells AEP-TC4 25 kN, four accelerometers PCB 393B12 and 393C and eventually four optical displacement transducers OPTO NCDT 1402-200. The dSPACE® platform is used for both measurement acquisition and signal control. TT1 can be used with or without specimen. The TT1 is endowed with:

- Four actuators Parker 890 CD with modular driving system AC 890 are fed by the 890 CS Parker Common Bus Supply with a velocity control loop (figure 6.9 shows a sketch of the Parker actuator).

- Four displacement sensors OPTO NCDT 1402-200 detect the position of the head of each actuator. These sensors exploit the principle of triangulation: a visible light beam is projected onto a target surface and the reflection is measured by a receiving high sensitivity optical element positioned with a certain angle with respect to the laser beam. The measuring range is 60 mm and the voltage-displacement relationship reads,

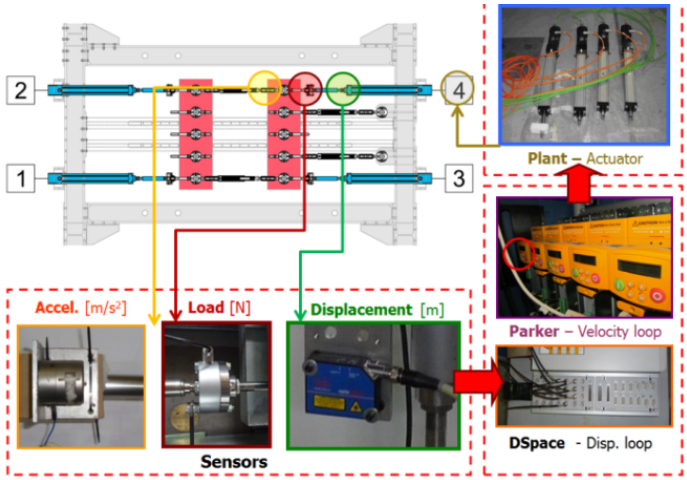

Figure 6.8: The TT1 sensor and plant set-up.

$$d[mm] = d_1 \Delta V[V] + d_0 \tag{6.32}$$

where $d_1 = 0.05$ m/V and $d_0 = -0.15$ m

- The force exerted by the actuators is measured by means of four load cells AEP TC4 25kN. The load cell shown in figure 6.10 contains a Wheatstone bridge that links the mechanical deformation with the variation of an electrical resistance in such a way that the loads is defined by a symmetric shear deformation (figure6.10).

- There are four 393 B12 accelerometers made by PCB Piezotronics. The sensitivity is 10 V/g that is 1 Vs^2/m and the measuring range is $\pm 0.5g$ (± 5 m/s^2). Accelerometers have their own power converter and power supply.

The planned set-up for the damper characterization is presented in figure 6.11 and shows the rotational MR damper produced by Maurer Shne Gmbh positioned inside the TT1 without the default additional masses. This set-up is used to identify the non-linear behavior of the device, i. e. the non-linear dependence of the damper force with the displacement and velocity. In addition the set-up is useful to identify the current-damping force relationship. Besides actuators, load cells and displacement transducers, the TT1 test rig was equipped with:

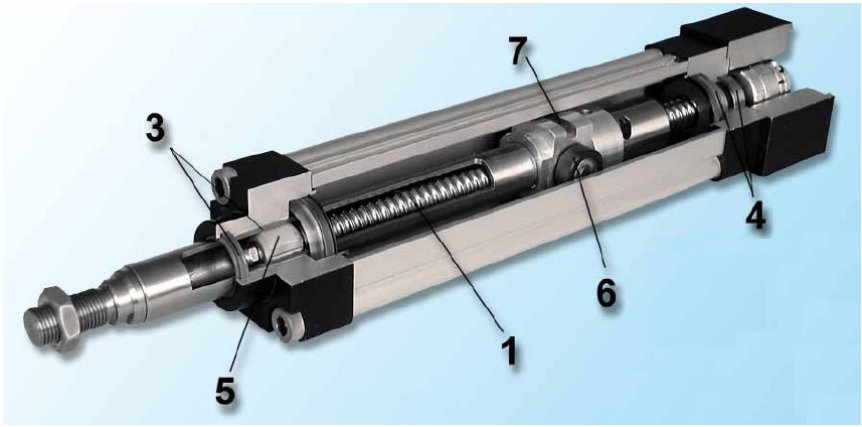

Figure 6.9: sketch of the Parker actuator.

Figure 6.10: the load cell TC4 25kN.

- The dSPACE® platform which is used for both measurement acquisition and signal control;

- the MR rotational damper with a current maximum limit of 6A and electrical resistance of 3.6 Ω; it consists of a disk-type MR damper produced by Maurer Shne Gmbh with MR fluid MRB10;

- the current regulator IASP Gmbh type CR 603 which is designed to energize the electrical component starting from a voltage set-point; the changing speed of the current, for a unit step function, is only a few milliseconds;

- the load cell AEP TS of 200 kg placed in axis with the gear beam and its analog transducer AEP TA/2.

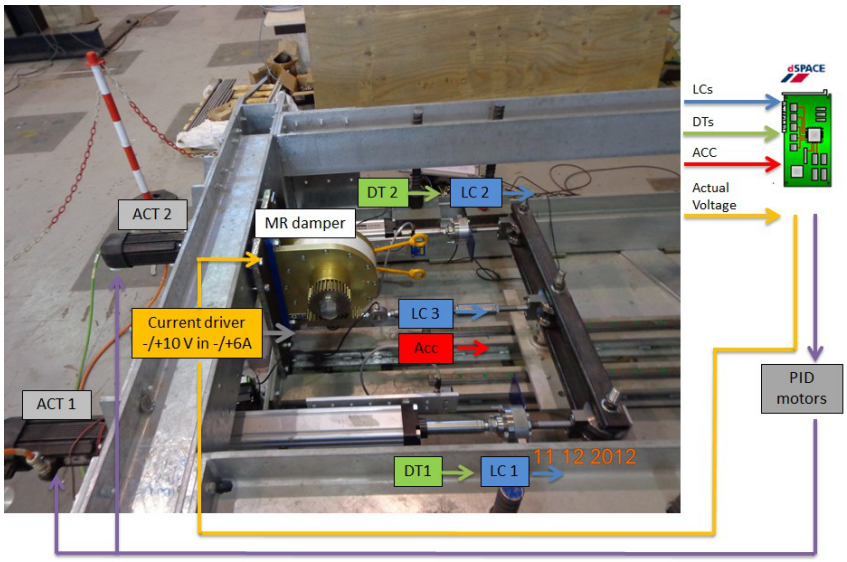

Figure 6.11: Control and acquisition instrumentation set-up in the TT1 Test rig.

The MR damper is a product of Maurer & Soehne and is a rotatory damper able to change its characteristics after the application of a current. Technical data of the MR damper are reported in table 6.3. The damper is composed by the main

Table 6.3: specifications of the MR damper

Technical data	
Fmax	$\sim 5000N$
Tmin	-40 $^{\circ}C$
Tmax	60 $^{\circ}C$
Supply current	4.5 A
Tension	24 V
Resistance	3.6 Ω

body an by the internal disk totally immersed in the fluid that is magnetizes by two coils positioned on both sides of the internal disk. The current regulator is designed to energize the damper and its power supply is 24V DC. Over an analog input (-10...+10V), the device regulate a current between -8 A and +8 A if the load resistance is less than 3 Ω. Since in the case of the damper the load resistance

is 3.6 Ω, the regulation limits became ±6 A over an analog input of ±7.5 V. The relationship between the applied voltage and the current flowing into the device is linear and defined as,

$$i = 0.85V \tag{6.33}$$

The declared changing speed of the current, for a step function, is only a few milliseconds. The characterization of the damper consists of tests to acquire displacement-force and velocity-force curves under different input and voltage conditions. Several test were performed as shown in table 6.4 in displacement control for different level of voltage and different amplitude and frequency of the sinusoidal displacement. The displacement set points were defined according to the footbridge characteristic in terms of both the damper allowable displacement and modal frequencies of the primary structure. Since the maximum allowable damper displacement is 40 mm, the desired actuator set-points are sinusoidal displacement of 10 mm and 14 mm and with a frequency range of the harmonic excitation in the range of 0.25 Hz 2 Hz and at different level of current ranging from 0 A to 6 A. Signals are filtered with a Butterworth filter characterized by a cut-off frequency of 300 Hz. Force-time, force-displacement and force-velocity plot are arranged by

Table 6.4: list of tests.

Sinusoidal displacement		Voltage
Amplitude [mm]	Frequency [Hz]	
10	0.25	0V-1V-2V-3V-4V-5V-6V
10	0.5	0V-1V-2V-3V-4V-5V-6V
10	1.0	0V-1V-2V-3V-4V-5V-6V
10	1.5	0V-1V-2V-3V-4V-5V-6V
10	2.0	0V-1V-2V-3V-4V-5V-6V
14	0.25	0V-1V-2V-3V-4V-5V-6V
14	0.5	0V-1V-2V-3V-4V-5V-6V
14	1.0	0V-1V-2V-3V-4V-5V-6V
14	1.5	0V-1V-2V-3V-4V-5V-6V
14	2.0	0V-1V-2V-3V-4V-5V-6V

different level of voltage and by different frequency and amplitude of the imposed displacement. The damper force at 0 V is clearly frequency dependent as shown in figure 6.33. This behavior tends to decrease for highest voltage applied as reported in figure 6.34. In addition the damper behavior is almost viscous for zero voltage and high frequencies. In the tested range, the force level spans between -/+ 65 N at 0V and -/+2000 N at almost 6 V with a displacement amplitude of 10 mm and between -/+ 75 N at 0V and -/+2200 N at almost 6 V with a displacement amplitude of 14 mm. Detailed results obtained from tests at 0.25 Hz, 1 Hz and 2 Hz are reported in the Appendix C at the end of the Chapter. In conclusion tests demonstrated that the force level is both voltage and input dependent. Then, for low frequency of the excitation, the behavior appears to be Bouc-Wen like while for high frequency, the viscous component arises. In addition, the viscous component increases with low voltage levels. So the global behavior results to be clearly frequency and, of course, voltage dependent.

6.4.2 Parametric model of the damper and results

The adopted model is reported in figure 6.12 and reproduces the dynamic of the experiment. The damper has been modeled by means of a Bouc-Wen-based

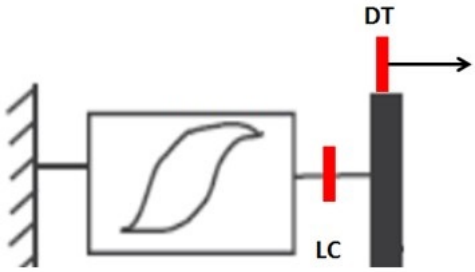

Figure 6.12: TT1 set-up for the damper identification.

model in parallel with a viscous element characterized by

$$f = \alpha z + c_0 \dot{u} \tag{6.34}$$

with

$$\dot{z} = A\dot{u} + \beta \dot{u}|z|^n - \gamma z|\dot{u}||z|^{n-1} \tag{6.35}$$

where

- αz is the hysteresis term;
- $c_0 \dot{u}$ is the linear viscous dash-pot.

In order to characterize the damper parameters. Some trial and error pre-test were been carried out in order to both define some initial condition useful for the optimization problem and understand the Bouc-Wen parameters influence on the hysteresis shape. Tests showed that A, β and γ are rate-dependent. Spencer and Sain (1997) and Dyke et al. (1996) suggested the following linear relationship between voltage and both the hysteresis scaling factor and the viscous damping coefficient, i.e.

$$c_0 = c_{0a} + c_{0b} V \tag{6.36}$$

and

$$\alpha_0 = \alpha_{0a} + \alpha_{0b} V \tag{6.37}$$

Pre-tests showed that:

- A, β and γ are function of both the frequency and the amplitude of the input and independent from the applied voltage as shown in table 6.5.

Table 6.5: Values for parameters A, β and γ.

f [Hz]	10 mm amplitude			14 mm amplitude		
	A [Ns/mm]	β [mm^{-2}]	γ [mm^{-2}]	A [Ns/mm]	β [mm^{-2}]	γ [mm^{-2}]
0.25	200	1.2	1.2	210	1.05	1.05
0.5	130	0.7	0.7	120	0.6	0.6
1.0	75	0.4	0.4	70	0.35	0.35
1.5	50	0.25	0.25	40	0.2	0.2
2.0	40	0.2	0.2	30	0.15	0.15

As a result, the characterizing equations for A, β and γ are represented by the following polynomial expression,

$$A(f, Amp) = a_{00}+a_{10}f+a_{01}Amp+a_{20}f^2+a_{11}fAmp+a_{02}Amp^2+a_{30}f^3+a_{21}f^2Amp+a_{12}fAmp^2$$

(6.38)

where f is normalized with mean 1.05 and *std* 0.6628 and *Amp* is normalized with mean 9.667 and *std* 3.811. Coefficients with 95% confidence bounds result: a_{00} = 551.3, $a_{10} = -711.9$, $a_{01} = -32.25$, a_{20} = 440.7, a_{11} = 14.9, a_{02} = 1.131, $a_{30} = -93.37$, $a_{21} = -3.242$ and $a_{12} = -0.3205$. The goodness of the fit is $R - square$ = 0.9918.

A simpler model considering a constant frequency of 1.5 Hz writes

$$A(1.5, Amp) = 114.67 - 5.65667 Amp \tag{6.39}$$

With regard to β and γ,

$$\beta(f, Amp) = b_{00} + b_{10} f + b_{01} Amp + b_{20} f^2 + b_{11} f Amp + b_{02} Amp^2 + b_{30} f^3 + b_{21} f^2 Amp + b_{12} f Amp^2 \tag{6.40}$$

Coefficients with 95% confidence bounds result: b_{00} = 1.965, $b_{10} = -3.002$, $b_{01} = -0.002913$, b_{20} = 2.006, $b_{11} = -0.006122$, $b_{02} = -0.001529$, $b_{30} = -0.4379$, $b_{21} = -0.007047$, b_{12} = 0.001457. The goodness of the fit is $R - square$ = 0.9900.

$$\beta(x, y) = \gamma(f, Amp) \tag{6.41}$$

and similarly a second model tuned on the single frequency of 1.5 Hz is estimated

$$\beta(1.5, Amp) = \gamma(1.5, Amp) = 0.4291 - 0.0168 Amp \tag{6.42}$$

- c and α are voltage dependent and the relationship with the voltage is presented in eqs. 6.43 and 6.44. Actually eq. 6.44 is the result of the interpolation of the value reported in table 6.6 with $R - square$ of 0.9925 and 0.9955 , respectively.

  $$c_0(V) = c_{00} + c_{10} V + c_{01} V^2 \tag{6.43}$$

  with c_{00} = 0.4262, c_{10} = 0.1321, c_{01} = 0.0202.

  $$\alpha_0(V) = \alpha_{00} + \alpha_{10} V + \alpha_{01} V^2 \tag{6.44}$$

  with α_{00} = 0.6, α_{10} = 0.59, α_{01} = 0.1694.

Table 6.6: values of the parameter α_0

Frequency [Hz]	Voltage [V]						
	0	1	2	3	4	5	6
0.25	0.95	2	2.8	3.9	6.00	8.00	1.00
0.5	0.85	1.9	2.7	3.8	6.00	8.00	1.00
1.0	0.6	1.5	2.6	3.8	6.00	8.00	1.00
1.5	0.5	1.3	2.3	3.8	6.00	8.00	1.00
2.0	0.4	1.2	2.2	3.8	6.00	8.00	1.00

- n is slightly voltage dependent: 1.15-1.05-0.9-0.85-0.85-0.85-0.85 for 0-1-2-3-4-5-6 V and $R - square$ = 0.972.

$$n(V) = 0.01361\,V^2 - 0.1446\,V + 1.1536 \tag{6.45}$$

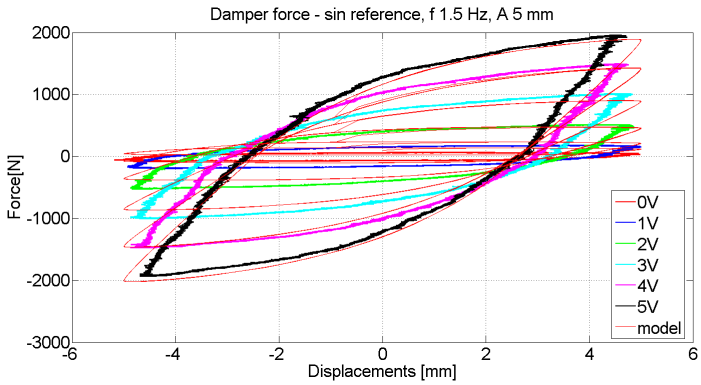

Figure 6.13: model validation of the input dependent model.

The model presents good agreement with experimental data for higher frequencies in the range of 1-2 Hz as shown in figure 6.13; while for low frequencies such as 0.25 Hz the numerical behavior can be improved at low voltages. The frequency of the MR-TMD activation is related to the frequency of the pedestrian load so a simplified model was adopted for the working frequency of 1.5 Hz of the bridge. The choose is to use a simplified voltage dependent Bouc-Wen based model and to optimize data around 1.5 Hz, i.e. the frequency of the resonant vertical pedestrian load. Parameters are optimized in order to find a second model working

in a restricted range but dependent only by the voltage. Parameter optimization took place by minimizing the residual between the measured force and the force yielded by the adopted model. The objective function used to minimize the residual between model and experimental data was:

$$J = \sum \frac{||f_{est}(t) - f_m(t)||^2}{||f_m||^2} \tag{6.46}$$

where f_{est} is the estimated damping force with known input and f_m is the force measured by the load cell on the damper. The non-linear minimum problem was constrained in a range of +/- 50 % of parameters value, in order to ensure the BIBO response of the model. The "Patternsearch" function in the MATLAB optimization toolbox was used (Matlab®, 2009). Optimized parameters are reported in tables 6.7 and 6.8. The simplified model obtained from fitting the results is described by

Table 6.7: test with 10 mm of the sine amplitude: optimized parameters.

		A	β	γ	α_0	c_0
0V	i.c.	50	0.25	0.25	0.6	0.4
	opt. par	42.83	0.38	0.22	0.43	0.54
1V	i.c.	50	0.25	0.25	1.5	0.6
	opt. par	59.84	0.18	0.18	0.92	0.35
2V	i.c.	50	0.25	0.25	2.6	0.8
	opt. par	57.5	0.27	0.22	1.99	0.6
3V	i.c.	50	0.25	0.25	3.8	1.00
	opt. par	54.07	0.29	0.23	3.52	1.01
4V	i.c.	50	0.25	0.25	6	1.3
	opt. par	51.28	0.27	0.24	5.82	0.87
5V	i.c.	50	0.25	0.25	8	1.5
	opt. par	50.63	0.26	0.24	7.76	1.30
6V	i.c.	50	0.25	0.25	10	2
	opt. par	50.95	0.24	0.23	9.31	1.66

the following relations,

$$A(V) = 0.0177V^2 - 1.4301V + 55 \tag{6.47}$$

Table 6.8: test with 14 mm of the sine amplitude: optimized parameters.

		A	β	γ	α_0	c_0
0V	i.c.	40	0.2	0.2	0.6	0.4
	opt. par	48.16	0.4	0.36	0.44	0.55
1V	i.c.	40	0.2	0.2	1.5	0.6
	opt. par	66.43	0.11	0.11	0.68	0.44
2V	i.c.	40	0.2	0.2	2.6	0.8
	opt. par	68.18	0.29	0.12	1.45	0.50
3V	i.c.	40	0.2	0.2	3.8	1.0
	opt. par	48.12	0.26	0.17	3.26	1.05
4V	i.c.	40	0.2	0.2	6	1.3
	opt. par	46.77	0.25	0.17	5.02	1.01
5V	i.c.	40	0.2	0.2	8	1.5
	opt. par	45.74	0.23	0.17	6.99	1.15
6V	i.c.	40	0.2	0.2	10	2
	opt. par	43.56	0.2	0.17	8.86	1.57

$$\beta(V) = 0.0036V^2 - 0.033V + 0.3122 \tag{6.48}$$

$$\gamma(V) = 0.0074V^2 - 0.0499V + 0.2603 \tag{6.49}$$

$$\alpha(V) = 0.1501V^2 + 0.6293V + 0.1941 \tag{6.50}$$

$$c(V) = 0.0258V^2 + 0.0318V + 0.4731 \tag{6.51}$$

The validation is reported in figure 6.14 and shows the displacement-force cycle of the model overlapped with experimental data for a forcing frequency of 1.5 Hz and a displacement amplitude of 10 mm. The adherence with real data is good.

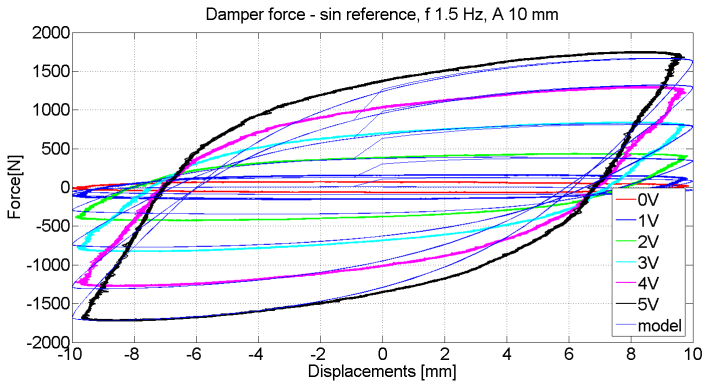

Figure 6.14: model validation of the voltage dependent model.

6.5 The UKF for parameter identification

In order to understand the validity of the Unscented Kalman filter (UKF) for the parameter estimation of non-linear hysteretic systems, we proceed with the application of the filter for the state estimation of a hysteretic SDoF system. The objective is to estimate parameters of a set of time invariant Bouc-Wen-like models such as the Bouc-Wen, Baber-Wen, Baber-Noori and Foliente model. Eventually, the experimental application on the damper performed by the use of the TT1 is reported.

6.5.1 Numerical benchmarks

The dynamic system is a time invariant SDoF endowed with an hysteresis element with restoring force is $z(t)$. The input $d(t)$ is the known sinusoidal input with frequency varying from 0.1 Hz to 2 Hz and amplitude of 10 N. The benchmark model has unitary mass, damping 0.3 Ns/m, stiffness equal to 9 N/m. Tests involve among others Bouc-Wen and Baber-Noori.

- Bouc-Wen

The state vector is defined as $X = [u, \dot{u}, z, A, \beta, \gamma, n]^T$ and the initial conditions is $X_0 = [0, 0, 0, 0.7, 1.5, 0.5, 1.5]^T$. The dynamic system in state space form results:

$$\dot{X} = f(X, d, w) = \begin{bmatrix} \dot{u}(t) \\ \ddot{u}(t) \\ \dot{z}(t) \\ \dot{A}(t) \\ \dot{\beta}(t) \\ \dot{\gamma}(t) \\ \dot{n}(t) \end{bmatrix} = \begin{bmatrix} \dot{u}(t) \\ -\frac{1}{m}\left(c\dot{u}(t) + ku(t) + z(t)\right) + d(t) \\ [A(t) - |z(t)|^{n(t)}(\gamma(t) + \beta(t)sign(z(t)\dot{u}(t)))]\dot{u}(t) \\ 0 \\ 0 \\ 0 \\ 0 \end{bmatrix} \tag{6.52}$$

assuming to know the mass acceleration and the external excitation, the equation of measurement results to be equal to

$$Y = h(X, v) = -\frac{1}{m}\left(c\dot{u}(t) + ku(t) + z(t) + v(t)\right) \tag{6.53}$$

The process noise and the measurement noise both have RMS equal to 10^{-6}. Furthermore, the filter parameters are $\alpha = 10^{-4}$, $\beta = 2$ and $k = -5$. Figure 6.15 shows results in term of comparison between numerical and estimated restoring force vs. displacements and time.

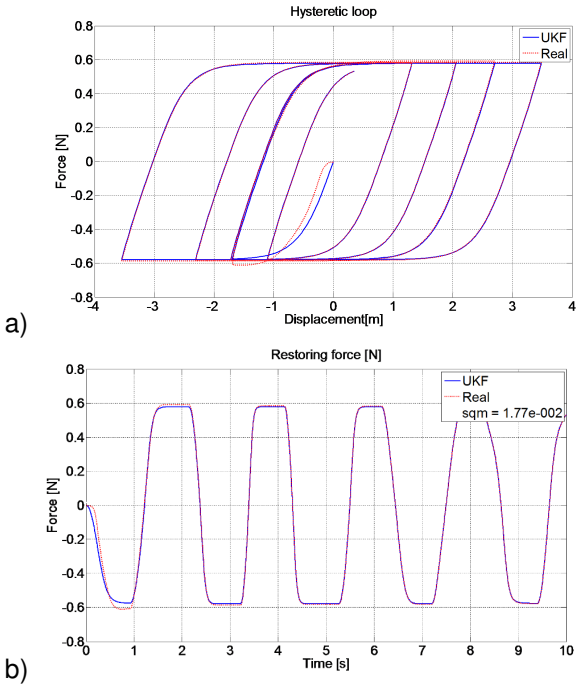

Figure 6.15: Bouc-Wen model, comparison between: a) numerical and estimated hysteretic cycle; b) numerical and estimated restoring force.

Figure 6.16 shows the results for hysteresis parameter estimation of the Bouc Wen model. The estimates of displacement, velocity and restoring force is ac-

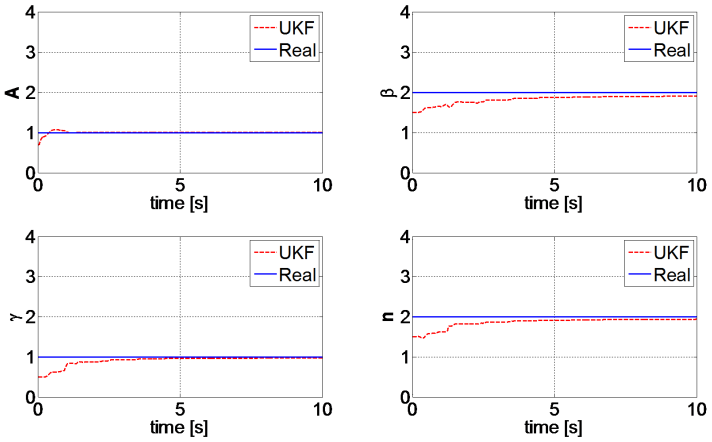

Figure 6.16: parameters estimation of the Bouc-Wen model.

curate, as shown in table 6.9 and the standard deviation of all variables is low. The estimation errors of hysteresis parameters are reported in table 6.9 and have average value of about 2.58% and maximum value of 4.61%.

Table 6.9: numerical, initial and estimated values of the Bouc-Wen model parameters.

Parameters	Exact value	Initial value	Estimated value	Error
A	1	0.7	1.0027	0.27
β	2	1.5	1.9078	4.61
γ	1	0.5	0.9751	2.49
n	2	1.5	1.9410	2.95

- Baber-Noori

The state vector is defined as $X = [u, \dot{u}, z, e, \beta, \gamma, n, \delta_A, \delta_\nu, \delta_\eta, \zeta_{1,0}, \xi_0, \delta_\xi, \lambda]^T$ and the initial conditions reads $X_0 = [0, 0, 0, 0, 1.7, 0.7, 1.7, 0.01, 0.01, 0.01, 0.6, 0.7, 0.1, 0.01, 0.1]^T$. The dynamic system in state space form is described in equation 6.54:

$$\dot{X} = f(X, d, w) = \begin{bmatrix} \dot{u}(t) \\ \ddot{u}(t) \\ \dot{z}(t) \\ \dot{e}(t) \\ \dot{\beta}(t) \\ \dot{\gamma}(t) \\ \dot{n}(t) \\ \dot{\delta}_A(t) \\ \dot{\delta}_\nu(t) \\ \dot{\delta}_\eta(t) \\ \dot{\zeta}_{1,0}(t) \\ \dot{\xi}_0(t) \\ \dot{\delta}_\xi(t) \\ \dot{\lambda}(t) \end{bmatrix} = \begin{bmatrix} \dot{u}(t) \\ -\frac{1}{m}\left(c\dot{u}(t) + \alpha k u(t) + z(t)\right) + d(t) + w(t) \\ \left\{\frac{(1-\alpha)A(t)}{\eta} h[1 - \nu|z(t)|^{n(t)}(\gamma(t) + \beta(t) sign(z(t)\dot{u}(t))]\right\} \dot{u}(t) \\ z(t)\dot{u}(t) \\ 0_{10x1} \end{bmatrix} \tag{6.54}$$

Figures 6.17 and 6.18 showresults in term of hysteretic loop and parameters of

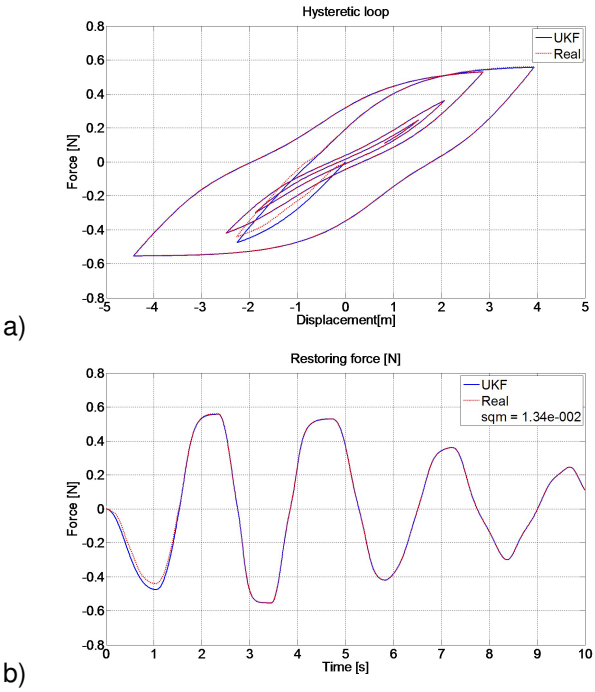

Figure 6.17: Baber-Noori model, comparison between: a) numerical and estimated hysteretic cycle; b) numerical and estimated restoring force.

the Baber Noori model with acceleration measurements, Table 6.10 shows initial and final values for the Baber Noori parameters and estimation errors.

6.5.2 Experimental application to time invariant MR damper

An additional test on the capability of the UKF is done by using real experimental data from the MR damper installed on the TT1. At this stage the identification is performed in reference to the stationary system without any change in the input

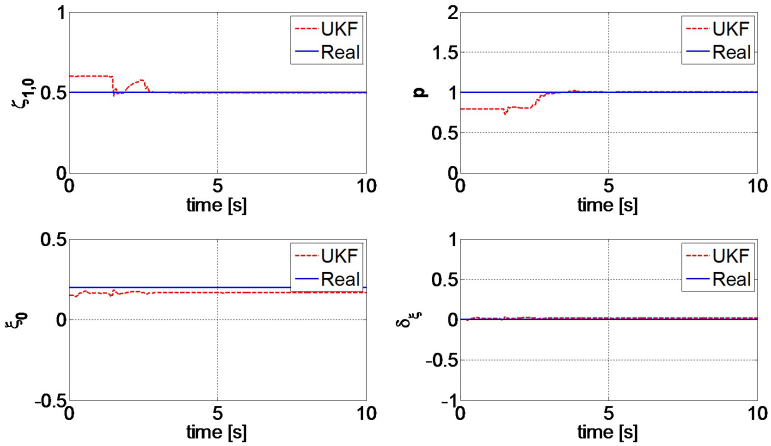

Figure 6.18: Baber Noori model; parameters estimation.

or in the applied voltage. The state space model is as follows,

$$\dot{X}(t) = \begin{bmatrix} \dot{z} \\ \dot{A} \\ \dot{\beta} \\ \dot{\gamma} \\ \dot{\alpha} \\ \dot{c} \\ \dot{f_d} \end{bmatrix} = \begin{bmatrix} [A - |z(t)|^n(\gamma + \beta sign(z(t)\dot{u}(t)))]\dot{u(t)} + w_1(t) \\ 0 \\ 0 \\ 0 \\ 0 \\ 0 \\ \alpha\dot{z(t)} + \alpha\dot{z}(t) + \dot{c}u(t) + c\ddot{u}(t) + w_2(t) \end{bmatrix} \tag{6.55}$$

The adopted configuration is the same used for the damper identification and showed in figure 6.11. The measured output is the force exerted by the damper,

$$Y(t) = h\left(X(t), v(t)\right) = [f_m(t) + v(t)] \tag{6.56}$$

As shown in figures 6.19 and 6.20, the matching is quite accurate since parameters are continuously varying around the initial condition.

6.6 Semi-active control

The classical design of a TMD is described by the Den Hartog theory and the original formulation assumes that frequency and modal mass of the critical mode are known due to the simplification of the structure (coupled with the TMD) to a simple 2DoF. In practical cases, the frequency of the structure can vary because of

Table 6.10: numerical, initial and estimated values of the Baber-Noori model parameters.

Parameters	Exact value	Initial value	Estimated value	Error
β	2	1.7	2.0079	0.39
γ	1	0.7	0.9745	2.55
n	2	1.7	2.0037	0.18
δ_A	0.02	0.01	0.0159	30.30
δ_ν	0.02	0.01	0.0219	9.36
δ_η	0.02	0.01	0.0265	32.65
$\zeta_{1,0}$	0.5	0.6	0.4977	0.46
p	1	0.7	1.0037	0.37
ξ_0	0.2	0.1	0.1684	15.78
δ_ξ	0.05	0.01	0.0214	328.8
λ	0.2	0.1	0.2503	25.13

uncertainties of the model, time varying loads or changes in the modal characteristic of the structure due to the temperature. On one hand the frequency variation can be detected by means of an on-line fast estimation using measured accelerations, on the other hand the estimation of the modal mass is more critical and can have different values because of the above-mentioned instances. This is the scenario for a possible de-tuning of the passive device resulting in a suboptimal TMD. To overcome the issue of de-tuning, semi-active control strategies have been developed. Semi active control systems use a fraction of the power required by active devices and they are inherently stable because they have bounded input in such a way they are also bounded output systems. In addition they have low operational costs, and low power requirements and don't add energy in the system. Basically the passive protection of the structure change while some mechanical parameters change in real time: in this way semi-active devices preserve in the same time reliability and adaptability, with an interesting compromise between passive and active strategy. The objective is to replace the passive optimal damper with a semi-active one characterized by a behavior based on a Bouc-Wen model. Then, an appro-

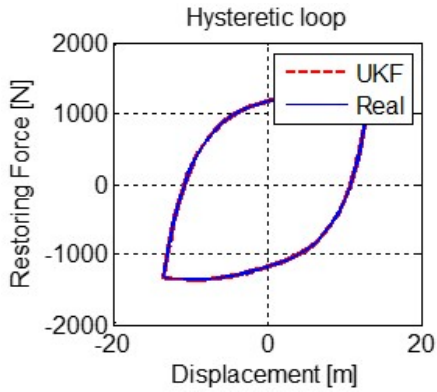

Figure 6.19: experimental test: comparison between measured and estimated hysteresis cycle.

priate control algorithm is applied to the damper by clipping in it the active control forces and taking into account the dissipative properties of the alternative damper.

6.6.1 Semi-active control strategies: state of the art

One of the most simple semi-active control law is the “Hook strategy” (Casciati et al., 2006). “Sky hook” and “ground hook” control strategies are based on a discrete or continuous damping variation between high and low state and are both called “intuitive” methods. These methods are quite practical because add damping and reduce the vibrations of the primary system in a very intuitive way. Sky hook and Ground hook are developed in order to reduce vibration amplitude of the upper body mass (m_b) and bottom body mass (m_t), respectively (Casciati et al., 2006) as showed in figure 6.21 a) and b). The goal is achieved by using the following control,

$$\begin{aligned} v_b(v_b - v_t) > 0,\ c = c_{high} \\ v_b(v_b - v_t) < 0,\ c = c_{low} \end{aligned} \tag{6.57}$$

and

$$\begin{aligned} v_t(v_b - v_t) < 0,\ c = c_{high} \\ v_t(v_b - v_t) > 0,\ c = c_{low} \end{aligned} \tag{6.58}$$

The control algorithm is based on a position logic and relevant parameters are reported in figure 6.22 It results that,

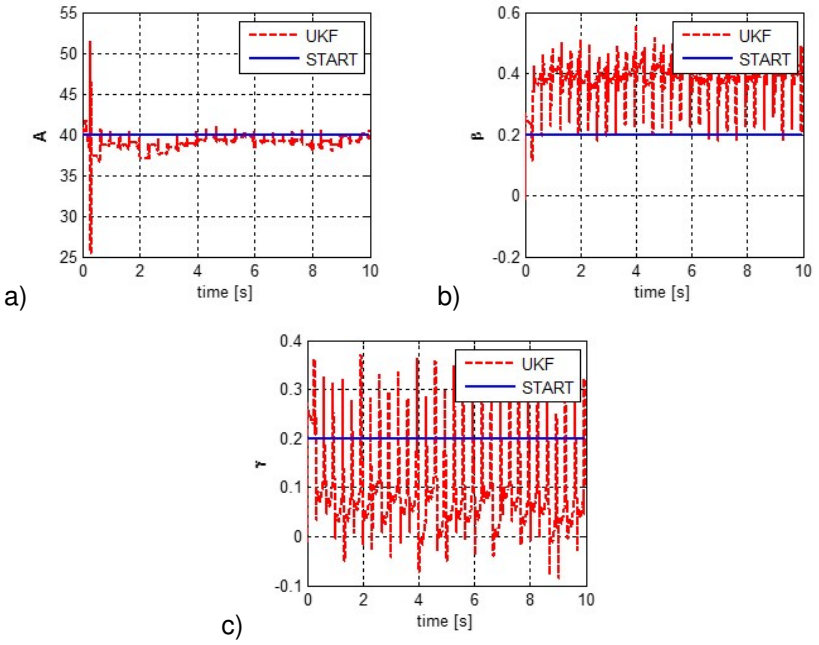

Figure 6.20: comparison between measured and estimated: a)A; b) β; and c)γ parameters.

- if the two masses go to different directions, the damping is set in high state and pull or push the masses close or far each other;
- in the Sky-hook logic, if the upper mass goes in the same direction of the bottom mass but it is faster, then damping is in high state, otherwise damping is in off state; dually, for the Ground hook logic we point attention on the bottom mass and if the bottom mass goes in the same direction of the upper mass but it is faster, then damping is in high state, otherwise damping is in off state.

An example is given in Koo (2003) where the Ground hook technique is used to re-design both the structure and the controller, minimizing the maximum value of trasmissibility as objective function in order to find the tuned vibration absorber parameters. The main idea is to find TMD parameters that generate the best model in terms of minimization of the maximum transmissibility value (ratio between output and input) or transfer function. Setareh (2001) searches for the optimum design

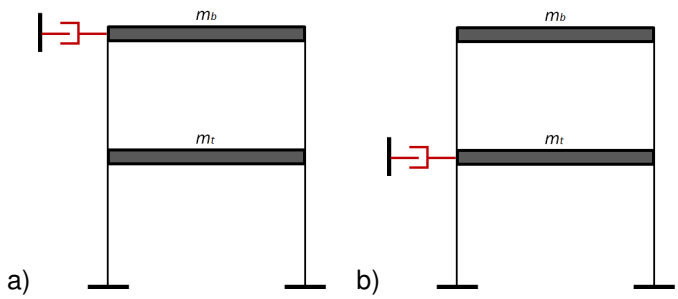

Figure 6.21: a) sky-hook logic; and b) ground-hook logic.

parameters of a continuously variable semi-active damper inside a TMD with the ground hook technique based on the minimization of the steady-state displacement response of the main mass. He wants to reduce the level of vibration of a single-degree-of-freedom system subjected to harmonic base excitations. The clipped control is the second most common intuitive control logic. In this respect, Dyke (1996) conducted a number of pilot studies to assess the usefulness of MR dampers for seismic response reduction. She proposed the clipped optimal control algorithm and tested it on a three story model configured with a single MR damper subjected to ground excitation. Jansen and Dyke (2000) used a variety of algorithms common in recent semi-active control studies; one of these is the clipped optimal control. They use accelerations in selected points and displacements of each control device to test the feedback loop of the H_2/LQR clipped control methods of a six story building controlled by four MR dampers and subjected to the N-E El Centro earthquake components. Pinkaew and Fujino (2001) investigated Semi-active Tuned Mass Damper (STMD) with variable damping under harmonic excitation. Using an optimal control law that minimize the quadratic performance index, they evaluated response of a SDoF system with passive and semi-active TMD by modification of damping. Results showed that vibration suppression by an STMD is superior to that of a conventional passive TMD in both transient and steady-state responses. Also Yuen et al. (2007) used a clipped optimal control to design one simulated MR damper based on robust reliability-based control methodology. In order to evaluate the feasibility and efficiency of the method, they used a ten story shear type building with two dampers under ground motion loading. Occhi-

CASE	1	2	3	4	5	6	7	8
Vb	+	+	+	+	-	-	-	-
Vt	+	+	-	-	+	+	-	-
Vb-Vt=Vrel	+	-	+	+	-	-	-	+
	|vt| < |vb|	|vt| > |vb|	|vt| < |vb|	|vt| > |vb|	|vt| < |vb|	|vt| > |vb|	|vt| < |vb|	|vt| > |vb|
Direzione Vb	→	→	→	→	←	←	←	←
Direzione Vt	→	→	←	←	→	→	←	←
Direzione Vrel	→	←	→	→	←	←	←	→
Damper	ext	comp	ext	ext	comp	comp	comp	ext
Vb*(Vb-Vt)	+	-	+	+	+	+	+	-
Skyhook damping	h	l	h	h	h	h	h	l
Vt*(Vb-Vt)	+	-	-	-	-	-	+	-
Ground hook damping	l	h	h	h	h	h	l	h

Figure 6.22: the “Hook” logic.

uzzi et al. (2002) performed a numerical simulation of the feedback LQR clipped optimal law of a 2DoF system (one DoF for the footbridge mode and one DoF for the device) subjected to sinusoid wave in resonance with the first vibration mode of the structure.

6.6.2 Clipped optimal control in detail

The approach proposed in Dyke (1996) consists in the use of a feedback loop to force the MR damper to generate approximately the desired optimal control force $r(t)$. $r(t)$ is designed by means of a linear optimal controller K_{LQR} based on measured structural responses $y(t)$ and $F_d(t)$ is usually defined as the force actually exerted by the damper. The Clipped control is composed by two steps (Casciati et al., 2006): i) the first part consists of the design of an active control law for an ideal active damper; so here we can use every type of control law; ii) in the second part the clipping controller develops a force matching the desired control force.

The second step is independent and consists in the design of a clipping controller that develops a force able to match approximately the desired control force. In a MR damper we cannot command the force $F_d(t)$ but only the voltage V applied to the current driver. The voltage modifies the MR properties to generate the desired control force. The control law read the force $F_d(t)$ produced by the damper and its sign; if the damper force is lower than the desired force and their sign is the same, the voltage applied is increased to the maximum level in order to increase the force exerted by the damper itself, zero otherwise. The control law read the force $F_d(t)$ produced by the damper and its sign and then applies the clipped algorithm as shown in eq. 6.59. In this way, the optimal control force tracks at any time the force $F_d(t)$ provided by the damper as close as possible to the control law $r(t)$ avoiding to introduce energy into the system. Indeed, the clipped logic results in adding to the structure an higher damping if the active control law is dissipative, but when the algorithm generates a not dissipative control force, then the effective force exerted by the damper is kept as lower as possible. On the other hand if $r(t)$ results to be higher than the actual $F_d(t)$, the maximum voltage is applied in order to provide the maximum force. The graphical representation of the algorithm is in figure 6.23 and can be stated as,

$$V = V_{max} H(r - F_d) F_d \tag{6.59}$$

or

$$i = i_{max} H(r - F_d) F_d \tag{6.60}$$

where $r(t)$ is the desired control force, $F_d(t)$ is the force exerted by the damper, H is the Heaviside function, V_{max} is the maximum applicable voltage and i_{max} is the maximum applicable current if the command is used in voltage or current, respectively. Since the strategy consists in two separate stages (i-optimal control force calculation and ii-control voltage/current estimation) a variety of control approaches can be used to design the optimal control law. For example H_2/LQR strategies had successful application. Dyke (1996) and Occhiuzzi et al. (2002) used LQR clipped optimal strategy in their work. The main goal of so called LQR implementation strategies is minimizing an object function with both the full state and the control force. Let the model of the open-loop process be the dynamical system in state

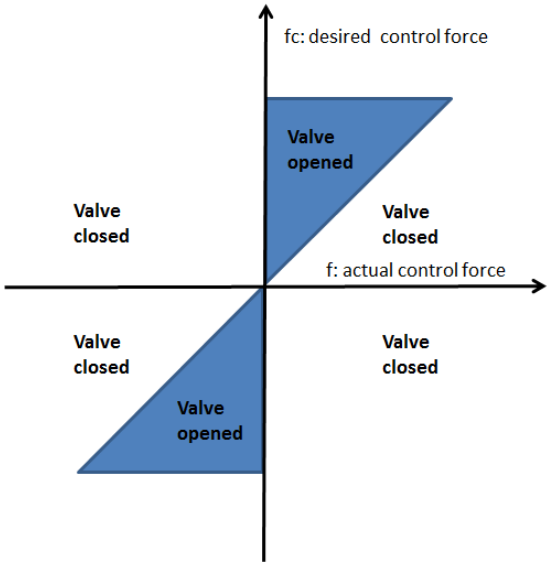

Figure 6.23: the clipped logic.

space form. The optimal damping minimizes the following performance index in continuous time,

$$J(t) = \int_0^\infty \left(x^T(t) Q x(t) + r^T(t) R r(t) \right) dt \tag{6.61}$$

such that the optimal control law with state feedback reads

$$r(t) = -K_{LQR} x(t) \tag{6.62}$$

In order to find the gain K_{LQR}, the unique solution P_∞ of the algebraic Riccati equation (ARE) is obtained by using the Q and R matrices

$$0 = A^T P_\infty + P_\infty A + P_\infty B R^{-1} B^T P_\infty + Q \tag{6.63}$$

and the gain results

$$K_{LQR} = R^{-1} B^T P_\infty \tag{6.64}$$

In the most common case, the full state is not available from the structure. As a consequence, it is possible to reconstruct the full state by means of the optimal observer. The stationary Kalman predictor in continuous time is obtained by solving the following Algebraic Riccati Equation

$$0 = A^T P_\infty + P_\infty A + P_\infty C R^{-1} C^T P_\infty + Q \tag{6.65}$$

As a result, we reconstructed the full state by means of the optimal Kalman observer with gain, i.e.

$$L = P_{\infty} C^T R^{-1} \tag{6.66}$$

The components of the semi-active controller are shown in figure 6.24 and are composed by several theoretical blocks: a) the controlled system or plant, b) the observer, c) the system controller, d) the damper clipped controller, e) the current driver, f) the damping element. The plant is subject to external excitations modeled as plant noise and has noise corrupted outputs. If only accelerations are available or just part of the state is known, the optimal observer reconstructs the full state of the system, otherwise the full state must be available for the control algorithm. Then the selected controller generates the optimal control force in this case through the LQR algorithm and sends the control law $r(t)$ to the clipping block. At this point, the output of the clipping block is the voltage; and the voltage sent to the damper is function of the clipped logic explained above. Only after the voltage definition, the current driver transforms the voltage signal into a current signal and sends it to the MR damper. Consequently, the current signal activates the damper which exerts the optimal damping force on the plant.

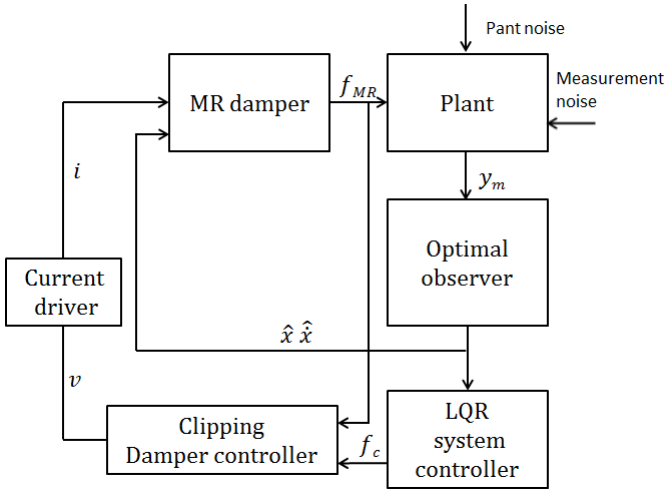

Figure 6.24: LQG clipped control scheme.

6.6.3 The model of the controlled structure

The Den Hartog scheme is composed by a 2DoF system where the first DoF is the mode to be damped and the second DoF is the TMD mass; the simplified controlled system is governed by a second order differential equations,

$$M\ddot{u}(t) + C\dot{u}(t) + Ku(t) = HF(t) + Gr(t) \tag{6.67}$$

where $H = \begin{bmatrix} 0 & 1 \end{bmatrix}$ and $G = \begin{bmatrix} +1 & -1 \end{bmatrix}$ are matrices that depend on the position of external load and of the controlled forces in the dynamic system, $F(t)$ is the applied external force, $r(t)$ is the target control force for the damper. The goal of the clipped logic is to emulate $r(t)$ by means of the actual force exerted by the damper $F_d(t)$ that is available in the experimental environment from the load cell. The mass damping and stiffness matrices eventually are,

$$M = \begin{bmatrix} m_s & 0 \\ 0 & m_d \end{bmatrix}, \; C = \begin{bmatrix} c_s & 0 \\ 0 & 0 \end{bmatrix}, \; K = \begin{bmatrix} k_s + k_d & -k_d \\ -k_d & k_d \end{bmatrix} \tag{6.68}$$

Defining the state vector as $x = \begin{bmatrix} u \\ \dot{u} \end{bmatrix}$, the classical equation of motion in state space form and in discrete form time reads,

$$\dot{x}(t) = Ax(t) + Br(t) + B_f F(t) \tag{6.69}$$

$$\dot{x} = \begin{bmatrix} 0 & I \\ -M^{-1}C & -M^{-1}K \end{bmatrix} x + \begin{bmatrix} 0 \\ -M^{-1}G \end{bmatrix} r + \begin{bmatrix} 0 \\ -M^{-1}H \end{bmatrix} F \tag{6.70}$$

Of course, the state is obtained through the Kalman observer since in the footbridge application only acceleration of the deck and the relative displacement between deck and TMD mass are measured. The available deck acceleration measurement can be related to the modal acceleration of the chosen mode. The MR-TMD active control is based on the theory of optimal control so the damper is controlled by a Linear Quadratic Gaussian Control.

6.6.4 Control concept applied to the simulated MR damper

The semi-active control is numerically tested with the outline presented in figure 6.24. The benchmark 2DoF system is composed by two masses, two passive

springs, a passive and an active damper and has the following characteristics corresponding to the third mode of the Nomi Calliano footbrdge,

- m_s = 1.3556e^5Kg
- k_s = 1.3074e^7N/m
- ω_s = 2π1.5 Hz
- ξ_s = 0.002
- m_d = 2000 Kg
- k_{opt} = 187320 N/m
- c_{opt} = 2817 Ns/m
- α_{opt} = 0.9855 N/m
- μ = 0.0148

The dynamic behavior of the 2DoF is investigated with a chirp force with a varying frequency range spanning from $-$50% to +50% of the primary mass frequency. The sinusoidal force has an amplitude proportional to the modal force corresponding to about 8 equivalent pedestrian. The basic idea is to replace the optimal MR damper of the TMD with the Maurer's prototype so some initial sensitivity test have been performed using the four models shown in figure 6.25. The four models shown in figure 6.25 represent the 2DoF equivalent system introduced by Den Hartog: a) without damper; b) with optimal damper; c) with a Bouc-Wen-like damper; and d) with a controlled damper. Eventually, seven case have been simulated in order to find the 1) steady state Acceleration Frequency Response (AFR) of the 2DoF system without damper, 2) AFR of the 2DoF system with optimal damper, 3) AFR of the 2DoF system with suboptimal damper with a variation in the modal mass of the 20%, 4) AFR of the 2DoF system with a MR damper settled to 0 V and modeled with the frequency and amplitude dependent parameters already validated, 5) AFR of the 2DoF system with a MR damper settled to 4 V and modeled with the frequency and amplitude dependent parameters already validated, 6) semi-active controlled system with nominal modal mass and 7) semi-active controlled system

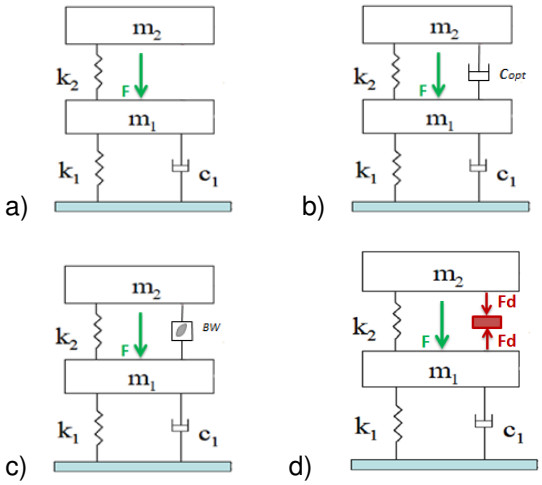

Figure 6.25: 2DoF models for preliminary tests: a) wo damper; b) optimal damper, c) Bouc-Wen-based damper; and d) forced system with clipped MR damper.

with an increase of the modal mass of the 20%. The sampling frequency is 100 Hz. Since the model if both frequency, amplitude and voltage dependent, it has been necessary to take into account for the hysteretic parameters in correspondence of both the relative motion between the two masses and the motion frequency. Of course the current is proportional to the applied voltage applied to the model according to eq. 6.33. Results of simulations are in figure 6.26. We want to show that:

- The insertion of the secondary mass induces the AFR to split into two peaks with similar amplitude. When the damper in not well tuned, that means that a variation in the modal mass or modal stiffness is occurred, the AFR shifts to the left or into the right of the frequency axis and the two peaks assume different amplitude. The damper is called suboptimal since the de-tuning doesn't produce a dramatic change bringing the structure to the initial condition relative to the absence of the damper.
- The presence of the properly tuned damper provides the lower frequency response.
- The de-tuned TMD yields a peak acceleration in correspondence of the new

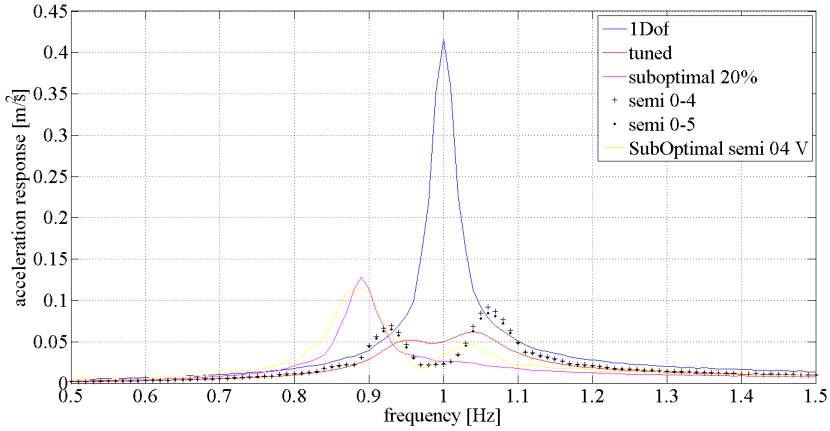

Figure 6.26: FRFs of the seven tested cases.

frequency of the structure.

- TMDs based on semi-active MR dampers driven by the clipped LQG optimal control algorithm have a better effectiveness in the frequency range around the tuning frequency but slightly lower performances around 0.95 and 1.05 the tuning frequency.
- In the presence of uncertainties on the dynamic characteristics of the footbridge, the performance of the passive device are invalidate and the use of a semi-active control strategy becomes of interest
- In presence of the sub-optimal damper the semi-active control reduces the peaks AFR amplitude.

6.6.5 Experimental set-up on the footbridge

After numerical tests, the MR-TMD was eventually positioned on the footbridge in the middle of the deck in correspondence of piece n. 24 and the controller fully activated. The device is instrumented with:

- one displacement transducer AEP with measuring range of 100 mm;
- one acceloremeter PCB 393B12 with black coaxial cable of 3.5 m;
- one load cell AEP of 200 kg with black coaxial cable of 3.5 m;

- two signal transmitters AEP $TA4/2$ fot both the load cell and the displacement transducer (protection class $IP65$)

Figure 6.27 shows the final configuration of the instrumented damper within the TMD housing. The displacement transducer is mounted so that both the movable head is in contact with the surface of the deck and the body is integral with and fixed to the mobile mass of the TMD. The accelerometer is just attached to the deck. The load cell is on the top of the rotative gear and measures the force generated by the damper. The transmitters are on the side of the moving mass feeding sensors and amplifying/filtering the return signal. There is also a control room placed in the

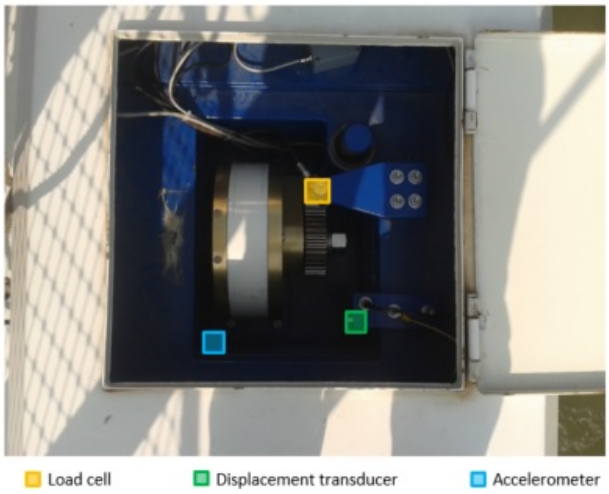

Figure 6.27: the instrumented damper within the TMD.

right shoulder of the bridge. In this cabin, there are several software and hardware components within a humidity protection rack:

- one industrial PC and its power supply;
- one ACE 1104 CLP kit composed by the control board DS 1104 R&D, input/output led panel and software package CDP;
- one Matlab®/Simulink®licence with Real-time Workshop®;
- one PCB accelerometer conditioner model $482A21$ and its power supply;

- the current regulator associated to the MR damper used for the voltage to current inversion;
- UPS;
- Power supply 24 V used for conditioners;
- web connection by means of the industrial router *IR*791.

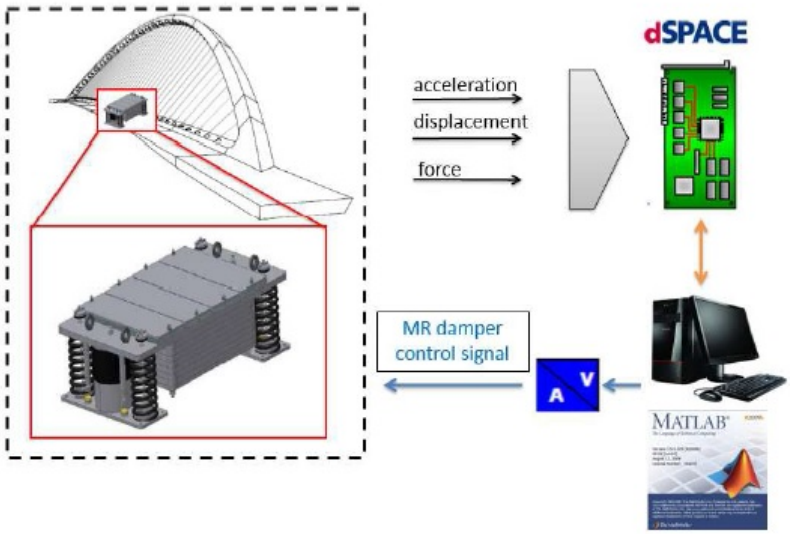

Figure 6.28: the control loop.

As shown in figure 6.28, signals coming from instruments on the MR-TMD are conveyed by means of coaxial cables in the dSPACE®console and then acquired by the hardware/software platform dSPACE®, while the control strategy is drawn in real time by Matlab®/Simulink®. Then, the voltage control signal is converted into a current signal by the driver located in the control cabin. All the wiring along the deck connecting the control room with the dissipation device was previously set during the construction phases of the footbridge. The detailed scheme of the whole equipment is shown in figure 6.29 where it is possible to distinguish between the input signals to dSPACE®from sensors and the output signal from dSPACE®to the damper (and consisting in the on/off control command).

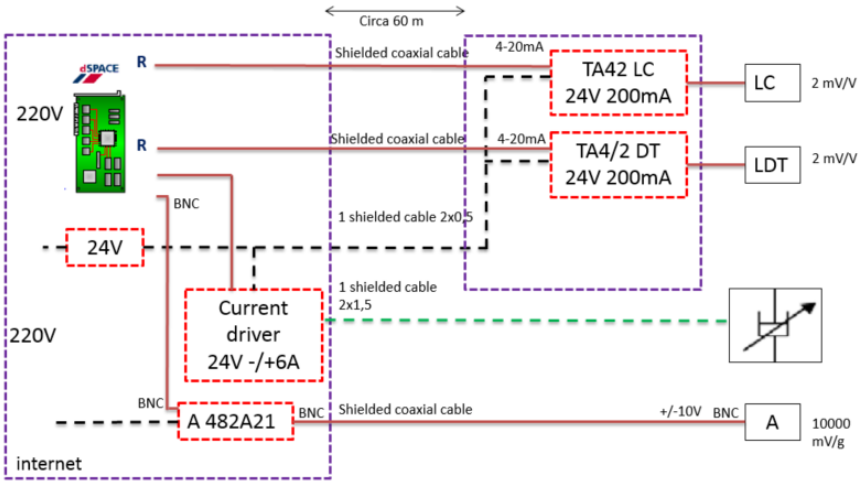

Figure 6.29: detailed scheme of instruments located on both the control room and the deck.

6.6.6 Control validation

The control validation is performed in Matlab/Simulink® through the dSPACE® platform and with a sampling frequency of 100 Hz. In order to experimental validate the control concept and given the availability or real data from the real structure, a set of real events have been selected and are listed in table 6.11. Events

Table 6.11: selected events chosen for the control validation.

n^o	Events	freq. content
1	2013_10_01_17_16_36_F	1.5 Hz
2	2013_10_03_10_15_00_F	2 Hz-2.5Hz
3	2013_10_03_16_59_07_F	1.5 Hz
4	2013_10_03_17_28_20_F	2 Hz-2.5Hz

are recorded by 8 accelerometers belonging to the permanent monitoring system showed in figure 4.30 and referring to the geometric domain. The main frequency content is around 1.5 Hz for events #1 and #3 and 2-2.5 Hz for events #2 and #4. Modal shapes from the updated model with the maximum soil stiffness are used to

project accelerations from the geometric to the modal domain and the third modal acceleration is selected to be used in the modal input identification. The goal is the application to the 2DoF simplified model of the input reconstructed from real recorded data. With regard the input identification, the SDR algorithm is stable for $\lambda >$ 10 steps. It is chosen a λ = 30 so the dimension of the sliding window is quite small and corresponding to 0.3 s with a sampling time of 0.01s. The forward shift *p* is equal to 1. The bandwidth of the system is small and the chosen sampling frequency of 100 Hz results to be accurate in order to avoid the ill conditioning in the frequency domain since the CRLB outside the bandwidth of the system is of the same order of magnitude of the CRLB into the band. The ill conditioning in the time domain is under control as shown in figure 6.30. The NSR is 1 with the regularization parameter β equal to 0.5. The input reconstruction is performed for

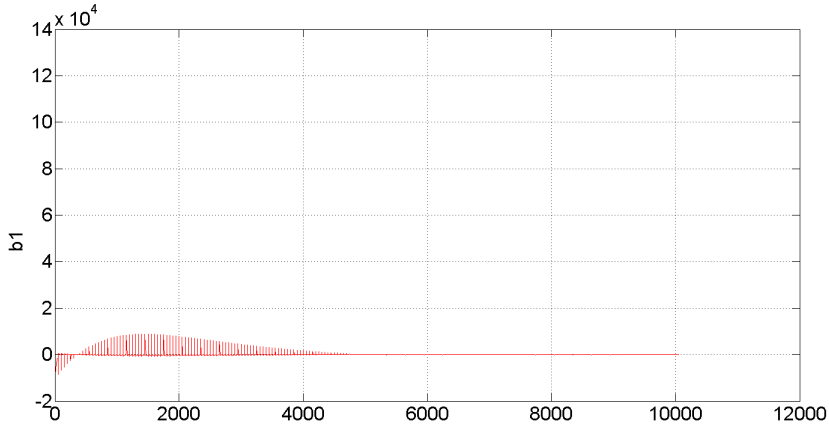

Figure 6.30: conditioning in the time domain of the 2DoF validation system.

all events from the modal acceleration of the third mode and it is in turn applied to the same 2DoF. The reconstruction is validated since real accelerations and accelerations obtained applying to the model the identified input result to be the same as shown in figure 6.31. Eventually, the input reconstruction for all the selected events is accurate. Then, by means of the reconstructed input, it is possible to simulates the semi-active control designed to damp the third asymmetric mode. Figure 6.32 shows results in term of reduction of acceleration of the first event with main frequency content around 1.5 Hz. The semi-active TMD appears to have an

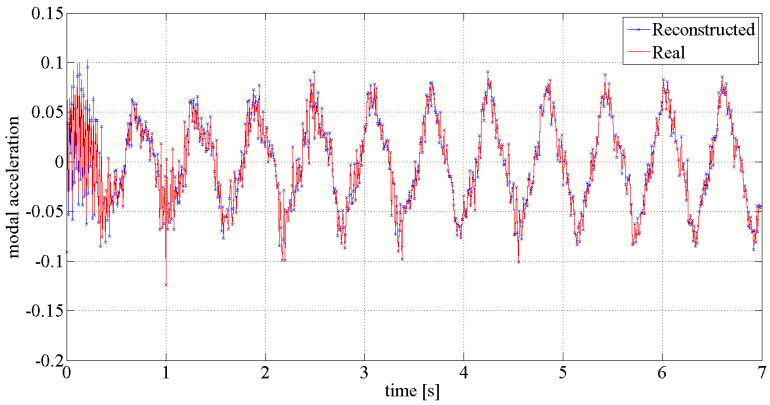

Figure 6.31: reconstructed and real modal accelerations for event #1.

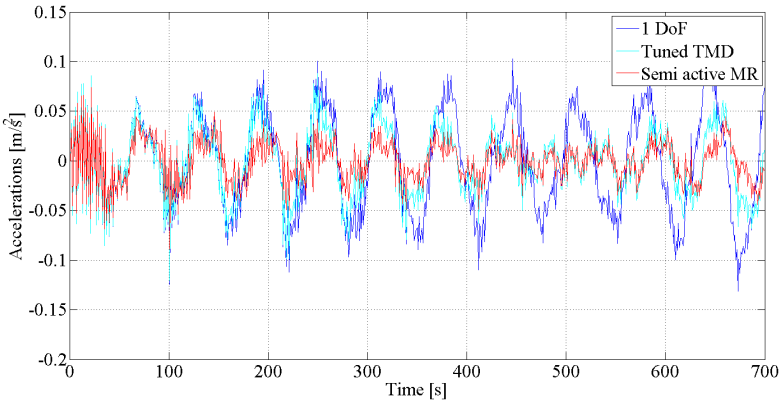

Figure 6.32: plot of reduced accelerations for event #1

increased efficiency respect to the optimal tuned, as detected in figure 6.26, since the forcing frequency belong to the range where the efficiency of the semi-active TMD is higher respect than the one of the passive TMD according to figure . Always according to figure 6.26, event #2 has a different frequency range, however acceleration in presence of the semi-active controller present a slightly reduction respect to the passive situation.

6.7 Conclusions

With regard to the non-linear identification of the MR damper, two parametric models have been evaluated at the Testing Laboratory of the University of Trento.

The first, more complex, results to be both input and voltage dependent, while the second one is a simplified version and it is only voltage dependent even if tuned on 1.5 Hz. Both models seem to be accurate and the validation exhibit a good matching between experimental and numerical.

Simulation of the semi-active control showed that the presence of the properly tuned damper provides the lower frequency response while of course the de-tuned TMD yields a peak acceleration in correspondence of the new frequency of the structure. TMDs based on semi-active MR dampers driven by the clipped optimal control algorithm have a better effectiveness in the frequency range around the tuning frequency but slightly lower performances in correspondence of 0.95 and 1.05 time the tuning frequency. If there are uncertainties on the dynamic characteristics of the footbridge, the use of a semi-active control strategy becomes of interest since a small variation in the acceleration response is detected.

Eventually, the semi-active control strategy consisting of the clipped LQG control is validated by the use of a real load history. The load is the result of an input identification process stable for $\lambda > 10$ step and with a forward shift p equal to 1. The chosen sampling frequency of 100 Hz is such that the ill conditioning in the frequency domain is avoided while the ill conditioning in the time domain presents no criticality.

6.8 Appendix C - hysteresis behavior of the MR damper

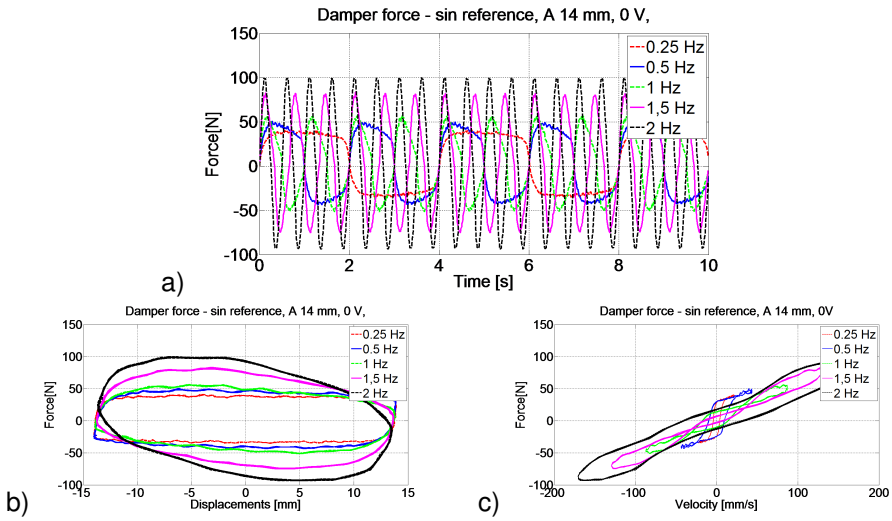

Figure 6.33: test with sinusoidal reference of 14 mm amplitude and subjected to 0V: a) Damper force time history; b) Force vs. Displacements cycle; and c) Force vs. Velocity cycle.

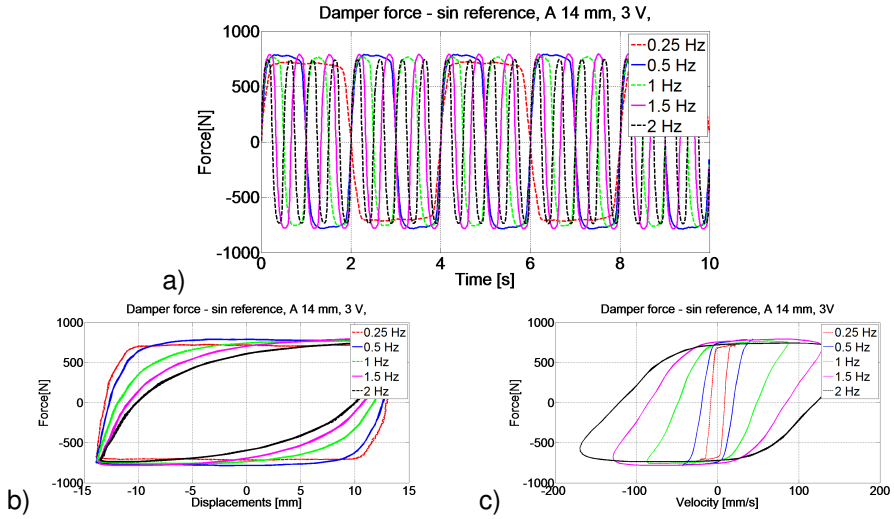

Figure 6.34: test with sinusoidal reference of 14 mm amplitude and subjected to 3V: a) Damper force time history; b) Force vs. Displacements cycle; and c) Force vs. Velocity cycle.

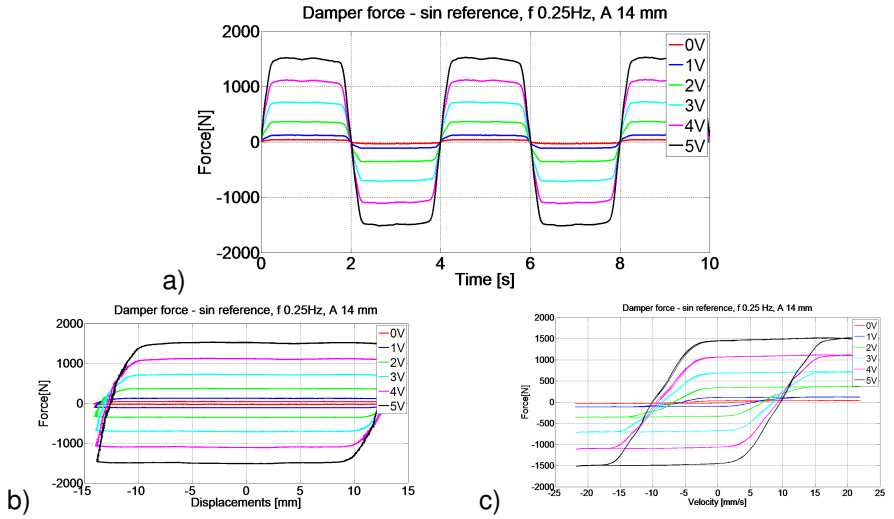

Figure 6.35: test with sinusoidal reference of 14 mm and 0.25 Hz: a) Damper force time history; b) Force vs. Displacements cycle; and c) Force vs. Velocity cycle.

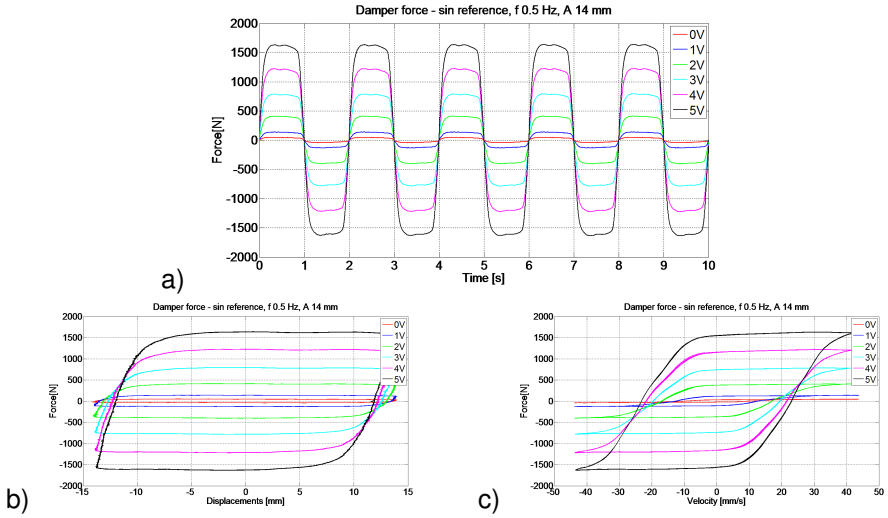

Figure 6.36: test with sinusoidal reference of 14 mm and 0.5 Hz: a) Damper force time history; b) Force vs. Displacements cycle; and c) Force vs. Velocity cycle.

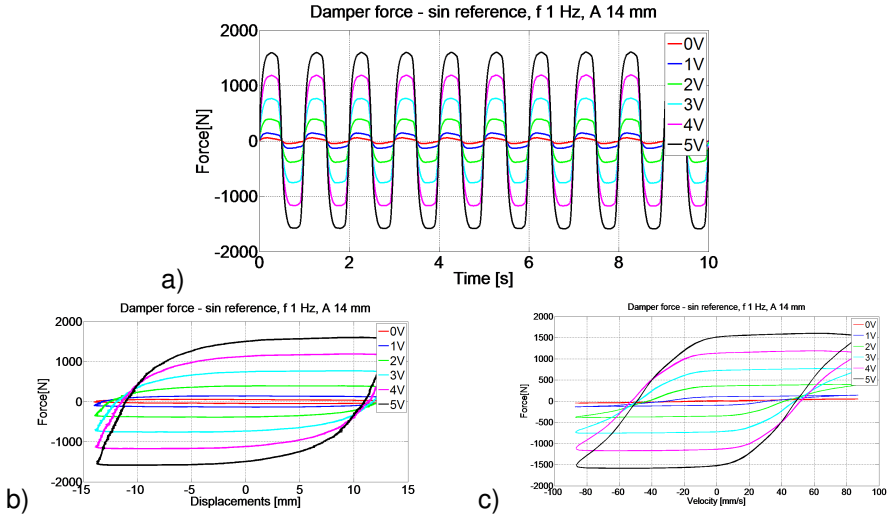

Figure 6.37: test with sinusoidal reference of 14 mm and 1 Hz: a) Damper force time history; b) Force vs. Displacements cycle; and c) Force vs. Velocity cycle.

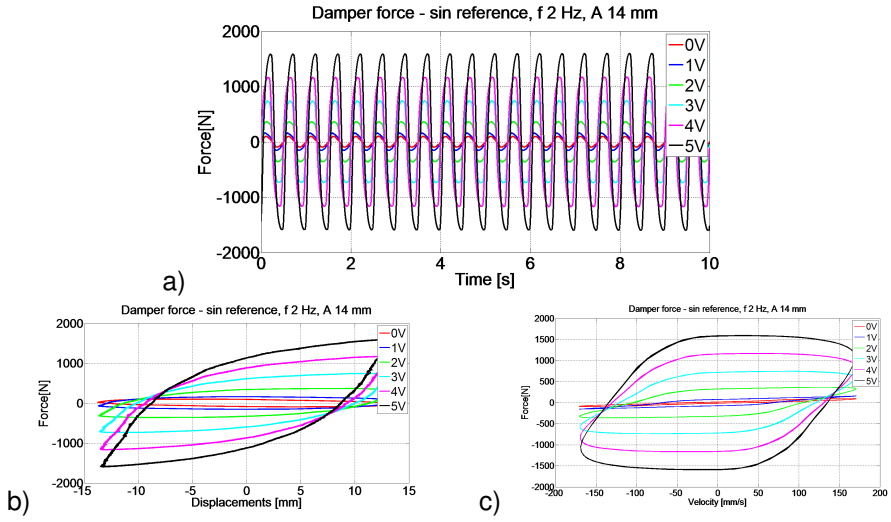

Figure 6.38: test with sinusoidal reference of 14 mm and 2 Hz: a) Damper force time history; b) Force vs. Displacements cycle; and c) Force vs. Velocity cycle.

CHAPTER 7

SUMMARY, CONCLUSIONS AND FUTURE PERSPECTIVES

7.1 Summary

The thesis deal with two main research topics: input identification and identification and control of a MR TMD.

1. The first topic regards the reconstruction of inputs from measured outputs. With regard to the state of the art, different approach are present in literature such as the Recursive Least Square approach, the Minimum-variance unbiased input and state estimate algorithm as well as a multitude of steady state observer based on the Kalman filter. However, the original contribution of the thesis is related to the formulation of the SDR algorithm; in particular the attention is focused on the case where the system is linear and time invariant, the input-output map is available either from a Finite Element model or from system identification and inputs are not repeated in space. Identificability, stability and ill conditioning are relevant problems addressed in the study. In addition, a second element of originality is related to the off-line inspection of the number and position of inputs from recorded data. Eventually, numerical and experimental tests have been performed.

2. The second topic deals with modeling of magneto-rheological fluids and control of the magneto-rheological damper to be installed on the Nomi-Calliano footbridge. In view of the installation, modeling and control of the device is consequently performed. Non-linear model for hysteretic systems are firstly presented and, then, the attention is shifted on hysteretic models for MR fluids. After an introduction about the use of the Unscented Kalman Filter for

non-linear estimation of general model of hysteresis, a parametric model for the MR damper is found and validated. Eventually, with the aim of tools such as input identification and real data from the installed monitoring system, a clipped control law is formulated to control the semi-active device.

7.2 Conclusions

- Chapter 4 deals with the dynamic analysis of the Nomi footbridge. Analysis showed that the footbridge without additional damping devices suffers from the exceeding of acceleration limits; so the design of a damping system composed by 4 TMDs was performed with the support of the experimental modal analysis and with the aim of identifying the modal dynamic characteristics of the system. The dynamic analysis led to the conclusion that a damping system composed by four TMDs needed to be added to the main structure in order to both ensure a behavior compatible with the serviceability limits imposed by the owner and avoid vibrational phenomena already observed in literature. The campaign devoted to the experimental modal analysis was organized to define the modal properties of the structure necessary for the correct design of the passive system of TMDs. Impulsive excitation and environmental excitation were used to obtain the first 7 vibrational modes. Since the identification tests were carried out on the structure not yet complete, in order to obtain the correct modal mass necessary for the design of the tuned devices, both model refinement and model updating were needed. Correct frequencies were eventually extrapolated after model updating and model refinements and the proper design parameters of the passive TMDs were evaluated as a function of the adjustment process. Additional analysis inherent the sensitivity of the damper parameters respect to the soil stiffness and the gradient of temperature showed that the optimal solution for the specific footbridge was the insertion of three passive and one semi-active TMD. Eventually, the damping system was designed and the bridge was equipped with a monitoring system integrated with the structure with the purpose of checking the actual response, with particular reference to the dynamic behavior related to the effect of wind and pedestrians. After the first three trimester of monitor-

ing, no exceeding of imposed limits was recorded. An interesting behavior of the footbridge was detected and consisted of the fact that in presence of low entity wind events, the structure oscillates according to the first mode while wind velocity higher than 15 m/s, mainly excites the 4^{th} vibrational mode.

- Chapter 5 addresses the determination of the number the position and the time histories of unmeasured inputs. It was shown that the number of inputs can be determined in a batch mode and with good accuracy from the rank of a matrix formed using the Fourier transform of the output data and provided that the number of unknown input is less than the measurements and that the available output is sufficiently long. The position of the inputs can subsequently be established with the aid of a model. The position of the acting loads indeed established by inspecting the generalized angles made by the columns of the transfer matrix of the model with the basis identified from the data. Once the input mapping is complete the time history of the load was inferred with good accuracy using a sequential deconvolution algorithm. In this respect, the I/O arrangement and the inherent delay of the problem define if the input is identifiable or if it is identifiable on any subspace. The sequential deconvolution is an iterative method that takes into account for the inherent delay of the system. For this purpose, the kernel of the Toeplitz was fundamental for the comprehension of constraints and limitations on the input reconstruction, especially if the input reconstruction has to be solved in the recursive fashion. It was shown that the part of the input affected by the delay is strictly related and can be detected through inspection of the Toeplitz matrix. Since the deconvolution is carried out on a sliding window, the SDR algorithm is a conditionally stable process and the condition for stability is derived. The size of the sliding window has to be chosen carefully because it affects the stability of the algorithm. It has been proved that both the discretization in time and space also affects the conditioning in the solution. An expression for the error in the reconstructed input as a function of the noise sequence is developed and is used to control the regularization or decide if regularization is needed. Both numerical and experimental tests have been performed and were characterized by favorable results.

- Chapter 6 treated the identification and control of a magneto-rheological damper to be installed on the Nomi-Calliano footbridge. With regard the non-linear identification of the MR damper, two parametric model have been evaluated at the Testing Laboratory of the University of Trento. The first resulted to be more complex since parameters describing the hysteretic cycle were both input and voltage dependent; the second model was a simplified version and was just voltage dependent and if tuned on 1.5 Hz and around 12 mm of input amplitude. Both the models seemed to be accurate and the validation presents a good matching between experimental data and numerical model. The Unscented Kalman filter as a tool for non-linear identification was investigated on time invariant benchmarks: tests showed that in the presence of varying parameters and huge noise, longer acquisition were needed in order to reach convergence. Moreover, an additional test on the capability of the UKF was done by using real experimental data from the MR damper installed on the TT1. At this stage the identification is performed in reference to the stationary system without any change in the input or in the applied voltage. Good matching results were obtained since parameters are obtained on-line and present time-varying values around the initial condition. The second part of the Chapter was about the control of the semi-actice tuned mass damper. Simulation showed that the presence of the properly tuned damper provides the lower frequency response while of course the de-tuned TMD yields a peak acceleration in correspondence of the new frequency of the structure. So a semi-active strategy called Clipped optimal control law based on the Linear Quadratic Regulator was chosen and implemented on the TMD model. Basically, the approach consisted of a feedback loop that force the damper to produce a desired control force according to LQR algorithm and by means of an on-off control of the voltage. The semi-active TMD driven by the clipped optimal control algorithm showed a better effectiveness in the frequency range around the tuning frequency but slightly lower performances around peaks of the 2DoF system.

- Eventually, the semi-active control strategy was validated by the use of a real load histories. In order to select the third modal acceleration and in view of

the control validation, eight events, whose geometric acceleration have been projected in the modal domain, have been used. Modal loads corresponding to the third mode have been reconstructed through an input identification process stable for $\lambda > 10$ step and with a forward shift p equal to 1. The chosen sampling frequency of 100 Hz was such that the ill conditioning in the frequency domain is avoided while the ill conditioning in the time domain presented no criticality. In turn, loads have been applied to the 2DoF system representing the semi-active TMD and the control logic has been applied to damp the third asymmetric mode. The semi-active TMD exhibited an increased efficiency with respect to the optimal tuning in the presence of events with main frequency content around 1.5 Hz. In addition, also in the presence of suboptimal conditions, the semi-active controller yielded a slightly reduction of accelerations with respect to the passive condition.

7.3 Future perspectives

As presented in the previous sections, this research has deepened some aspects of the input identification and control of a MR-TMD. Other aspects are how to deal with model uncertainties and how to include the damper dynamics into the control model. It is not always possible to know or to predict the input acting on a structure, so unknown loads are of mayor concern since they can have big impact on the structure since they are just considered as unknown disturbances within the model. In addition, modeling of large-scale structures lead to model errors. Errors may result from the inclusion or the neglect of highly nonlinear elements in the system dynamic, from mismodeling in material and geometric properties, discretization and linear approximation of nonlinearities. As consequence, modelling errors and uncertain parameters affect the controller robustness. Finally, it is not always possible to measure all the state variables, so the control performance might be affected by property of measurements channels and a compromise involving the number and position of available sensors must be done. Lastly, smart material such as magneto-rheological dampers have limitations associated with their hysteretic and nonlinear behavior. Limitations are mainly due to the difficulty to include in the model also the damper dynamic since parameters describing the hysteretic

shape are load dependent and exhibit a time delay that must be taken into account. As a consequence, in presence of parametric uncertainties, unknown disturbances and limited measurements, application of nonlinear control techniques became mandatory and must be pursued.

7.4 List of publications

- Oreste S. Bursi, Enrico Cazzador, Alessia Ussia, “Probability analysis of a twin deck curved cable-stayed footbridge subjected to multiple inputs and corrosion”, submitted to Reliability Engineering & System Safety.

- D. Bernal, A. Ussia, “Sequential deconvolution input reconstruction”, submitted to Mechanical Systems and Signal Processing.

- D. Bernal, A. Ussia and O. Bursi, “On line and off line Identification of Inputs: Numbers, Locations and Time Histories”, abstract accepted to Eurodyn 2014.

- D. Bernal and A. Ussia, “Identification of Independent Inputs and their Spatial Positions”, in Proceedings of IMAC 2014, Orlando, Florida USA February 3-6, 2014.

- A. Ussia, A. Bonelli, O.S. Bursi, “Modeling and Optimal Semi Active Control Strategies for adaptive MR-TMD”in Proceedings of Structures Congress , USA: ASCE and American Society of Civil Engineers, 2013. - ISBN: 9780784412848. Proceeding of Structures Congress 2013, Pittsburgh, Pennsylvania, United States, 2-4 May 2013

- O. S. Bursi, A. Ussia, A. Kumar,“Structural health monitoring of a complex cable-stayed footbridge and reliability assessment” in The 11^th International Conference on Structural Safety & Reliability, USA: A. A. Balkema, 2013. Atti di: ICOSSAR 2013, New York, USA, 16-20, June. - URL: http://icossar2013.org/

- A. Ussia, O.S. Bursi, A. Bonelli, “Optimal Control of a Footbridge Endowed with Semi Active MR TMDs”in Proceedings of the 5^th European Conference on Structural Control, 18-20 June, Genoa, Italy: Erredi Grafiche Editoriali S.n.c., 2012. - ISBN: 9788895023137. Proceedings of: EACS 2012, Genoa, Italy, 18-20 June

- O.S. Bursi, A. Bonelli, R. Ceravolo,N. Tondini, A. Ussia, “Dynamic and Aeroelastic Behavior of a Twin Deck Curved Cable-Stayed Footbridge Equipped with Passive Devices”in Proceedings of the Engineering Mechanics Institute 2011, Boston, USA: Eurodyn, 2011. Proceedings of: Conference EMI 2011, Boston, USA, June 2-4, 2011

BIBLIOGRAPHY

Eurocode 0 UNI EN 1990. Criteri generali di progettazione strutturale., 2006.

T. T. Baber and M. N. Noori. Modeling general hysteresis behavior and random vibrations applications. *Journal of Vibration, Acoustic, Stress and Reliability in Design*, 108:411–420, 1986.

T.T. Baber and Y.K. Wen. Stochastic equivalent linearization for hysteretic, degrading, multistory structures. Technical report, University of Illinois, Urbana-Champaign Report No. 471 UILU-ENG-80-2001, 1980.

T.T. Baber and Y.K. Wen. Random vibrations on hysteretic, degrading systems. *Journal of the Engineering Mechanics Division*, 107(6):1069–1087, 1981.

D. Bernal. Optimal discrete to continuous transfer for band limited inputs. *Journal of Engineering Mechanics*, 133:1370–1377, 2007.

D. Bernal and A. Ussia. Sequential deconvolution input reconstruction. *Mechanical Systems and Signal Processing (accepted)*, 2013.

M. Bertero and T. A. Poggio. Ill-pose problems in early vision. In *Proceedings of the IEEE*, 1988.

A. N. Blekherman. Autoparametric resonance in a pedestrian steel arch bridge: Solferino bridge. *Journal of Bridge Engineering*, 12(6):669–676, 2007.

R. Bouc. Forced vibration of mechanical systems with hysteresis. In *4th Conference of non-linear Oscillation*, page 315, 1966.

R. Bouc. Modle mathmatique d' hystrsis. *Acustica*, 24:16–25, 1971.

F. Carli. Non-linear response of hysteretic oscillator under evolutionary excitation. *Advanced Engineering Software*, 30(9-11):621–630, 1999.

J. D. Carlson and M. R Jolly. Mr fluid, foam and elastomer devices. *Mechatronics*, 10:555–569, 2000.

J. D. Carlson, D. M. Catanzarite, K. A. Clair, and W. A. Bullogh. Magneto-rheological fluid dampers for semi-active seismic control. In *5th International Conference on ER fluids, MR fluids and Assoc. Tech*, pages 20–28, 1996.

F. Casciati. Smoothed plasticity laws and elasto-plastic analysis. Technical report, Dipartimento di Ingegneria Strutturale e Geotecnica, Universita' di Roma la Sapienza, 1988.

F. Casciati. Stochastic dynamics of hysteretic media. *Structural Safety*, 6:259–269, 1989.

F. Casciati, G. Magonette, and F. Marazzi. *Technology of Semi-Active devices and application in vibration mitigation*. John Wiley and Sons, Ltd, 2006.

R. Ceravolo. Use of instantaneous estimators for the evaluation of structural damping. *Journal of Sound and Vibration*, 274(1-2):385–401, 2004.

A. Cigada, G. Diana, and E. Zappa. On the response of a bridge deck to turbulent wind. *Journal of Wind Engineering and Industrial Aerodynamic*, 90:1173–1182, 2002.

L. Cohen. *Time-Frequency Analysis*. Englewood Cliffs, NJ Prentice-Hall Inc, 1995.

P. Dallard, T. Fitzpatrick, A. Flint, S. Le Bourva, A. Low, S. R. Ridsill, and M. Willford. The london millennium footbridge. *The Structural Engineer*, 79, 2001a.

P. Dallard, T. Fitzpatrick, A. Flint, A. Low, S. R. Ridsill, M. Willford, and M. Roche. London millennium bridge: pedestrian-induced lateral vibration. *Journal of Bridge Engineering*, 6, 2001b.

M. Darouach and M. Zasadzinski. Unbiased minimum-variance estimation for systems with unknown exogenous inputs. *IEEE Transactions on Automatic*, 39(3): 606–609, 1997.

Universita degli Studi di Trento. Nuovo ponte ciclopedonale sul fiume adige nel comune di nomi - identificazione dinamica ponte privo di dispositivi di smorzamento e ponte provvisto di dispositivi di smorzamento ed effetti dinamici indotti dallazione dei pedoni. Technical report, Department of Civil, Mechanical and Environmental Engineering, 2012.

G. Diana, F. Resta, M. Belloli, and D. Rocchi. On the vortex shedding forcing on suspension bridge deck. *Journal of Wind Engineering and Industrial Aerodynamic*, 94:341–363, 2006.

A. Dominiquez, R. Sedaghati, and I. Stiharu. A new dynamic hysteresis model for the magneto-rheological damper. *Journal of Engineering Mechanics*, 5:1179–1189, 2006.

A. Dominiquez, R. Sedaghati, and I. Stiharu. Modeling and application mr dampers in semi-active structures. *Computational structures*, 86:407–415, 2008.

J. F. Doyle. Determining the contact force during the transverse impact of plates. *Experimental Mechanics*, pages 10–16, 1984.

J. F. Doyle. A wavelet deconcolution method for impact force estimation. *Experimental Mechanics*, pages 403–408, 1997.

S. J. Dyke. *Acceleration feedback control strategies for active and semi-active control systems: modeling, algorithm development and experimental verification*. PhD dissertation, Department of Civil engineering and Geological Sciences, 1996.

S. J. Dyke, B. F. Spencer, M. K. Sain, and J. D. Carlson. Modeling and control of magneto-rheological dampers for seismic reduction. *Smart Material and Structures*, 5:565–575, 1996.

D. J. Ewins. *Modal testing, theory, practice and application*. Research Study Press, 2000.

A. Filiatrault, R. Tremblay, and R. Kar. Performance evaluation of friction spring seismic damper. *Journal of Structural Engineering*, 126(4):491–499, 2000.

G. C. Foliente. Hysteresis modeling of wood joints and structural systems. *Journal of Structural Engineering*, 121:1013–1022, 1995.

G. C. Foliente, P. Singh, and M. N. Noori. Equivalent linearization of generally pinching hysteretic, degrading systems. *Earthquake Engineering and Structural Dynamics*, 25:611–629, 1996.

D. R. Gamota and F. E. Filisko. Dynamic mechanical studies of a electro-rheolocical materials: moderate frequencies. *Journal of Rheology*, 35:399–425, 1991.

C. F. Gauss. Theoria motus corporum coelestium. 1809.

H. Gavin. Multi-duct er dampers. *Journal of Intelligent material, System and Structures*, 12:353–366, 2001.

S. Gillijns and B. De Moor. Unbiased minimum-variance input and state estimation for linear discrete-time system with direct feedthrough. *Automatica*, 43:934–937, 2007a.

S. Gillijns and B. De Moor. Unbiased minimum-variance input and state estimation for linear discrete-time systems. *Automatica*, 43:111–116, 2007b.

E. Giorcelli, A. Fasana, L. Garibaldi, and A. Riva. Modal analysis and system identification using armav models. In *The 12th International Modal Analysis Conference IMAC*, 1994.

T. P. Gunstona, J. Rebelleb, and M. J. Griffina. A comparison of two methods of simulating seat suspension dynamic performance. *Journal of Sound and Vibrations*, 278:117134, 2004.

H. Hanselman. Implementation of digital controllers, a survey. *Automatica*, 23(1): 7–32, 1987.

D. Hartog. *Mechanical vibrations*. McGraw-Hill,, 1940.

C.P. Heine. *Simulated response of degrading hysteretic joints with slack behaviour*. Phd thesis, 2001.

F. Hlawatsch and G. F. Boudreaux-Bartels. Linear and quadratic time-frequency signal representation. *IEEE Signal Processing Magazine*, 20:1483–1510, 2006.

C. S. Hsieh. Robust two-stage kalman filters for systems with unknown inputs. *IEEE Transactions on Automatic Control*, 45(12):23742378, 2000.

J. S. Hwang, A. Kareem, and W. J. Kim. Estimation of modal loads using structural response. *Journal of Sound and Vibration*, 326:522–539, 2009.

J. S. Hwang, A. Kareem, and W. J. Kim. Wind load identification using wind tunnel test data by inverse analysis. *Journal of Wind Engineering and Industrial Aerodynamics*, 99(1):1826, 2011.

F. Ikhouane and F. Dyke. Modeling and identification of a shear mode magneto-rheological damper. *Smart Material ans Structures*, 16:1–12, 2007.

F. Ikhouane, V. Manosa, and J. Rodellar. Dynamic properties of the hysteretic bouc-wen model. *System and Control Letters*, 56:197–205, 2007.

H. Inoue, N. Ikeda, K. Kishimoto, T. Shibuya, and T. Koizumi. Inverse analysis of the magnitude and direction of impact force. *JSME International J. Series A*, 38: 84–91, 1995.

M. Ismail, F. Ikhouane, and Rodellar J. The hysteresis bouc-wen model, a survey. *Archives of Computational Methods for Engineering*, 16:161–188, 2009.

L. Jansen and S. J. Dyke. Semi active control strategies for mr dampers: a comparative study. *Journal of Engineering Mechanics*, 126:795–803, 2000.

R. Jimenez and L. Alvarez-Icaza. Lugre friction model for a magneto-rheological damper. *Structural Control and Health Monitoring*, 12:91–116, 2005.

M. Jolly, J. D. Carlson, and B. C. Munoz. A model for the behavior of magneto-rheological materials. *Smart Material and Structures*, 5:607–614, 1996.

J. N. Juang and M. Phan. *Identification and control of Mechanical Systems*. Cambridge University Press, 2001.

S. J. Julier and J. K. Uhlmann. A general method for approximating non-linear transformation of probability distributions. Technical report, Dept. of Engineering Science - University of Oxford, 1996.

S. J. Julier and J. K. Uhlmann. Correction to unscented filtering and non-linear estimation. In *IEEE*, volume 3, pages 1958–1958, 2004a.

S. J. Julier and J. K. Uhlmann. Unscented filtering and non-linear estimation. In *IEEE*, volume 3, pages 401–422, 2004b.

T. Kailath. *Linear Systems*. Prentice Hall, 1990.

R. E. Kalman. A new approach to linear filtering and prediction problems. *Trans. ASME Journal of Basic Engineering*, 82:35–456, 1960.

P. K. Kitanidis. Unbiased minimum variance linear state estimation. *Automatica*, 23(6):775–778, 1987.

T. Kobori, N. Koshika, K. Yamada, and Ikeda Y. Seismic-response-controlled structure with active mass driver system, part i: Design. *Earthquake Engineering and Structural Dynamics*, 20:133–149, 1991a.

T. Kobori, N. Koshika, K. Yamada, and Ikeda Y. Seismic-response-controlled structure with active mass driver system, part ii: Verification. *Earthquake Engineering and Structural Dynamics*, 20:151–166, 1991b.

J.-H. Koo. *Using magneto-rheological dampers in semiactive tuned vibration absorbers to control structural vibrations*. Phd thesis, 2003.

T. Koupra, J. Bartosek, and Zemcik R. Loading force reconstruction and impact location identification for unidirectional carbon/epoxy wide beam. In *9th YSESM*, 2010.

N. Kurata, T. Kobori, M. Takahashi, N. Niwa, and H. Midorikawa. Actual seismic response controlled building with semi-active damper system. *Earthquake Engineering and Structural Dynamics*, 28(11):1427–1447, 1999.

N. M. Kwok, Q. P. Ha, M. T. Nguyen, J. Li, and B. Samali. Bouc-wen model parameter identification for a mr fluid damper using computationally efficient ga. In *ISA Transactions*, number 46, pages 167–179, 2007.

S. S. Law and T. H. T. Chan. Moving force identification: a time domain method. *Journal of Sound and Vibration*, 201:1–22, 1997.

S. S. Law and Y. L. Fang. Moving force identification: optimal state estimation approach. *Journal of Sound and Vibration*, 239(2):233–254, 2001.

S. S. Law, J. Q. Bu, and X. Q. Zhu. Time-varying wind load identification from structural responses. *Engineering Structures*, 27:15861598, 2005.

J.M. Leuridan, D.L. Brown, and R.J. Allemang. Time domain parameter identification methods for linear modal analysis: a unifying approach. *ASME Paper Number 85-DET-90*, 1985.

S. J. Li, Y. Suzuki, and M. Noori. Identification of hysteretic systems with slip using bootstrap filter. *Mechanical Systems and Signal Processing*, 18:781–795, 2004.

J. J. Liu, C. Ma, C. Kung, and D. C. Lin. Input force estimation of a cantilever plate by using a system identification technique. *Computed Methods in Applied Mechanics and Engineering*, 190(11-12):1309–1322, 2000.

A. Lorenzi and O. S. Bursi. Valutazione e riduzione delle vibrazioni di un ponte ciclopedonale ad arco inclinato tramite tmd. Technical report, Department of Civil, Mechanical and Environmental Engineering, 2011.

Z. R. Lu and S. S. Law. Force identification based on sensitivity in time domain. *Journal of Engineering Mechanics*, 132(10):1050, 2006.

J. P. Lynch. *Decentralization of wireless monitoring and control technologies for smart civil structures*. PhD thesis, Dept. of Civil and Environmental Engineering, Stanford University, CA, 2002.

J. P. Lynch and K. H. Law. Market-based control of linear structural systems. *Earthquake Engineering and Structural Dynamics*, 31(10):1855–1877, 2002.

F. Ma, C. H. Ng, and N. Ajavakom. On system identification and response prediction of degrading structures. *Structural Control and Health Monitoring*, 13(1): 347–364, 2006.

N. M. M. Maia, Y. E. Lage, and M. M Neves. *Recent Advances on Force Identification in Structural Dynamics*, chapter 6. http://dx.doi.org/10.5772/51650, 2012.

N.M.N. Maia and J.M.M. Silva. *Theoretical and experimental modal analysis*. Research Studies Press, Wiley, 1997.

S.F. Masri, J.P. Caffrey, T.K. Caughey, A.W. Smyth, and A.G. Chassiakos. dentification of the state equation in complex non-linear systems. *International Journal of Non-linear Mechanics*, 39:1111–1127, 2004.

F. J. Millanes and Ripa T. Pascual. The new abandoibarra footbridge next to the guggenheim museum, bilbao. *Bulletin ouvrages mtalliques*, 3, 2004.

Oliver Nelles. *Non-linear system identification*. Springer, 2001.

A. Nishitani and Y. Inoue. Overview of the application of active/semi-active control to building structures in japan. *Earthquake Engineering and Structural Dynamics*, 30:1565–1574, 2001.

L. J. L. Nordstrom. A dynamic programming algorithm for input estimation on linear time-variant systems. *Computer Methods and Applied Mechanical Engineering*, 195:64076427, 2006.

A. Occhiuzzi, M. Spizzuoco, and G. Serino. Semi-active mr dampers in tmds for vibration control of footbridges, part 1: Numerical modeling and control algorithm. In *Footbridge 2002*, 2002.

A. Occhiuzzi, M. Spizzuoco, and F. Ricciardelli. Loading models and response control of footbridges excited by running pedestrian. *Structural Control and Health Monitoring*, 15:349–368, 2008.

T. Pinkaew and Y. Fujino. Effectiveness of semi-active tuned mass dampers under harmonic excitation. *Engineering Structures*, 23:850–856, 2001.

G. Raia. Progetto esecutivo passerella ciclopedonale sul fiume adige nel comune di nomi, 2010.

J. C. Ramallo, H. Yoshioka, and B. F. Spencer. A two-step identification technique for semiactive control systems. *Struct Control Health Monitoring*, 11:273–289, 2004.

S.M. Savaresi, S. Bittanti, and M. Montiglio. Identification of semi-physical and black-box non-linear models: the case of mr dampers for vehicles control. *Automatica*, 41:113–127, 2005.

M. Setareh. Application of semi-active tuned mass dampers to base-excited systems. *Earthquake Engineering and Structural Dynamics*, 30:449–462, 2001.

S. Seth and P. L. Jerome. Wireless networked distributed controllers for real-time control of civil structures. In *American Control Conference*, 2005.

Setra'. Stra footbridges - assessment of vibrational behaviour of footbridges under pedestrian loading, ministre des transports de l' equipement du tourisme et de le mer, 2006.

D. Simon. *Optimal state estimate*. Wiley, 1990.

A. W. Smyth, S. F. Masri, A. G. Chassiokos, and T. K. Caughey. On-line parametric identification of mdof non-linear hysteretic systems. *Journal of Engineering Mechanics*, 125:133–142, 1999.

A. W. Smyth, S. F. Masri, E. G. Kosmatopoulos, and T. K. Caughey. Development of adaptive modeling techniques for non-linear hysteretic systems. *International Journal of Non-Linear Mechanics*, 37:1435–1451, 2002.

T. T. Soong, A. M. Reinhorn, Y. P. Wang, and R. C. Lin. Full-scale implementation of active control. i: Design and simulation. *Journal of Structural Engineering*, 117(11):35163536, 1991.

B. F. Spencer, F. Dyke, M. K. Sain, and J. D. Carlson. Phenomenological model for magneto-rheological dampers. *Journal of Engineering Mechanics*, 123:230–238, 1997.

B. F. Jr. Spencer. Civil engineering applications of smart damping technology. In *5th Int. Conf. on Vibration Engineering*, 2002.

B. F. Jr. Spencer and S. Nagarajaiah. State of the art of structural control. *Journal of Structural Engineering*, pages 845–856, 2003.

B. F. Jr. Spencer and M. K. Sain. Controlling buildings: A new frontier in feedback. *IEEE Control Syst. Mag*, 17(6):19–35, 1997.

R. Stanway, J. L. Sproston, and N. G. Stevens. Non-linear identification of semi-active control devices. *IFAC Identification and System Parameter estimation*, pages 195–2000, 1985.

R. Stanway, J. L. Sproston, and N. G. Stevens. Non-linear modeling of an electro-rheological vibration damper. *Journal of Electrostatics*, 20:167–184, 1987.

M. D. Symans and M. C. Constantinou. Semi-active control systems for seismic protection of structures: A state-of-the-art review. *Eng. Struct.*, 221(6):469487, 1999.

P. C. Tuan, C. C. Ji, L. W. Fong, and W. T. Huang. An input estimation approach to on-line two dimensional inverse heat conduction problem. *Numerical Heat Transfer*, 29:345–363, 1996.

P. C. Tuan, S. C. Lee, and W. T. Hou. An efficient on-line thermal input estimation method using kalman filter and recursive least square algorithm. *Inverse Problems in Engineering*, 5(4):309–333, 1997.

A. Van Den Bos. *Parameter Estimation for Scientists and Engineers*. John Wiley and Sons, Inc., 2007.

R. van der Merve. *Sigma-Point Kalman Filters for Probabilistic Inference in Dynamic State-Space Models*. PhD thesis, Faculty of the OGI School of Science and Engineering at Oregon Health and Science University, 2004.

R. van der Merve and E. A. Wan. Efficient derivative-free kalman filters for online learning. In *European Symposium on Artificial Neural Network (ESANN)*, 2001a.

R. van der Merve and E. A. Wan. The square-root unscented kalman filter for state and parameter estimation. In *International Conference on Acoustic, Speech and Signal Processing*, 2001b.

R. van der Merve, R. De Freitas, A. Doucet, and E. A. Wan. The unscented particle filter. Technical report, Dept. of Engineering - Cambridge University, 2000.

P. Van Overschee and B. De Moor. *Subspace Identification for Linear Systems: Theory and Implementation - Applications*. Kluwer Academic Press Dordrecht, 1996.

E. A. Wan and R. van der Merve. The unscented kalman filter for non-linear estimation. In *Symposium 2000 on Adaptive Systems for Signal Processing, Communication and Control*, 2001.

E. A. Wan, R. Van der Merwe, and A.T. Nelson. *Advances in Neural Information Processing Systems*, chapter Dual estimation and the Unscented transformation, pages 666–672. MIT Press, 2000.

Y.K. Wen. Method of random vibration of hysteretic systems. *ASCE Journal of Engineering Mechanics*, 102:249–263, 1976.

Y.K. Wen. Equivalent linearization for hysteretic system under random excitation. *Journal of Applied Mechanics*, 47:150–154, 1980.

N. Wiener. *Extrapolation, Interpolation and smoothing of stationary time series*. MIT Press, 1949.

L. Y. Yu and Chan H. T. Moving force identification based on the frequency-time domain method. *Journal of Sound and Vibration*, 261:329349, 2003.

K.-V. Yuen, Y. Shi, J. Beck, and H.-F. Lam. Structural protection using mr dampers with clipped robust reliability-based control. *Structural and Multidisciplinary Optimization*, 34:431–443, 2007.

F. L. Zanotti. *Dynamic models for ancient heritage structures*. PhD thesis, Polytechnic University of Turin, 2012.

M. F. Zapateiro De La Hoz. *Semi-active control strategies for vibration mitigation in adaptronic structures equipped with magneto-rheological dampers*. PhD thesis, Girona, Spain, 2009.